Polynorbornenes: Synthesis and Application as Gas Transport Membranes

A Dissertation Presented for the

Doctor of Philosophy

Degree

The University of Tennessee, Knoxville

Elizabeth Margaret Powell

May 2025

DEDICATION

I want to dedicate this dissertation to my grandmother, Rita Evans. I lived in the house next door to my grandparents, but I'd argue that between mornings before school, afternoons after school, and full days during summer vacation, I grew up there as much as I did at the house next door. My grandmother instilled in me a love of reading, an appreciation for the arts, and a self-assurance that has guided me to where I am today. She once told me, "Your education is the one thing no one can ever take away from you." I have held that line with me through every high and low of my college and graduate school career. Rita Evans is one of the strongest and most loving women I have had the privilege of knowing, and I count myself lucky that I call her Nannie.

ACKNOWLEDGEMENTS

If you had asked me 10 years ago if I'd be receiving a PhD in chemistry, I would have laughed and said that it was only for geniuses. But here I am—far from being a genius—and receiving a PhD. I know beyond a shadow of a doubt that is because of the never-ending support and love of my family. I have been incredibly lucky to have had parents, a sister, and grandparents who have always seen potential in me even when I couldn't. So, I first want to acknowledge them for everything they have given and sacrificed for me. I want to thank my mom for talking with me almost every morning on my drive to work. You have encouraged me, comforted me, and cheered for me more than anyone could ever hope for. I want to thank my dad for the example he set for me. You have shown me how to work hard, change a tire, and move through life with the certainty that everything will be okay. I want to thank my sister, Grace who has kept me laughing through this all. I want to thank my boyfriend, David. You, more than anyone, have had to endure the graduate school version of me and all the good, the bad, and the ugly that entails. And you have handled it better than I could have ever asked. Thank you for proofreading every paper, listening to every presentation, and never letting me quit. Having you through this experience has meant more to me than I could express.

Next, I want to thank my PI, Professor Brian Long. You hold your lab and your graduate students to a high standard. Thank you for that and for expecting so much more out of me than I did myself. This has been a tough, sometimes infuriating journey, but I will be forever thankful to have had the opportunity to be mentored by you.

I want to thank Dr. Justin Burroughs, Dr. Xinyi Wang, Dr. Cameron Workman, Dr. Trevor Wilson, Nick Shawver, Christy Witcher, Rahil Parikh, Godwin Ochola,

Rakesh Patter, Mason Jones, Karina Guerrero, Nathan Kunzler, Sophie Ahmed, Taylor Marcum, Taylor Lundquist, Shelby Watson, and numerous others for the past five years of friendship, mentorship, and goofing. This has been the toughest adventure of my life, but this lot somehow found a way to keep me laughing the entire time.

Next, I want to thank the members of my dissertation committee, Professor Mike Kilbey, Professor Konstantinos Vogiatzis, and Professor Gila Stein. I cannot thank you all enough for your mentorship and encouragement over the years. Thank you for pushing me and guiding me to form me into the scientist I am today.

Finally, I want to thank my cats, Mr. Milk and Banjo, my ballroom dance community, as well as my friends in book club and at cross stitch and everyone else who has supported me through this time in my life. I can honestly say that I wouldn't be here today without each and every one of you.

ABSTRACT

Dense polymeric gas separation membranes offer a passive and energy efficient alternative to current separation methods in industries such as carbon capture, hydrogen recovery, and natural gas purification. Polynorbornenes (PNB's) are particularly interesting as membrane materials due to the modular nature of the monomeric feedstock and polymerization techniques. For example, norbornene derivatives polymerized via vinyl addition polymerization (VAP) yield polymers that maintain the bicyclic norbornane moiety within the polymeric backbone giving rise to materials with high glass transition temperatures (T_g) and decomposition temperatures (T_d). Conversely, norbornene derivatives polymerized via ring opening metathesis polymerization (ROMP) yield rubbery polymers with double bonds in the backbone that exhibit lower T_g's and T_d's. The tunable nature of polynorbornenes (PNBs) makes these polymers attractive materials for studying the structure-property relationships that governs gas transport properties.

However, there is a significant drawback in the polymerization of these monomers. Norbornenes are typically synthesized via a Diels-Alder reaction that yields a mixture of *endo*- and *exo*-substituted isomers. It has been widely reported that the *endo*-substituted monomers are less reactive in both VAP and ROMP compared to their *exo*-substituted counterparts. Additionally, the catalysts typically employed for VAP have poor functional group tolerance; notably, polar functionalized norbornenes give rise to low molar mass polymers in low yields. Herein, I present my contribution to the world's understanding of the polymerization of polar-functionalized norbornenes and expound

upon the application of VAP and ROMP PNB's as dense polymeric gas separation membranes.

My first project (Chapter II) explores the coordination environment of polar vs nonpolar norbornene monomers with VAP neutral, single-site Ni-based catalysts. In Chapter III, I investigate the effects that monomer stereochemistry has on the gas transport properties of VAP PNB's. My final project (Chapter IV) explores the incorporation of ROMP PNB into the backbone of highly rigid polymers of intrinsic microporosity (PIMs) as segmented block copolymers and their subsequent gas transport properties.

TABLE OF CONTENTS

LIST OF TABLES

LIST OF FIGURES

LIST OF SCHEMES

CHAPTER I:

1.1 Introduction to Norbornene Polymerization Techniques

Norbornene and norbornene derivatives are an interesting class of monomers that offer facile tunability of polymer characteristics through choice of monomer functionality and polymerization method. The most commonly employed approach for synthesizing norbornenes is through a [4pi+2pi]-cycloaddition (Diels-Alder) reaction that gives rise to a mixture of *endo*- and *exo*- substituted monomers.[1, 2] The strained bicyclic nature and olefin present within the backbone of norbornenes allows these monomers to be polymerized in a variety of ways including cinyl addition polymerization (VAP) and ring opening metathesis polymerization (ROMP). However, it is commonly observed that for both polymerization methods, the *exo*-substituted monomers are more reactive than their *endo*-substituted counterparts.[3-6]

VAP of norbornenes gives rise to a thermally robust and chemically stable polymers that retain their bicyclic moiety within the backbone. While a variety of catalysts have been employed to polymerize norbornene (Ti, Cr, Fe, Co, and Cu), functionalized norbornenes typically require late transition metal catalysts containing Ni or Pd centers.[1, 7] Still, polar-functionalized norbornene monomers give rise to polymers with low molar masses and low yields. In Pd-based catalysts this has been shown to arise from coordination and/or chelation of the polar moiety to the metal center.[8-10] While the field of VAP has seen astounding progress in recent years, continued research is necessary to broaden the scope of polymerizable monomers via VAP. ROMP is a highly reactive and synthetically simple living polymerization that yields unsaturated polymers that exhibit low glass transition temperatures (T_g) and poor chemical stability.[11, 12] The catalysts used in ROMP (W and Ru), however, are far more functional-group tolerant than those used for VAP; therefore, a number of functionalized monomers can be polymerized via ROMP. Additionally, the functional group tolerance of ROMP catalysts allows

for the incorporation of chain transfer agents that can be utilized to end-functionalize polymer chain ends. [13, 14]

1.2 Introduction to Dense Polymeric Gas Transport Membranes

Chemical separations accounts for 10-15% of the United States' energy consumption. This includes refining crude oil, separating alkenes and alkanes, and carbon capture which utilize distillation, cryogenic distillation, and amine adsorption respectively. All of these methods require heating during their processes which drives up the energy expense and cost of separation. It has been proposed that developing alternative, energy-efficient methods could reduce operational costs in the US annually by $4 billion.[15] In facilities that separate CO_2 from flue gas emissions, this is especially relevant as the release of greenhouse gases, such as CO_2 into this atmosphere has been linked to anthropogenic climate change. With energy consumption in the US expected to climb, it becomes more and more imperative to develop energy-efficient and cost-effective methods for CO_2 separations.

Dense polymeric gas separation membranes offer a passive alternative to current industrial separation methods. To evaluate the performance of polymeric membranes for gas separation, Robeson plotted gas transport data for a number of gas pairs on a log-log plot of selectivity (α_{ij}) of the two gases (P_i/P_j) vs permeability (P_i) where P_i and P_j represent the permeability of the more and less permeable gases, respectively (**Figure 1.1**). The slope of this line (n) determined from equation **1** was found to correlate strongly with the ratio of the kinetic diameter of the gas pairs. The line from this equation is representative of what is referred to as the upper bound, above which virtually no data points appear. In this equation (**eq. 1**), α_{ij} represents the selectivity of two gases (P_i/P_j); k is the front factor; and P_i is the permeability of

the more permeable gas as previously stated. From this line a trade-off was established for permeability and selectivity.[16]

$$P_i = k\alpha_{ij}^n \quad \textbf{(eq. 1)}$$

The upper bound is theoretically explained using the solution-diffusion model which describes the transport of a gas molecule through dense polymeric membranes (**Figure 1.2**). In this model, gas transport is divided into three significant steps. The first step is the sorption of a particular gas into the face of the membrane exposed to high pressure, which is followed by diffusion of this gas through the membrane. In the final step, the gas desorbs from the face of the membrane exposed to low pressure. Permeability (P_i) of the gas molecule is, therefore, governed by two parameters: diffusivity (D_{ij}) and solubility (S_{ij}) (**eq. 2**).[17] Considering selectivity (α_{ij}) is simply the ratio of the permeability of two gas molecules, selectivity can be further divided into diffusivity selectivity and solubility selectivity (**eq. 3**).

$$P = D \times S \quad \textbf{(eq. 2)}$$

$$\alpha_{ij} = \frac{P_i}{P_j} = \frac{D_i \times S_i}{D_j \times S_j} \quad \textbf{(eq. 3)}$$

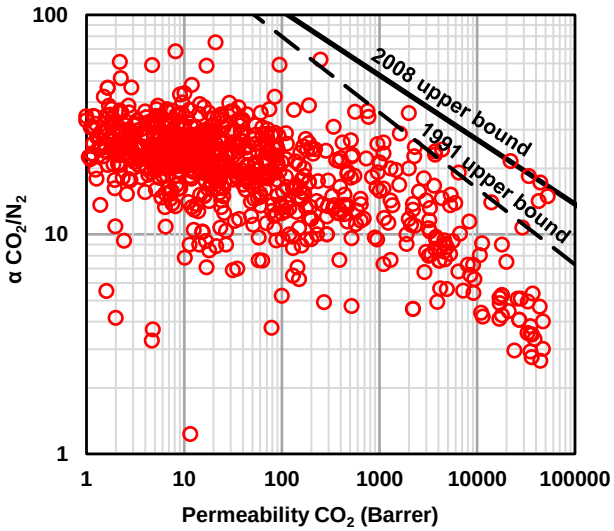

Figure 1.1. Robeson plot of CO_2/N_2 for a breadth of polymeric materials.

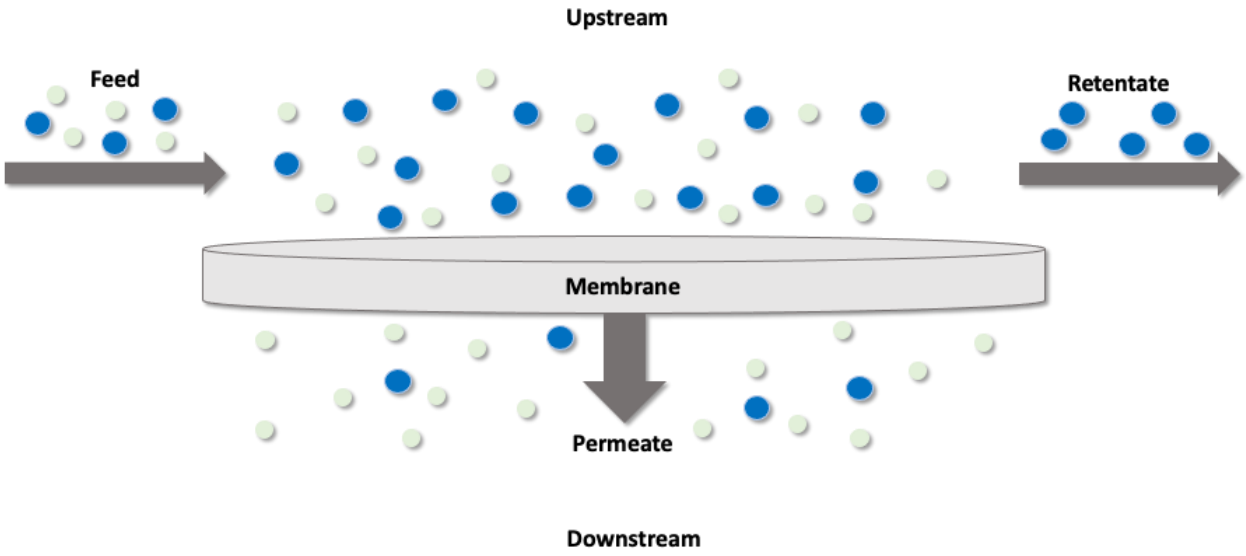

Figure 1.2. Schematic representation of membrane driven gas separations.

Interestingly, glassy polymers typically dominate the upper bound. This is due in part to their ability to form excess non-equilibrium free volume that allows for a size sieving type effect of gas molecules. However, glassy polymers face two distinct issues: First, membranes made from glassy polymers are commonly diffusivity-controlled exhibiting lower solubility coefficients, and second, glassy polymers undergo what is known as physical aging. Physical aging is a process by which the excess non-equilibrium free volume within the polymer matrix densifies over time as a consequence of segmental motion towards thermodynamic equilibrium even below a polymer's glass transition temperature (T_g). [18,9] Rubbery polymers have a liquid-like matrix in which gas molecules permeate via free volume created by transient motion of the polymer chain, rather than "frozen" non-equilibrium free volume.[19] Therefore, rubbery polymers exhibit large diffusivity coefficients with low mobility selectivity and are deemed solubility-controlled materials.[20]

Diffusivity refers to the mobility of the gas molecules through free volume present in the polymer matrix. Therefore, diffusivity of a molecule is governed by chain rotation; size and shape of the penetrant; and non-equilibrium free volume within the polymer.[21] Diffusivity selectivity follows that gas molecules with smaller kinetic diameters diffuse more readily than gas molecules with larger kinetic diameters.

Solubility refers to the interaction of the gas molecules with the polymer matrix and is, therefore, governed by polymer-penetrant interaction; free volume within the polymer and the condensability of the penetrant gas.[21] In amorphous polymers, solubility of gas molecules is agreed to occur through the dual-sorption model (**eq. 4**). Therein, small molecules can dissolve into dense regions within the polymer matrix (Henry's law, $\boldsymbol{k_d}$), and the concentration of gas molecules is expected to increase linearly as a function of increasing pressure. Additionally,

molecules can sorb into free volume elements present within the polymer matrix (Langmuir component, $\frac{C'_H b}{1+bp}$).

$$S = k_d + \frac{C'_H b}{1+bp} \quad \textbf{(eq. 4)}$$

1.3 PIMs

Polymers of intrinsic microporosity (PIMs) are ladder-like amorphous polymers that consist of a fused ring backbone with points of contortion that give rise to frustrated packing and the formation of micropores (<2 nm). [22] PIMs are considered *inherently* microporous because their nonequilibrium free volume that is formed within the polymer matrix is ascribed to the tortuous nature of the backbone rather than processing conditions of the material.[23] The first PIM was developed by Budd and coworkers in 2004 (**PIM-1**), which was formed from the polycondensation reaction of 5,5,6,6,-tetrahydroxy-3,3,3,3-tetramethyl-1,1'-spirobisindane (**1**) and tetra-fluoroterephthalonitrile (**2**) as shown in **Scheme 1.1**. [24] The rigid interconnected regions of large interchain spacing lead to frustrated packing and give **PIM-1** a very high fractional free volume (~0.25) as well as a large apparent BET surface area (~800 m^2g^{-1}).[25] The micropores give rise to a molecular sieving type of separation that allows for increased diffusivity (through increased fractional free volume) with a simultaneous increase in solubility (through increased gas uptake and penetrant-polymer interaction). The increase in the rigidity and the microporous nature of this unique class of polymers has been noted as their exceptional gas transport properties. [23]

Scheme. 1.1 Synthesis of PIM-1

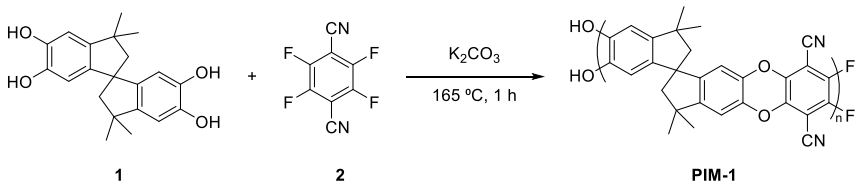

1 2 PIM-1

PIMs have large solubility coefficients compared to most glassy polymers, and in some cases, such as CO_2 and CH_4, they seem to exhibit solubility controlled selectivity.[26] The Budd group proposed this occurred because of the increased free volume from micropores that allows for more gas uptake; however, it can also be accounted for because of the increased polarity from the ether and nitrile groups within the polymer backbone that promotes strong intermolecular interactions between polymer and gas.[24] Despite the increase in permeability, the selectivity of these polymers remains relatively constant in contrast to the trade-off relationship typically observed.[24]

While PIMs show promise as gas separation membranes, they are brittle and exhibit rapid and extensive physical aging which makes them problematic for industrial implementation. Although PIMs have a rigid backbone, microstructural rearrangements within the polymer matrix even below their T_g, causes densification of the polymer membrane and leads to an increase in selectivity (3.5 to 5.0 for O_2/N_2 after 1,380 days) while drastically decreasing the permeability (317 barrer to 64 barrer for N_2 after 1,380 days).[27,28]

1.4 Conclusions and Outlook

The implementation of dense polymeric gas separation membranes for industrial separations offers a promising alternative to the high energy and expensive methods currently employed. There are, however, key issues that need to be overcome before polymeric membranes see widespread industrial application. Namely, these materials are subject to a tradeoff between their permeability and selectivity that greatly inhibits them. Even with significant advances in the development of materials with exceptional gas transport properties, other issues, such as poor mechanical properties and physical aging, limit these materials. As such, there is a continued effort for the development of new and original polymeric materials to

study the structure-property relationship that governs gas transport properties. In order to do this, however, it is imperative that we have access to a wide variety of polymerization methods. VAP is a promising polymerization technique that has been shown to yield highly stable and mechanically robust materials. Notably, this polymerization technique can be used with norbornene and norbornene derivatives which is a favorable monomer feedstock that allows for ease of synthesis and facile tailoring of monomer functionality. However, catalysts commonly employed in VAP are notoriously sensitive to *endo*-substituted monomers and polar-functionalized monomers, overall limiting the pool of norbornene derivative can be tested utilized.

References

(1) M. V. Bermeshev, P. P. C. Addition polymerization of functionalized norbornenes as a powerful tool for assembling molecular moieties of new polymers with versatile properties. *Progress in Polymer Science* **2018**, *84*, 1-46.
(2) Nicolaou;, K. C.; S. A., S.; Montagnon;, T.; Vassilikogiannakis, G. The Diels-Alder Reaction in Total Synthesis. *Angew. Chem. Int. Ed.* **2002**, *41*, 1668-1698.
(3) Funk, J. K.; Andes, C. E.; Sen, A. Addition Polymerization of Functionalized Norbornenes: The Effect of Size, Stereochemistry, and Coordinating Ability of the Substituent. *Organometallics* **2004**, *23* (8), 1680-1683. DOI: 10.1021/om049043l.
(4) Wolf;, W. J.; T. P., L.; Grubbs, R. H. Examining the Effects of Monomer and Catalyst Structure on the Mechanism of Ruthenium-Catalyzed Ring-Opening Metathesis Polymerization. *J. Am. Chem. Soc.* **2019**, *141*, 17796-17808.
(5) Nishihara, Y.; Inoue, Y.; Nakayama, Y.; Shiono, T.; Takagi, K. Comparative Reactivity of Exo- and Endo-Isomers in the Ru-Initiated Ring-Opening Metathesis Polymerization of Doubly Functionalized Norbornenes with BothC yano and Ester Groups. *Macromolecules* **2006**, *39*, 7458-7460.
(6) Tsai, S. D.; Register, R. A. Endo/Exo Reactivity Ratios in Living Vinyl Addition Polymerization of Substituted Norbornenes. *Macromolecular Chemistry and Physics* **2018**, *219* (11), 1800059. DOI: 10.1002/macp.201800059.
(7) Blank, F. C. J. Metal catalysts for the vinyl/addition polymerization of norbornene. *Coordination Chemistry Reviews* **2009**, *253*, 827-861. DOI: 10.1016/j.ccr.2008.05.010.
(8) Hennis, A. D.; Polley, J. D.; Long, G. S.; Sen, A.; Yandulov, D.; Lipian, J.; Benedikt, G. M.; Rhodes, L. F.; Huffman, J. Novel, Efficient, Palladium-Based System for the Polymerization of Norbornene Derivatives: Scope and Mechanism. *Organometallics* **2001**, *20* (13), 2802-2812. DOI: 10.1021/om010232m.
(9) Keyes, A.; Basbug Alhan, H. E.; Ordonez, E.; Ha, U.; Beezer, D. B.; Dau, H.; Liu, Y. S.; Tsogtgerel, E.; Jones, G. R.; Harth, E. Olefins and Vinyl Polar Monomers: Bridging the Gap for Next Generation Materials. *Angew. Chem. Int. Ed* **2019**, *58* (36), 12370-12391. DOI: 10.1002/anie.201900650.
(10) McDermott, J.; Chang, C.; Martín, L. F.; Rhodes, L. F.; Benedikt, G. M.; Lattimer, R. P. β, γ-Carbon−Carbon Bond Cleavage as a Prelude to Chain Transfer in Ester-Functionalized Norbornene Polymerization. *Macromolecules* **2008**, *41* (9), 2984-2986. DOI: 10.1021/ma702779a.
(11) Sutthasupa, S.; Shiotsuki, M.; Sanda, F. Recent advances in ring-opening metathesis polymerization, and application to synthesis of functional materials. *Polymer Journal* **2010**, *42* (12), 905-915. DOI: 10.1038/pj.2010.94.
(12) Wang, X.; Wilson, T. J.; Alentiev, D.; Gringolts, M.; Finkelshtein, E.; Bermeshev, M.; Long, B. K. Substituted polynorbornene membranes: a modular template for targeted gas separations. *Polymer Chemistry* **2021**, *12* (20), 2947-2977. DOI: 10.1039/d1py00278c.
(13) Vanbiervliet, E.; Fouquay, S.; Michaud, G.; Simon, F.; Carpentier, J.-F.; Guillaume, S. M. From Epoxide to Cyclodithiocarbonate Telechelic Polycyclooctene through Chain-Transfer Ring-Opening Metathesis Polymerization (ROMP): Precursors to Non-Isocyanate Polyurethanes (NIPUs). *Macromolecules* **2017**, *50* (1), 69-82. DOI: 10.1021/acs.macromol.6b02137.

(14) Bielawski, C. W.; Benitez, D.; Morita, T.; Grubbs, R. H. Synthesis of End-Functionalized Poly(norbornene)s via Ring-Opening Metathesis Polymerization. *Macromolecules* **2001**, *34* (25), 8610-8618. DOI: 10.1021/ma010878q.
(15) Sholl, D. S.; Lively, R. P. Seven Chemical Separations to Change the World. *Nature* **2016**, *532* (7600), 435-437. DOI: 10.1038/532435a.
(16) Robeson, L. M.; Burgoyne, W. F.; Langsam, M.; Savoca, A. C.; Tien, C. F. High performance polymers for membrane separation. *Polymer* **1994**, *35* (23), 4970-4978. DOI: 10.1016/0032-3861(94)90651-3.
(17) Freeman, B. D. Basis of Permeability/Selectivity Tradeoff Relations in Polymeric Gas Separation Membranes. *Macromolecules* **1999**, *32* (2), 375-380. DOI: 10.1021/ma9814548.
(18) Galizia, M.; Chi, W. S.; Smith, Z. P.; Merkel, T. C.; Baker, R. W.; Freeman, B. D. 50th Anniversary Perspective: Polymers and Mixed Matrix Membranes for Gas and Vapor Separation: A Review and Prospective Opportunities. *Macromolecules* **2017**, *50* (20), 7809-7843. DOI: 10.1021/acs.macromol.7b01718.
(19) Merkel, T. C.; Bondar, V. I.; Nagai, K.; Freeman, B. D.; Pinnau, I. Gas sorption, diffusion, and permeation in poly(dimethylsiloxane). *JOURNAL OF POLYMER SCIENCE PART B-POLYMER PHYSICS* **2000**, *38* (3), 415-434. DOI: 10.1002/(SICI)1099-0488(20000201)38:3<415::AID-POLB8>3.0.CO;2-Z.
(20) DOI: 10.1002/(SICI)1099-0488(20000201)38:3.
(21) Robeson, L. M.; Liu, Q.; Freeman, B. D.; Paul, D. R. Comparison of transport properties of rubbery and glassy polymers and the relevance to the upper bound relationship. *Journal of Membrane Science* **2015**, *476*, 421-431. DOI: 10.1016/j.memsci.2014.11.058.
(22) Staiger, C. L.; Pas, S. J.; Hill, A. J.; Cornelius, C. J. Gas Separation, Free Volume Distribution, and Physical Aging of a Highly Microporous Spirobisindane Polymer. *Chemistry of Materials* **2008**, *20* (8), 2606-2608. DOI: 10.1021/cm071722t.
(23) Budd, P. M.; McKeown, N. B.; Fritsch, D. Free volume and intrinsic microporosity in polymers. *Journal of Materials Chemistry* **2005**, *15* (20), 1977. DOI: 10.1039/b417402j.
(24) Budd, P.; Msayib, K.; Tattershall, C.; Ghanem, B.; Reynolds, K.; McKeown, N.; Fritsch, D. Gas separation membranes from polymers of intrinsic microporosity. *J. Membr. Sci.* **2005**, *251* (1-2), 263-269. DOI: 10.1016/j.memsci.2005.01.009.
(25) Du, N.; Park, H. B.; Dal-Cin, M. M.; Guiver, M. D. Advances in high permeability polymeric membrane materials for CO2separations. *Energy Environ. Sci.* **2012**, *5* (6), 7306-7322. DOI: 10.1039/c1ee02668b.
(26) Budd, P.; McKeown, N.; Ghanem, B.; Msayib, K.; Fritsch, D.; Starannikova, L.; Belov, N.; Sanfirova, O.; Yampolskii, Y.; Shantarovich, V. Gas permeation parameters and other physicochemical properties of a polymer of intrinsic microporosity: Polybenzodioxane PIM-1. *Journal of Membrane Science* **2008**, *325* (2), 851-860. DOI: 10.1016/j.memsci.2008.09.010.
(27) Swaidan, R.; Ghanem, B.; Litwiller, E.; Pinnau, I. Physical Aging, Plasticization and Their Effects on Gas Permeation in “Rigid” Polymers of Intrinsic Microporosity. *Macromolecules* **2015**, *48* (18), 6553-6561. DOI: 10.1021/acs.macromol.5b01581.
(28) McDermott, A. G.; Budd, P. M.; McKeown, N. B.; Colina, C. M.; Runt, J. Physical aging of polymers of intrinsic microporosity: a SAXS/WAXS study. *J. Mater. Chem. A* **2014**, *2* (30), 11742-11752. DOI: 10.1039/c4ta02165g.

CHAPTER II: Polymerization of Ester-functionalized Norbornenes Using Neutral Nickel Catalysts

A version of this chapter was originally published by E. Margaret Powell:

Powell, E. M.; Mimna, R. A.; Day, V. W.; Long, B. K.*; Rhodes, L. F*. Polymerization of Ester-Functionalized Norbornenes Using Neutral Nickel Catalysts. *Organometallics* **2024**, 43, 2565-2573.

*Corresponding author

2.1 Abstract

Addition-type polymerizations have shown tremendous promise for a variety of applications; however, the direct polymerization of polar functionalized norbornene monomers is often challenging when using transition metal-based catalysts. This result is often ascribed to the oxophilic nature of many transition metal species that lead to nonproductive modes of monomer coordination to the Lewis acidic active metal site. Strategies to overcome this issue include the use of late transition metal catalysts, such as those containing Ni and Pd active sites, which generally exhibit greater monomer functional group tolerance. However, discrepancies in molecular weight and yield are still often encountered for the vinyl addition polymerization of polar vs. nonpolar functionalized norbornene monomers. While researchers have studied these effects for Pd-based complexes, analogous studies when using neutral, single-site nickel-based catalysts are absent from the literature. Herein, we will show that polar functionalized norbornenes and a variety of polar additives readily coordinate $L_nNi(C_6F_5)_2$ type vinyl-addition polymerization catalysts, and their polymerization behavior is studied. These results show that simple trends in polynorbornene molecular weight are observed as a function of coordinating ligand (L_n) strength for the polymerization of nonpolar substituted norbornenes, but do not fully explain why the polymerization of polar functionalized norbornenes routinely produce low molecular weight polymers in poor yields.

2.2 Introduction

Polyolefins are the most widely used and distributed polymers, reaching over 184 million tons produced globally in 2017.[1] This is due in part to their inexpensive monomer feedstocks and diversity of thermomechanical properties that may be accessed through tuning polymerization

conditions and (co)monomer identity. Unfortunately, a commonly encountered issue when using early transition metal-based olefin polymerization catalysts is that they are often incapable of polymerizing, or copolymerizing, polar functionalized monomers. This is often ascribed to the highly oxophilic nature of early transition metals, therefore making them incompatible with polar functional groups such as alcohols, ethers, esters, and carboxylic acids.[2]

To circumvent these issues, researchers often use functional group protection-deprotection strategies or synthesize specialty monomers, for example, to enable the use of early transition metal catalysts.[2, 3] However, a promising strategy to access polar functionalized polyolefins via direct (co)polymerization is to shift from early transition metals to late transition metal-based catalysts. For example, cationic Pd diimine complexes originally reported by Brookhart and coworkers have been shown to copolymerize acrylates with ethylene.[4-6] Similarly, certain neutral nickel complexes have also been shown to facilitate the (co)polymerization of functional, olefinic monomers.[7, 8]

Detailed calculational studies of both cationic and neutral nickel and palladium complexes have been carried out to better understand the ability of these late transition metal-based catalysts to copolymerize simple olefins and polar comonomers.[9, 10] Therein, two coordination modes were considered for functional monomers, such as acrylates, to the active metal site: π-olefin and O-coordinated complexes. These studies suggest that complexes with strongly coordinating polar functionality (e.g., M-O-coordination) are inappropriate candidates for functional monomer copolymerization as this may hinder, or prevent, coordination of the functional monomer's olefinic double bond to the active metal site, which is a prerequisite for coordination-insertion polymerization.

Our interest in the area of functionalized polyolefins focuses primarily on polymers derived from cycloolefinic, norbornene-type monomers. In particular, polar functionalized norbornene-based polymers have shown promise as they, depending on the functional group, can exhibit improved adhesion to substrates or solubility in aqueous base, thus forming the basis for electronics packaging polymers and binder resins for photoresist formulations, respectively.[11-14] Complexes that are active for the polymerization of norbornene-based monomers traditionally include both cationic nickel and palladium complexes. However, in 2000, Rhodes and coworkers discovered the activation of nickel-based catalysts toward the polymerization of norbornene by transfer of C_6F_5 from $B(C_6F_5)_3$ to Ni.[15] This discovery led to a class of neutral, single-site nickel complexes bearing electron-withdrawing groups, such as **Ni1** and **Ni2** (**Figure 2.1**) which bear C_6F_5 moieties, and that are highly effective for the polymerization of norbornene.[16]

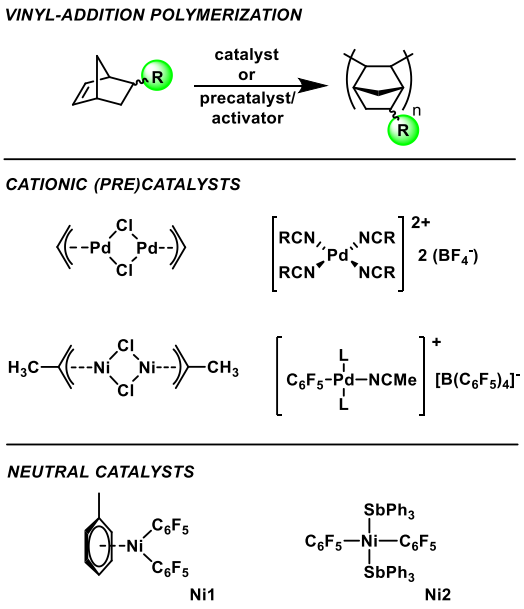

Figure 2.1. Vinyl-addition polymerization of polynorbornenes and examples of commonly used Ni- and Pd-based (pre)catalysts, which propagate via a cationic neutral active metal site.

Despite the success of these neutral nickel catalysts, preliminary work in our labs has consistently shown a discrepancy in the vinyl-addition polymerization of polar functionalized norbornyl monomers using the neutral, single-site nickel catalyst (η^6-toluene)Ni(C_6F_5)$_2$ (**Ni1**), as compared to analogous polymerizations of nonpolar norbornene monomers. Similar effects have been reported for cationic palladium-based catalysts in which the metal center is believed to coordinate the monomer's polar functional group (**Figure 2.2**), inhibiting further monomer insertion into the metal center.[17] Further complications arise in that norbornene-based monomers are commonly synthesized via Diels-Alder reaction that yields a mixture of *endo*- and *exo*-isomers.[18] Monomers having *endo*-substituted polar functional groups may form chelates via the simultaneous coordination of the metal to the polar functionality and bicyclic olefin. (**Figure 2.2**).[17, 19-22] Combined, these two modes of coordination, as well as other issues recently highlighted by Harth and coworkers,[2] are believed to lead to decreased polymerization activity when (co)polymerizing polar-substituted norbornene monomers.

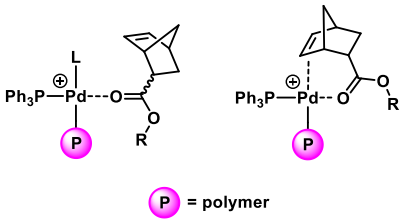

Figure 2.2. Proposed coordination modes when polymerizing prototypical *exo*- and *endo*-ester substituted norbornene monomers using Pd-based catalysts.[17]

2.3 Results and Discussion

2.3.1 Polymerization of Polar vs. Nonpolar Monomers

For the studies presented herein, 5-hexylbicyclo[2.2.1]hept-5-ene (**M1**) and t-butyl bicyclo[2.2.1]hept-5-ene-2-carboxylate (**M2**) are used as prototypical nonpolar- and polar-substituted norbornene monomers, respectively. Each monomer was polymerized using **Ni1** at increasing monomer-to-catalyst ratios (**Scheme 2.1**). For each polymerization, we found that polymerization of nonpolar **M1** gives rise to high molecular weight polymer (M_n = 680-700 kg/mol) in high yield (**Table 2.1**, entries 1-3), while the polymerization of polar functionalized monomer **M2** produced only low molecular weight polymers (M_n = 9-17 kg/mol) in poor yield (**Table 2.1**, entries 4-6).

As previously noted, the low molecular weights and yields observed for the polymerization of polar functionalized monomers using **Ni1** agree well with prior reports employing Pd(II)-based catalysts that propagate via a cationic metal site. Because of this, we hypothesized that a similar type of coordination, and/or chelation, may occur between the carbonyl moiety of ester functionalized monomer **M2** and the neutral active metal center of **Ni1**, as shown in **Figure 2.3**. If valid, these coordination modes may similarly inhibit productive monomer coordination, and/or insertion, and offer a plausible explanation for the lower molecular weight polymers and lower yields produced when polymerizing such polar functionalized monomers, as compared to analogous nonpolar monomer **M1**.

Scheme 2.1. Polymerization of **M1** and **M2** using catalyst **Ni1**.

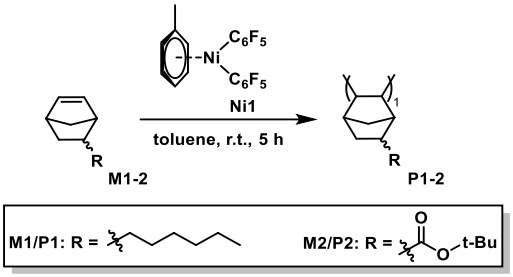

Table 2.1. Polymerization of norbornene monomers **M1** and **M2** to yield polymers **P1** and **P2**, respectively, using **Ni1**[a].

entry	monomer	M:cat	yield (%)	M_n[b] (kg/mol)	Đ [b]
1	M1	50:1	96 ± 6.4	700 ± 66	5.1 ± 2.1
2	M1	100:1	99 ± 0.6	680 ± 30	2.4 ± 0.9
3	M1	750:1	69 ± 2.6	690 ± 36	2.9 ± 0.4
4	M2	50:1	37 ± 6.4	8.7 ± 0.1	1.5 ± 0.1
5	M2	100:1	41 ± 0.7	15 ± 1.0	1.7 ± 0.1
6	M2	750:1	2.8 ± 2.1	17 ± 0.4	1.8 ± 0.1

[a]General polymerization conditions: total monomer = 0.14 mmol, 100 µL toluene; T_{rxn} = 20 ºC, and t = 5 h. All polymerizations were run in triplicate. [b]Molecular weights and dispersity were measured using gel permeation chromatography at 40 ºC in THF and reported relative to polystyrene standards.

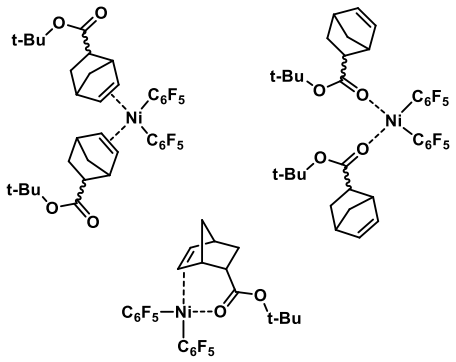

Figure 2.3. Potential coordination modes of ester functionalized monomer **M2** with **Ni1** following displacement of the labile, coordinated toluene.

2.3.2 Coordination Studies

Our initial investigations into the potential coordination of ester-substituted monomer **M2** to the active metal site of catalyst **Ni1** were conducted at low temperature to mitigate undesirable polymerization, which occurs readily at room temperature. Therein, **M2** was combined with **Ni1** in a 2:1 ratio in CH_2Cl_2 at -78 ºC. The solvent and any volatile byproducts were then removed to yield a yellow solid that was analyzed using IR spectroscopy and compared to the individual IR spectra of the native **Ni1** and **M2** (see **Figure A12**). If coordination of the carbonyl moiety of **M2** to the Ni-center occurs, we would expect to observe a shift of the carbonyl stretching frequency to lower wavenumbers as compared to that of free monomer **M2**, which occurs at 1724 $cm^{-1.}$ Indeed, when **M2** was combined with **Ni1**, we observed two stretches at a lower frequency which could be ascribed to symmetric and asymmetric carbonyl stretches at 1636 cm^{-1} and 1614 cm^{-1}.[23] This shift, in addition to the asymmetric nature of the coordinated carbonyl peak, agrees with the coordination of two molecules of **M2** in a cis fashion to the $Ni(C_6F_5)_2$ fragment likely resulting in a square planar complex with pseudo-C2v symmetry.[24, 25] Though these experiments were run at low temperatures in an attempt to avoid polymerization of the monomer, some polymerization was observed that complicated further analysis.

To avoid complications arising from monomer polymerization, monomer **M2** was hydrogenated using Crabtree's catalyst to yield t-butyl bicyclo[2.2.1]heptane-2-carboxylate (**M3**), which prevents the possibility of polymerization while still permitting ester coordination to the active Ni site. Therein, two equivalents of **M3** were added to **Ni1** in CH_2Cl_2 at room temperature followed by removal of the solvent and any volatile byproducts under vacuum to yield a yellow solid (**Scheme 2.2**) that was analyzed by IR and ^{19}F NMR spectroscopy. Again, the single carbonyl stretch observed for **M3** at 1724 cm^{-1} was observed to shift and yield two

new stretches at a lower frequencies (1638 cm^{-1} and 1615 cm^{-1}) that we ascribe to the symmetric and asymmetric carbonyl stretches (**Figure 2.4**), which also agrees with the coordination of two equivalents of **M3** in a cis fashion to the active $Ni(C_6F_5)_2$ site in a square planar complex with pseudo-C2v symmetry.[24, 25]

The ^{19}F NMR spectrum of the product resulting from mixing **M3** + **Ni1** shows a shift in the ortho, para, and meta fluorine resonances for the resultant new species, relative to the starting catalyst (**Figure 2.5**), with new resonances observed at ~ -119 ppm (o-fluorines), -162 ppm (p-fluorines), and -166 ppm (m-fluorines). These results similarly suggest coordination of the carbonyl of **M3** to the Lewis acidic Ni center. It should be noted that the ^{19}F NMR spectra of the products isolated after mixing **M2** + **Ni1** and **M3** + **Ni1** displayed broad signals and/or multiplets, which we attribute to the resultant product complexes bearing a mixture of coordinated *endo*/*exo* stereoisomers of **M2** or **M3**. Attempts to confirm the identity of these new complexes via X-ray crystallography were unsuccessful.

Because we were unable to fully confirm the identity of **Ni1**-**M2** or -**M3** coordinated complexes, we envisioned that simpler esters, such as ethyl acetate (EtOAc), that do not exist as isomeric mixtures might serve as an easily characterizable proxy for **M2** or **M3**. To test this hypothesis, two equivalents of EtOAc were combined with one equivalent of **Ni1** to yield an orange solid following removal of all volatiles under vacuum. Analysis of the resulting Ni complex by IR spectroscopy showed a shift in the single carbonyl peak from 1736 cm^{-1} to a lower frequency that can be ascribed to symmetric and asymmetric carbonyl stretches at 1662 cm^{-1} and 1647 cm^{-1}, which is similar to that observed when using monomers **M2** and **M3**. This data suggests coordination of two ethyl acetate molecules to the nickel center in a cis fashion.

Similarly, ^{19}F NMR spectroscopy also showed shifts of the ortho-, meta-, and para-fluorine signals, as expected (**Figures A21** and **A4**, respectively).

Because these studies showed that even simple esters readily displace toluene and coordinate to **Ni1**, we became interested in how other donor ligands, L, might yield $L_nNi(C_6F_5)_2$ derivatives that might vary in their polymerization behavior for nonpolar and polar norbornene monomers. More specifically, we were interested in how ligands of varying coordinating strengths might impact the polymerization process. Based on this, catalysts **Ni3**, **Ni4**, and **Ni5**, were synthesized by dissolving **Ni1** in an excess of ethyl acetate, tetrahydrofuran, or 1,2-dimethoxyethane (DME), respectively (**Scheme 2.3**) following a modified literature procedure used to previously access **Ni4**.[26]

Scheme 2.2. Mixing of **M3** and **Ni1** to probe potential coordination modes via IR and NMR spectroscopy.

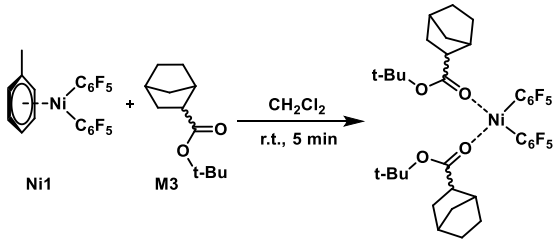

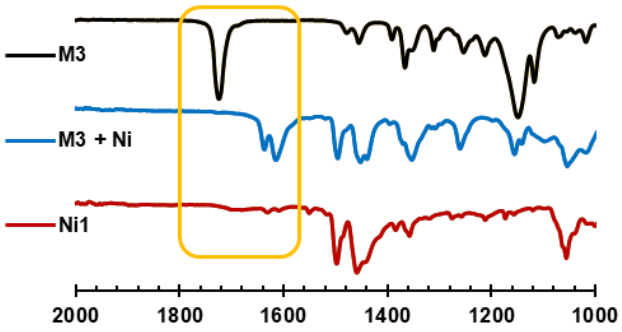

Figure 2.4 IR spectra of the hydrogenated monomer **M3** (top), **M3** + **Ni1** mixed in CH_2Cl_2 followed by removal of all volatiles in vacuo (middle), and **Ni1** (bottom).

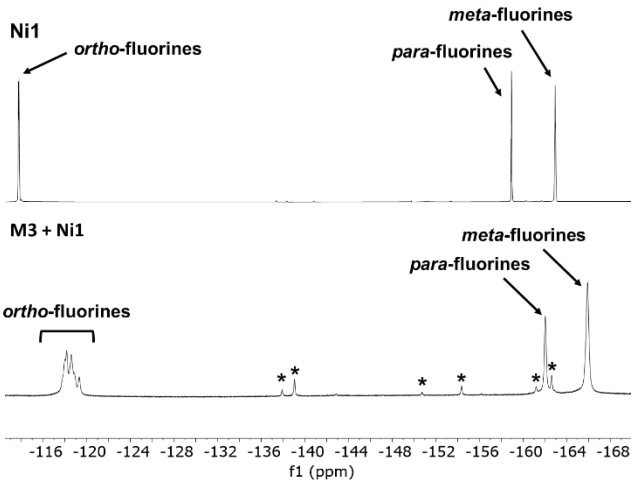

Figure 2.5. ^{19}F NMR spectra of the hydrogenated monomer **Ni1** (top) and the proposed coordinated species resulting from the mixing of **M3** and **Ni1** in a 2:1 ratio, respectively (bottom). Also present in the ^{19}F NMR spectrum are two additional sets of peaks from catalyst degradation. The first set of peaks (-137.91 ppm, -150.73 ppm, and -161.20 ppm) correspond to perfluoro-1,1'-biphenyl, which forms via reductive elimination at the Ni center. The second set of peaks (-139.05 ppm, -154.37 ppm, and -162.62 ppm) correspond to pentafluorobenzene that presumably results from protodemetallation that may have occurred during isolation and analysis of the product.

Catalysts **Ni3**, **Ni4**, and **Ni5**, which bear EtOAc, THF, and DME ligands, respectively, were characterized using ^{1}H, ^{13}C, and ^{19}F NMR spectroscopy. X-ray crystallographic quality crystals of **Ni3** and **Ni5** were grown via layering of hexanes/EtOAc and hexanes/DME, respectively (**Figure 2.6**). **Ni4** was characterized by X-ray crystallography in a prior literature report.[26] Crystallography data of **Ni3** shows coordination of two ethyl acetate ligands in a cis - fashion through the oxygen of the carbonyl moiety to the active Ni center. (**Figure A30**) This coordination environment differs from the trans- environment observed for **Ni2**; however, it agrees nicely with our expectations from IR spectroscopy. Due to the potential for chelation of the DME ligand, **Ni5** was also expected to exist in a similar cis- coordination environment, which has been previously reported for the analogous catalyst bis(2,4,6-tris(trifluoromethyl)phenyl)Ni(1,2-dimethoxy-ethane).[27, 28] Indeed, X-ray crystallographic data of

Ni5 reveals chelation of the DME ligand resulting in cis-coordination of the C_6F_5 ligands (**Figure A32**).

Scheme 2.3. Synthesis of $L_nNi(C_6F_5)_2$ complexes **Ni3-Ni5**.

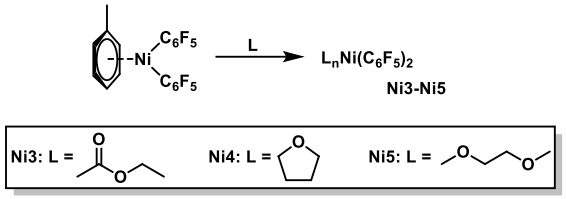

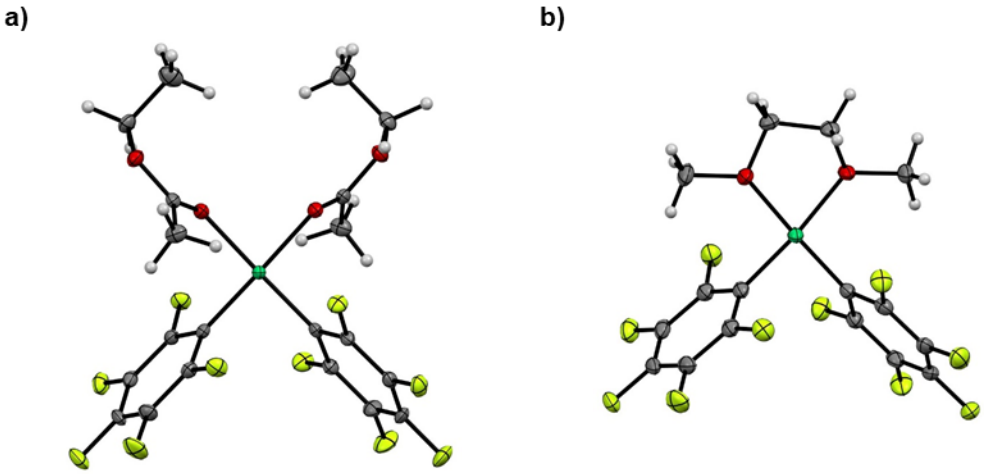

Figure 2.6 ORTEP representations of a) **Ni3** and b) **Ni5**. Thermal ellipsoids are drawn at 50% probability and all hydrogen atoms are included.

2.3.3 Polymerization and Equilibrium Studies

Monomers **M1** and **M2** were polymerized using catalysts **Ni3**, **Ni4**, and **Ni5** following the procedure described above, and are compared to the results obtained using toluene ligated catalyst **Ni1** (see **Table 2.2**). Similar to the results obtained when using catalyst **Ni1**, polymerizations of nonpolar monomer **M1** using **Ni3**, **Ni4**, and **Ni5** each produced high molecular weight polymers (M_n = 460 – 580 kg/mol) in high yield (88-97 %) (**Table 2.2**, entries 2-4). In contrast, analogous polymerizations of ester-containing monomer **M2** once again produced low molecular weight polymers (M_n = 14 – 16 kg/mol) in low yield (18 - 41 %) (**Table 2.2**, entries 6-8). While these results confirm that neutral Ni catalysts **Ni3**, **Ni4**, and **Ni5** remain polymerization active, it suggests that pre-coordination of either polar ester or ether ligands to the active site does not strongly influence the polymer yield or molecular weights obtained when polymerizing polar monomer **M2**.

Though polar-ligand coordinated catalysts **Ni3**, **Ni4**, and **Ni5** were unable to access high molecular weight **P2**, we noted that a trend of steadily increasing molecular weight polymers were obtained for catalysts **Ni3**, **Ni4**, and **Ni5** for the polymerization of monomer **M1**. To investigate this effect further, the K_{eq} between toluene coordinated **Ni1** and its polar ligand coordinated analogues ($L_nNi(C_6F_5)_2$) were each measured as a proxy to estimate the binding strength of each polar ligand to the Lewis acidic Ni center. For example, the K_{eq} between THF-coordinated **Ni4** and toluene-coordinated **Ni1** was measured by combining one equivalent of **Ni1** and two equivalents of THF and the equilibrium position was measured using ^{19}F NMR spectroscopy by integration of the aryl fluorine peaks assigned to each complex (**Figure 2.8**). At equilibrium, two sets of ^{19}F resonances were observed – the first set (-113.8 ppm, -160.2 ppm, and -164.0 ppm) corresponding to the toluene-ligated complex **Ni1** and the second set (-118.4

ppm, -161.2 ppm, and -165.1 ppm) corresponding to bis(THF) ligated **Ni4**. The measured K_{eq} values for **Ni1** in the presence of stoichiometric amounts of EtOAc, THF, and DME were 0.8, 2.7, and 19.0, respectively.

Plots of **P1** and **P2** molecular weight versus measured equilibrium constant (K_{eq}) of each $L_nNi(C_6F_5)_2$ are shown in **Figures 2.9** and **2.10**, respectively. Interestingly, we found that there is a clear linear trend between polymer molecular weight and measured K_{eq} values for **Ni3**, **Ni4**, and **Ni5** when polymerizing nonpolar monomer **M1** (**Figure 2.9**). While the exact mechanistic rationale for this observed behavior is yet unknown, we suspect that the presence of polar additives may aid in the stabilization of the propagating Ni center, thereby preventing deleterious catalyst degradation and yielding higher molecular weight polymers. In contrast, no clear trend was observed for the polymerization of polar monomer **M2** (**Figure 2.10**), wherein the resultant molecular weights were not significantly different from one another based on the 1-sigma criterion.

Table 2.2. Polymerization of norbornene monomers **M1** and **M2** to yield polymers **P1** and **P2**, respectively, using neutral nickel catalysts **Ni1**, **Ni3**-**Ni5**.[a]

entry	Mon.	Cat.	yield (%)	M_n[b] (kg/mol)	$Đ$[b]
1	**M1**	**Ni1**	99 ± 0.6	680 ± 30	2.4 ± 0.9
2	**M1**	**Ni3**	97 ± 1.5	460 ± 18	1.6 ± 0.1
3	**M1**	**Ni4**	88 ± 8.0	510 ± 36	1.9 ± 0.2
4	**M1**	**Ni5**	90 ± 1.5	580 ± 35	1.9 ± 0.4
5	**M2**	**Ni1**	41 ± 0.7	15 ± 1.0	1.7 ± 0.1
6	**M2**	**Ni3**	21 ± 11	16 ± 0.8	1.5 ± 0.1
7	**M2**	**Ni4**	18 ± 6.5	14 ± 1.7	1.6 ± 0.2
8	**M2**	**Ni5**	29 ± 5.2	16 ± 0.5	1.6 ± 0.1

[a]General polymerization conditions: total monomer = 0.14 mmol, catalyst = 1.4 μmol, 100 μL toluene; T_{rxn} = 20 ºC, and t = 5 h. All polymerizations were run in triplicate [b]Molecular weights and dispersity were measured using gel permeation chromatography at 40 ºC in THF and reported relative to polystyrene standards.

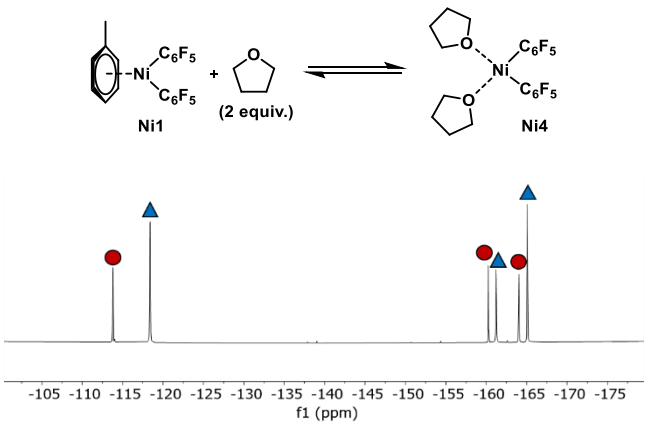

Figure 2.7. Representative example of determining K_{eq} via ^{19}F NMR spectroscopy for **Ni1** (red circles) in the presence of 2 equiv. of THF to form **Ni4** (blue triangles).

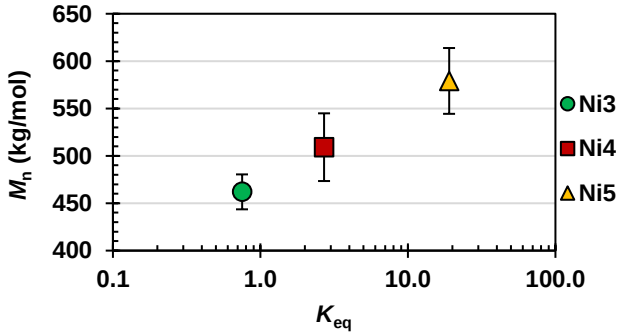

Figure 2.8. Plots of molecular weight (M_n) versus measured equilibrium constant (K_{eq}) of each $L_nNi(C_6F_5)_2$ for the polymerization of nonpolar monomer **M1**.

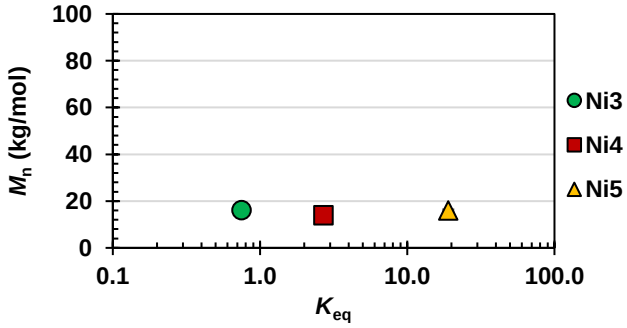

Figure 2.9. Plots of molecular weight (M_n) versus measured equilibrium constant (K_{eq}) of each $L_nNi(C_6F_5)_2$ for the polymerization of nonpolar monomer **M2**. NOTE: error bars for each data point are included in this plot but are hidden by the data markers.

These studies have focused primarily on oxygen-based ligands, due to the prevalence of polar norbornyl monomers bearing esters and ethers, for example. However, other neutral $L_nNi(C_6F_5)_2$ type complexes have recently seen increased interest for the vinyl addition of functionalized norbornenes, such as trans-$[Ni(C_6F_5)_2(SbPh_3)_2]$ (**Ni2**). This catalyst has been shown to tolerate a variety of functionalized norbornyl monomers, such as those bearing alkoxy silane-substituents,[29] and we were therefore interested in how the change in ligand type, from the hard, oxygen coordinating ligands of catalysts **Ni3**-**Ni5** to the soft stibine-based ligands of catalyst **Ni2** would impact the polymerization of monomers **M1** and **M2**.

To investigate this, we first ran equilibrium studies in which **Ni1** (1 equiv.) was mixed with $SbPh_3$ (2 equiv.) in CD_2Cl_2. The ^{19}F NMR spectrum of this mixture revealed rapid and complete ligand exchange of the toluene ligand of **Ni1** for the $SbPh_3$ ligands. The K_{eq} value was therefore unmeasurable, and its polymerization results could not be readily plotted alongside the results for catalysts **Ni3**-**Ni5**. Furthermore, ^{19}F NMR and IR spectroscopy both suggest that the coordinating $SbPh_3$ ligands are not readily displaced by **M3** or EtOAc, even when excess ester was used (See **Figures A12**, **A13**, **A17** and **A18**).

In similarity to the results observed for catalysts **Ni1** and **Ni3**-**Ni5**, polymerization of nonpolar monomers using **Ni2** produced high molecular weight polymer **P1** (M_n = 230 ± 53 kg/mol) in high yield (90-99%), whereas polymerizations of polar monomer **M2** produced only low molecular weight **P2** (M_n = 14 kg/mol ± 0.3) in low yield (18-41 %). These polymerization results mimic those of catalysts **Ni3**-**Ni5**; however, **Ni2** does not seem to follow the same trend of increasing **P1** polymer molecular weight vs. ligand strength despite **Ni2** having an infinitely stronger coordinating ligand than any of the four other catalysts (**Ni1**, **Ni3**-**Ni5**). We anticipate that this discrepancy in observed behavior is likely due to the difference of hard vs. soft

coordinating neutral ligands for catalysts **Ni3**-**Ni5** vs. **Ni2**, respectively, though further investigations will be required.

2.4 Conclusions

Norbornene-type monomers bearing polar and nonpolar functional groups were polymerized using a series of neutral, single-site nickel-based catalysts. The polymerization of the nonpolar monomer (**M1**) gave rise to high molecular weight polymer in high yield, whereas the polymerization of the polar, ester containing monomer (**M2**) gave rise to low molecular weight polymer in poor yield. The possibility of coordination/chelation of the polar functionality to the Lewis acidic metal center was investigated using IR and ^{19}F NMR spectroscopy. When two equivalents of **M2**, **M3**, or EtOAc were combined with one equivalent of **Ni1**, IR spectroscopy revealed a shift in the carbonyl stretch of the native ester to a lower frequency with symmetric and asymmetric carbonyl stretching. This, along with the shift in the ^{19}F NMR peaks of the coordinated species, suggests coordination of two molecules of **M2**, **M3**, or EtOAc in a cis fashion to the $Ni(C_6F_5)_2$ fragment.

Due to the facile displacement of the toluene ligand in **Ni1**, other $L_nNi(C_6F_5)_2$ catalysts were synthesized through simply dissolving **Ni1** in excess EtOAc, THF, or DME to yield **Ni3**, **Ni4**, and **Ni5**, respectively. To the best of the author's knowledge, **Ni3** and **Ni5** have not been previously described in the literature. These catalysts were thoroughly characterized using ^{1}H, ^{13}C, and ^{19}F NMR spectroscopy, as well as X-ray crystallography. X-ray crystallography data of **Ni3** revealed coordination of two ethyl acetate ligands via the carbonyl oxygen to the nickel center in a cis fashion, which agrees with the results obtained from IR and ^{19}F NMR spectroscopy. X-ray crystallography data of **Ni5** revealed chelation of a single DME ligand to the nickel center in a cis fashion.

Monomers **M1** and **M2** were subsequently polymerized using **Ni3**, **Ni4**, and **Ni5**, and these results were compared to the results obtained using **Ni1**. Polymerization of **M1**, again, gave rise to polymers with high molecular weights in high yield, whereas **M2** gave rise to polymers with low molecular weights in poor yield. Interestingly, polymerizations of nonpolar monomer **M1** presented a trend of increasing molecular weight as a function of ligand coordination strength, as was estimated by measured K_{eq} values. In contrast, polymerizations of ester functionalized monomer **M2** produced polymers that were not significantly different from one another in molecular weight.

Finally, the results obtained for catalysts **Ni3**-**Ni5**, which bear ligands that coordinate the Ni center via oxygen atoms, were compared to polymerizations using the Sb-coordinated catalyst **Ni2**. Again, decreased molecular weight and yield were observed for the polymerization of **M2**, as compared to **M1**. The coordination strength of this catalyst was also investigated; however, when compared to the coordinating strength of the ligands in **Ni1**, **Ni3**, **Ni4**, and **Ni5**, **Ni2** contains ligands that are infinitely stronger in their coordination strength. Surprisingly, however, this increase in ligand coordination strength did not follow the observed trend of increasing **P1** molecular weight noted for catalysts **Ni3**-**Ni5**, which we hypothesize may be due to the difference in ligand type (i.e. hard versus soft ligands). In sum, these results provide deeper insight into the discrepancies often observed when polymerizing polar vs. nonpolar norbornene-type monomers using neutral, single-site nickel catalysts, but future studies will be required to identify the exact mechanistic rationale leading to limited molecular weights and yields for the polymerization of polar monomers, such as **M2**.

2.5 Acknowledgements

EMP and BKL wish to acknowledge financial support from Promerus, LLC and NSF Award# 2203977. The authors thank Dr. Phattananawee Naloah for assistance collecting crystal data for $(EtOAc)_2Ni(C_6F_5)_2$ and $(DME)Ni(C_6F_5)_2$. CSD and VWD acknowledge NSF Chemical Instrumentation Award# 9521801 to Wake Forest for funds to purchase the X-ray diffractometer used to collect prior, unpublished data for $(EtOAc)_2Ni(C_6F_5)_2$. We thank Cheryl Burns and Steve Krumins for their technical support.

2.6 Experimental

2.6.1 Materials and Methods

All manipulations were carried out under an atmosphere of nitrogen using standard Schlenk technique or in an inert atmosphere using an MBraun glovebox filled with nitrogen gas. Monomers 5-hexylbicyclo[2.2.1]hept-5-ene (**M1**, *endo*: exo= 21:77) and t-butyl bicyclo[2.2.1]hept-5-ene-2-carboxylate (**M2**, *exo*:*endo* = 23:77) were gifted from Promerus LLC and purified via vacuum distillation from CaH_2, degassed using iterative freeze-pump-thaw cycles (3×), and stored in the glovebox prior to use. The catalyst (η^6-toluene)$Ni(C_6F_5)_2$ (**Ni1**) was gifted from Promerus LLC, stored in a glovebox, and used as received. The catalyst trans-$[Ni(C_6F_5)_2(SbPh_3)_2]$ (**Ni2**) was synthesized following literature procedure.[29, 30] Dichloromethane (CH_2Cl_2), tetrahydrofuran (THF), ethyl acetate (EtOAc), and toluene were purchased from Fischer Scientific, dried via passage through an Innovative Technologies PurSolv solvent purification system, and degassed via iterative freeze-pump-thaw cycles (3×) prior to use. Anhydrous dimethoxy ethane was purchased from Acros in Acroseal™ bottles and degassed via iterative freeze-pump-thaw cycles (3×) prior to use. Methanol for polymer precipitation was purchased from Fischer Scientific and used as received.

^{1}H NMR spectra of all monomers and polymers were obtained in $CDCl_3$ using a Varian 500 MHz spectrometer. ^{1}H NMR ^{13}C NMR, and ^{19}F NMR of all catalysts were obtained in $CDCl_3$ or CD_2Cl_2 using a Varian 500 MHz or 300 MHz spectrometer. All ^{1}H NMR spectra were referenced to the residual $CHCl_3$ peak at 7.26 ppm or the residual CD_2Cl_2 peak at 5.32 ppm. All ^{13}C NMR spectra were referenced to the residual $CDCl_3$ peaks at 77.16 ppm. IR spectra were obtained using an Agilent Technology Cary 630 FTIR with a diamond ATR sample cell. The IR spectrometer was used inside a nitrogen atmosphere glove box, and all samples were stored and analyzed under a nitrogen atmosphere. Polymer molecular weights were measured relative to polystyrene standards using Tosoh EcoSEC GPC system with a tetrahydrofuran eluent at 40 °C.

2.6.2 General Norbornene Polymerization Procedure using Ni1.

In a typical polymerization procedure, **M2** (1.0014 g, 5.2 mmol) was added to a vial equipped with a magnetic stir bar in a glovebox. A solution of **Ni1** (2.5 mg, 0.05 mmol) in 3.7 mL of toluene was prepared in a separate vial, then added to the monomer. The final concentrations of **M2** and **Ni1** were 1.37 M and 0.0138 M, respectively. The reaction mixture was stirred at room temperature for 5 h before precipitating the reaction mixture into excess methanol. The precipitate was filtered and dried under vacuum at 65 ºC overnight to yield 0.5589 g of the polymeric product (56 %).

2.6.3 Synthesis of t-Butyl bicyclo[2.2.1]hept-5-ane-2-carboxylate (M3)

In a glovebox, **M2** (3.003 g, 15.5 mmol) was dissolved in CH_2Cl_2 (10.5 mL) in a vial equipped with a stir bar. [(1,5-cyclooctadiene) iridium(tricyclohexylphosphine)(pyridine)] PF6 (Crabtree's Catalyst) (12.3 mg, 0.015 mmol) was weighed into a separate vial. The monomer solution was added to the vial containing Crabtree's catalysts. The vial containing the reaction mixture was placed in a stainless-steel Parr Reactor, sealed, and removed from glovebox. The

reactor was then charged with hydrogen gas (300 psi) and stirred overnight. The hydrogenated product was distilled under vacuum between 35-40 °C at 300 mTorr to yield 1.6913 g of **M3** (56 %) as a colorless liquid. ^{1}H NMR ($CDCl_3$): *endo*-isomer δ= 2.66 (m, 1H), 2.50 (br s, 1H), 2.24 (br s, 1H), 1.45 (s, 9 H), 1.8-1.1 (m, 8H); *exo*-isomer δ= 2.45 (br s, 1H), 2.26 (br s, 1H), 2.19 (br d, 1H), 1.43 (s, 9H), 1.8-1.1 (m, 8H). IR: ν(CO) 1724 cm^{-1}. ^{13}C NMR ($CDCl_3$): δ=175.61, 174.53, 79.80 79.68, 47.61, 46.99, 41.03, 40.78, 40.36, 37.26, 36.48, 36.14, 34.21, 31.79, 29.57, 29.24, 28.82, 28.32, 28.23, 24.77. HRMS ESI +(m/z) [M+H]+ Calculated for $C_{12}H_{20}O_2$:196.14633, Found:197.15378 CHNO elemental analysis for ($C_{12}H_{20}O_2$): C=73.09, H=9.82, O=17.19 (calculated, C= 73.43, H=10.27, O=16.30). Although these results are outside the range viewed as establishing analytical purity, they are provided to illustrate the best values obtained to date.

2.6.4 Coordination of t-Butyl bicyclo[2.2.1]hept-5-ene-2-carboxylate to (η^6-toluene)Ni(C_6F_5)$_2$ (M2 + Ni1)

In a glovebox, **Ni1** (0.1873 g, 0.39 mm) was dissolved in CH_2Cl_2 (3.6 mL) in a 50 mL Schlenk flask equipped with a magnetic stir bar to give a dark red-brown solution. The catalyst solution was cooled to -78 ºC and **M2** (0.3031 mg, 1.6 mmol) was added. The solvent and any volatile byproducts were removed under vacuum to produce 0.2218 g of an orange powder (yield = 73% if calculated assuming two equivalents of **M2** are coordinated to **Ni1** with concomitant displacement of toluene). ^{19}F NMR (CD_2Cl_2): δ= -118.6 (m, 2F), -161.8 (bs, 1F), -165.5 (bs, 2F). IR:ν(CO) 1724 cm^{-1} (free monomer), 1636 cm^{-1}, 1614 cm^{-1} (coordinated monomer).

2.6.5 Coordination of t-Butyl bicyclo[2.2.1]hept-5-ane-2-carboxylate to (η^6-toluene)Ni(C_6F_5)$_2$ (M3 + Ni1).

In a glovebox, **Ni1** (22.7 mg, 0.047 mmol) was dissolved in CH_2Cl_2 (1.0 mL) in a 5 mL Schlenk flask equipped with a magnetic stir bar to give a dark red-brown solution. **M3** (63.9 mg, 0.33 mmol) was added to the catalyst solution. The solvent and any volatile byproducts were removed under vacuum to produce 30.2 mg of orange powder (yield= 82 % if calculated assuming two equivalents of **M3** are coordinated to **Ni1** with concomitant displacement of toluene). ^{19}F NMR (CD_2Cl_2): δ= -118.6 (m, 2F), -162.0 (t, 1F), -165.9 (t, 2F). IR:ν(CO) 1638 cm^{-1}, 1615 cm^{-1}.

2.6.6 Coordination of EtOAc to Ni(C_6F_5) (η^6-toluene)Ni(C_6F_5) (EtOAc + Ni1)

In a glovebox, **Ni1** (30.1 mg, 0.062 mmol) was dissolved in ethyl acetate (1.0 mL) in a 50 mL Schlenk flask equipped with a magnetic stir bar to give a dark red-brown solution. The solvent and any volatile byproducts were removed under vacuum to produce 20.6 mg of an orange powder (yield= 58 % if calculated assuming two equivalents of EtOAc are coordinated to **Ni1** with concomitant displacement of toluene). ^{19}F NMR (CD_2Cl_2): δ -118.8 (d, 2 F), -160.4 (t, 1F), -164.5 (t, 2F). IR:ν(CO) 1662 cm^{-1}, 1647 cm^{-1}.

2.6.7 Synthesis of (EtOAc)$_2$Ni(C_6F_5)$_2$ (Ni3)

In a glovebox, **Ni1** (0.1046 g, 0.21 mmol) was dissolved in 1.8 mL ethyl acetate in a 50 mL Schlenk flask equipped with a magnetic stir bar. The reaction was stirred for 5 minutes. The solvent and any volatile byproducts were removed under vacuum to produce 0.0586 g of orange powder (yield = 56 % if calculated assuming two equivalents of EtOAc are coordinated to **Ni1** with concomitant displacement of toluene. ^{1}H NMR ($CDCl_3$) δ= 4.12 (br s, 2H), 2.64 (br s, 3H),1.21 (br s, 3H). 13C NMR (CDCl3) δ= 179.57, 150.09, 148.11, 138.24, 136.31, 135.74, 133.76, 101.51, 64.21, 22.84, 13.71. ^{19}F NMR (CD_2Cl_2): δ= -118.8 (d, 2F), -160.4 (t, 1F), -164.5

(t, 2F). IR:ν(CO) 1662 cm^{-1}, 1647 cm^{-1}. CHN elemental analysis for ($C_{20}H_{16}F_{10}NiO_4$): C=42.44, H=3.08 (calculated, C= 42.22, H=2.83)

2.6.8 Synthesis of $(THF)_2Ni(C_6F_5)_2$ (Ni4)

In a glovebox, Ni1 (0.1065 g, 22.0 mmol) was dissolved in 6 mL of THF in a 50 mL Schlenk flask equipped with a magnetic stir bar. The reaction was stirred for 5 minutes. The solvent and any volatile byproducts were removed under vacuum to produce 0.1174 g of orange powder (yield = 99 % if calculated assuming two equivalents of THF are coordinated to **Ni1** with concomitant displacement of toluene. ^{1}H NMR, ^{13}C NMR, and ^{19}F NMR spectra matched that of prior literature reports.[26]

2.6.9 Synthesis of $(DME)Ni(C_6F_5)_2$ (Ni5)

In a glovebox, **Ni1**(17.1 mg, 0.035 mmol) was dissolved in 10 mL 1,2-dimethoxy ethane in a 50 mL Schlenk flask equipped with a magnetic stir bar. The reaction was stirred for 5 minutes. The solvent and any volatile byproducts were removed under vacuum to produce 15.8 mg of orange powder (yield = 92 % if calculated assuming one equivalent of DME is coordinated to **Ni1** with concomitant displacement of toluene). ^{1}H NMR ($CDCl_3$): δ= 3.68 (br s, 4H), 3.02 (br s, 6H). ^{13}C NMR ($CDCl_3$): δ= 150.23, 148.34, 138.65, 136.70, 136.03. 133.96, 100.10, 71.65, 62.76. 19F NMR (CD_2Cl_2): δ -118.8 (d, 2 F), -160.4 (t, 1F), -164.5 (t, 2F). CHN elemental analysis for ($C_{12}H_{10}F_{10}NiO_2$): C=39.79, H=2.09 (calculated, C= 40.12, H=2.44)

2.6.10 General Method for Determination of K_{eq} Values

In a typical procedure, **Ni1** (15.7 mg, 0.03 mm) was dissolved in 700 µL of CD_2Cl_2. 10 µL of THF was mixed with 30 µL of CD_2Cl_2 (4 M). 10 µL of the THF solution was added to the catalyst solution. The solution was added to a J-Young NMR tube. NMR was obtained within 10 minutes of mixing. The peaks for the ortho-fluorines of the newly formed species were

integrated to 1. The ortho-fluorines corresponding to Ni1 were integrated and those values were used to calculate Keq as the ratio of integrated products to reactants ($K_{eq} = I_{products}/I_{reactants}$).

References

(1) Geyer, R.; Jambeck, J. R.; Law, K. L. Production, use, and fate of all plastics ever made. *Sci. Adv* **2017**, *3* (7), 1700782. DOI: 10.1126/sciadv.1700782.
(2) Keyes, A.; Basbug Alhan, H. E.; Ordonez, E.; Ha, U.; Beezer, D. B.; Dau, H.; Liu, Y. S.; Tsogtgerel, E.; Jones, G. R.; Harth, E. Olefins and Vinyl Polar Monomers: Bridging the Gap for Next Generation Materials. *Angew. Chem. Int. Ed* **2019**, *58* (36), 12370-12391. DOI: 10.1002/anie.201900650.
(3) Boffa, L. S.; Novak, B. M. Copolymerization of Polar Monomers with Olefins Using Transition-Metal Complexes. *Chem. Rev.* **2000**, *100* (4), 1479-1493. DOI: 10.1021/cr990251u.
(4) Mecking, S.; Johnson, L. K.; Wang, L.; Brookhart, M. Mechanistic Studies of the Palladium-Catalyzed Copolymerization of Ethylene and α-Olefins with Methyl Acrylate. *J. Am. Chem. Soc* **1998**, *120* (5), 888-899. DOI: 10.1021/ja964144i.
(5) Lynda K. Johnson, S. M., Maurice Brookhart. Copolymerization of Ethylene and Propylene with Functionalized Vinyl Monomers by Palladium(II) Catalyst. *J. Am. Chem. Soc.* **1996**, *118*, 267-268. DOI: 10.1021/ja953247i.
(6) Blank, F. C. J. Metal catalysts for the vinyl/addition polymerization of norbornene. *Coordination Chemistry Reviews* **2009**, *253*, 827-861. DOI: 10.1016/j.ccr.2008.05.010.
(7) Wang, C.; Friedrich, S.; Younkin, T. R.; Li, R. T.; Grubbs, R.; Bansleben, D. A.; Day, M. W. Neutral Nickel(II)-Based Catalysts for EthylenePolymerization. *Organometallics* **1998**, *17*, 3149. DOI: 10.1021/om980176y.
(8) Younkin, T. R. C., E. F.; Henerson, S. K.; Grubbs, R.; Bansleben, D. A. Neutral, Single-Component Nickel (II) Polyolefin Catalysts That Tolerate Heteroatoms. *Science* **2000**, *287*, 460-462. DOI: 10.1126/science.287.5452.460.
(9) Michalak, A. Z., T. DFT Studies on the Copolymerization of α-Olefins with Polar Monomers: Ethylene-Methyl Acrylate Copolymerization Catalyzed by a Pd-Based Diimine Catalyst. *J. Am. Chem. Soc.* **2001**, *123* (49), 12266-12278. DOI: 10.1021/ja010876l.
(10) Michalak, A. Z., T. DFT Studies on the Copolymerization of α-Olefins with Polar Monomers: Comonomer Binding by Nickel- and Palladium-Based Catalysts with Brookhart and Grubbs Ligands. *Organometallics* **2001**, *20*, 1521-1532. DOI: 10.1021/om0009886.
(11) Grove, N. R.; Kohl, P. A.; Bidstrup Allen, S. A.; Jayaraman, S.; Shick, R. Functionalized polynorbornene dielectric polymers: Adhesion and mechanical properties. *J. Polym. Sci, Part B: Polym. Phys* **1999**, *37* (21), 3003-3010. DOI: 10.1002/(sici)1099-0488(19991101)37:21<3003::aid-polb10>3.0.co;2-t.
(12) Okoroanyanwu, U. General Cosiderations on the Radiation of Photochemistry of Resists. In *Chemistry and Lithography*, SPIE, 2010; pp 395-415.
(13) Bermesheva, E. V.; Bermeshev, M. V. Single-Component Catalysts for the Vinyl-Addition Polymerization of Norbornene and its Derivatives. *ChemCatChem* **2023**, *15* (24), 1-23. DOI: 10.1002/cctc.202300818.
(14) Selhorst, R.; Gaitor, J.; Lee, M.; Markovich, D.; Yu, Y.; Treichel, M.; Olavarria Gallegos, C.; Kowalewski, T.; Kourkoutis, L. F.; Hayward, R. C.; et al. Multiblock Copolymer Anion-Exchange Membranes Derived from Vinyl Addition Polynorbornenes. *ACS Appl. Energy Mater.* **2021**, *4*, 10273-10279. DOI: 10.1021/acsaem.1c02094.
(15) Kalamarides, H. A.; Iyer, S.; Lipian, J.; Rhodes, L. F.; Day, C. Pentafluoroaryl Transfer from Tris(pentafluorophenyl)boron Hydrate to Nickel. Synthesis and X-ray Crystal Structure of

($PPh_2CH_2C(O)Ph)Ni(C_6F_5)_2$. *Organometallics* **2000**, *19* (19), 3983-3990. DOI: 10.1021/om000606w.
(16) Barnes, D. A. B., G. M.; Goodall, B. L.; Huang, S. S.; Kalamrides,H. A.; Lenhard, S.'McIntosh, L. H.; Selvy, K. T.; Schick, R. A.; Rhodes, L. F. Addition Polymerization of Norbornene-Type Monomers Using Neutral Nickel Complexes Containing Fluorinated Aryl Ligands. *Macromolecules* **2003**, *36*, 2623-2332. DOI: 10.1021/ma030001m.
(17) Funk, J. K.; Andes, C. E.; Sen, A. Addition Polymerization of Functionalized Norbornenes: The Effect of Size, Stereochemistry, and Coordinating Ability of the Substituent. *Organometallics* **2004**, *23* (8), 1680-1683. DOI: 10.1021/om049943l.
(18) Martin, J. G., Hill, R. K. Stereochemistry of the Dield-Alder Reaction. *Chem. Rev.* **1961**, *61*, 537-562. DOI: 10.1021/cr60214a001.
(19) Mathew, J. P.; Reinmuth, A.; Melia, J.; Swords, N.; Risse, W. (η3-Allyl)palladium(II) and Palladium(II) Nitrile Catalysts for the Addition Polymerization of Norbornene Derivatives with Functional Groups. *Macromolecules* **1996**, *29* (8), 2755-2763. DOI: 10.1021/ma9515285.
(20) Breunig, S.; Risse, W. Transition-metal-catalyzed vinyl addition polymerizations of norbornene derivatives with ester groups. *Die Makromolekulare Chemie* **1992**, *193* (11), 2915-2927. DOI: 10.1002/macp.1992.021931117.
(21) Potier, J.; Commarieu, B.; Soldera, A.; Claverie, J. P. Thermodynamic Control in the Catalytic Insertion Polymerization of Norbornenes as Rationale for the Lack of Reactivity of Endo-Substituted Norbornenes. *ACS Catalysis* **2018**, *8* (7), 6047-6054. DOI: 10.1021/acscatal.8b00393.
(22) Commarieu, B.; Claverie, J. P. Bypassing the lack of reactivity of endo-substituted norbornenes with the catalytic rectification–insertion mechanism. *Chem. Sci* **2015**, *6* (4), 2172-2181. DOI: 10.1039/c4sc03575e.
(23) Hennis, A. D.; Polley, J. D.; Long, G. S.; Sen, A.; Yandulov, D.; Lipian, J.; Benedikt, G. M.; Rhodes, L. F.; Huffman, J. Novel, Efficient, Palladium-Based System for the Polymerization of Norbornene Derivatives: Scope and Mechanism. *Organometallics* **2001**, *20* (13), 2802-2812. DOI: 10.1021/om010232m.
(24) Gary L. Miessler, P., J. Fischer, Donald A. Tarr. Symmetry and Group Theory. In *Inorganic Chemistry*, Fifth ed.; Pearson, 2014; pp 111-112.
(25) Catherine E. Housecroft, A. G. S. Introduction to Molecular Symmetry. In *Inorganic Chemistry*, Fourth ed.; Pearson, 2012; pp 60-86.
(26) Forniés, J.; Martín, A.; Martín, L. F.; Menjón, B.; Kalamarides, H. A.; Rhodes, L. F.; Day, C. S.; Day, V. W. Synthesis and Characterization of a New Family of Square-Planar Nickel(II) Carbonyl Derivatives. *Chem. Eur. J.* **2002**, *8* (21), 4925-4934. DOI: 10.1002/1521-3765(20021104)8:21<4925::aid-chem4925>3.0.co;2-4.
(27) George M. Benedikt, B. L. G., Suri Iyer, Lester H. McIntosh III, Richard Mimna, Larry F. Rhodes. Synthesis, Solution Dynamics, and X-ray CrystalStructure of Bis(2,4,6-tris(trifluoromethyl)-phenyl)(1,2-dimethoxyethane)nickel. *Organometallics* **2001**, *20*, 2565-2569. DOI: 10.1021/om0100784.
(28) Ponce-De-León, J.; Gioria, E.; Martínez-Ilarduya, J. M.; Espinet, P. Ranking Ligands by Their Ability to Ease $(C_6F_5)_2Ni^{II}L \rightarrow Ni^0L + (C_6F_5)_2$ Coupling versus Hydrolysis: Outstanding Activity of PEWO Ligands. *Inorganic Chemistry* **2020**, *59* (24), 18287-18294. DOI: 10.1021/acs.inorgchem.0c02831.
(29) Gmernicki, K. R.; Hong, E.; Maroon, C. R.; Mahurin, S. M.; Sokolov, A. P.; Saito, T.; Long, B. K. Accessing Siloxane Functionalized Polynorbornenes via Vinyl-Addition

Polymerization for CO_2 Separation Membranes. *ACS Macro Lett.* **2016**, *5* (7), 879-883. DOI: 10.1021/acsmacrolett.6b00435.
(30) Casares, J. A.; Espinet, P.; Martín-Alvarez, J. M.; Martínez-Ilarduya, J. M.; Salas, G. Stable Nickel Catalysts for Fast Norbornene Polymerization: Tuning Reactivity. *Eur. J. Inorg. Chem.* **2005**, *2005* (19), 3825-3831. DOI: 10.1002/ejic.200500121.

CHAPTER III: Stereochemical Effects of Addition-Type Polynorbornenes for CO_2/N_2 Separations

3.1 Abstract

3.2 Introduction

Chemical separations are an integral, yet often unappreciated facet of our society. In fact, 10-15% of the United States' energy consumption comes from chemical separations. This includes refining crude oil, separating alkenes and alkanes, and carbon capture which utilize distillation, cryogenic distillation, and amine adsorption respectively. All of these methods require heating during their processes which drives up the energy expense and cost of separation. It has been proposed that developing alternative, energy-efficient methods could reduce operational costs in the US annually by $4 billion.[1] In facilities that separate CO_2 from flue gas emissions, this is especially relevant as the release of greenhouse gases, such as CO_2 into this atmosphere has been linked to anthropogenic climate change. With energy consumption in the US expected to climb, it becomes more and more imperative to develop energy-efficient and cost-effective methods for CO_2 separations.

Dense polymeric gas separation membranes offer a passive alternative to current separation methods in industries such as carbon capture. However, due to the tradeoff relationship between permeability (pressure and thickness normalized flux) and selectivity (the preference of a membrane to permeate one gas versus another), dense polymeric membranes are limited in their implementation in an industrial setting.[2, 3] Significant advances in membrane science have been made over the past several decades, and this field has seen several noteworthy advances thanks to the growing fundamental understanding of the polymeric structure-property relationships that governs gas transport.[4-7]

Previous work in our group has investigated the relationship between the molecular structure of vinyl addition polynorbornene (VAPNB) alkoxysilyl substituent structure and gas transport properties. For example, we observed that decreasing the substituent length from tripropoxysilyl to triethoxysilyl to trimethoxysilyl leads to a simultaneous increase in permeability and selectivity.[8] This gives rise to an uncharacteristic trend in performance that is perpendicular to the 2008 upper bound. These results highlight the impact that small changes in polymer structure can have on gas transport properties and prompted a curiosity revolving around how other changes in polymer molecular structure could affect gas transport properties. The polymers presented in our previous work were synthesized from monomers containing a mixture of both the *endo*- and *exo*- norbornene monomers. Herein, we expand upon this study and investigate the effect that alkoxysilyl substituent stereochemistry has on gas transport properties through a detailed comparison of mixed alkoxysilyl norbornene monomer and their *exo*-enriched counterparts.

3.3 Results and Discussion

3.3.1 Monomer and Polymer Synthesis

The proposed mixed monomers (**M1$_{Mix}$** – **M4$_{Mix}$**) and their *exo*-enriched counterparts (**M1$_{Exo}$** – **M4$_{Exo}$**) are shown in **Scheme 3.1**. Norbornene-based monomers **M1$_{Mix}$ – M3$_{Mix}$** were synthesized via the Diels-Alder reaction between cyclopentadiene and the corresponding vinylalkoxysilane following an established procedure.[8] Monomers **M1$_{Mix}$ – M4$_{Mix}$** were purified via iterative vacuum distillation until reaching >99% purity (by NMR), yielding clear, colorless oils that are a mixture of *endo*- and *exo-isomers*. Each of the synthesized monomers were

characterized via ^{1}H NMR spectroscopy. The *exo*-enriched norbornene-based monomers (**M1$_{Exo}$ – M4$_{Exo}$**) were isolated from their corresponding *mixed* norbornene counterpart via iterative flash column chromatography until reaching >98% *exo*-enriched isomers. Each of the isolated isomers were characterized via ^{1}H NMR spectroscopy.

Monomers **M1$_{Mix}$ – M4$_{Mix}$** and **M1$_{Exo}$ – M4$_{Exo}$** were polymerized in dry DCM using the catalyst *trans*-[Ni(C_6F_5)$_2$($SbPh_3$)$_2$] to yield polymers **P1$_{Mix}$ – P4$_{Mix}$** and **P1$_{Exo}$ – P4$_{Exo}$** following previously reported procedures (**Table 3.1**).[9] These polymers exhibit excellent solubility in common organic solvents such as DCM, chloroform, THF, and toluene.

Scheme 3.1. Monomers **M1$_{Mix}$** – **M4$_{Mix}$** and **M2$_{Exo}$ - M2$_{Exo}$** as well as the synthesis of **P1$_{Mix}$** – **P4$_{Mix}$** and **M1$_{Exo}$** – **M4$_{Exo}$.**

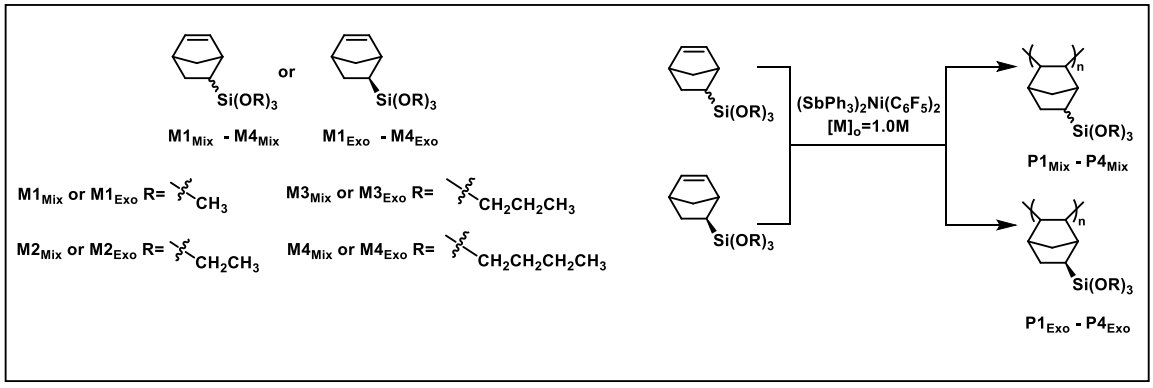

Table 3.1. Characterization of polymers.

entry	Polymer	yield (%)	M_n (kg/mol)[b]	$Đ$[b]
1	**P1$_{Mix}$**	53	118	1.9
2	**P1$_{Exo}$**	45	183	2.7
3	**P2$_{Mix}$**	63	111	2.0
4	**P2$_{Exo}$**	85	342	16.5
5	**P3$_{Mix}$**	57	88	1.9
6	**P3$_{Exo}$**	91	430	6.2
7	**P1$_{Mix}$**	56	99	1.8
8	**P4$_{Exo}$**	85	204	2.0

[a]General polymerization conditions: total monomer = 4.7 mmol, catalyst= 4.6 μmol, 4.7 mL DCM, T_{rxn}=20 ºC, and t=1 h. Polymers were purified by precipitation into MeOH. [b]Molar masses and dispersity were measured using gel permeation chromatography at 40 ºC in THF relative to polystyrene standards.

3.3.2 Gas Transport Analysis

Polymer films for gas transport measurements were cast from 3.2 wt% solutions in chloroform. These polymer-chloroform solutions were syringe filtered into cellophane covered glass dishes, which were then covered with aluminum foil, and the solvent was allowed to evaporate over several days. The procedure produced homogenous, free-standing films between 80 - 150 μm thickness.

Our group has previously investigated the structure-property relationship between alkoxysilyl chain length on vinyl addition polynorbornenes and gas transport properties. They found that as the alkoxysilyl chain length was decreased from propyl to ethyl to methyl, there was a simultaneous increase in CO_2 permeability and CO_2/N_2 selectivity.[8] We draw from this previous study to aid in investigating the structure-property relationship between stereochemistry of substituents and gas transport properties.

The density of each polymer was measured using Archimedes' principle, and those values were used to estimate fractional free volume (FFV) using the Bondi method (**Table 3.2**).[10, 11] For both the *mixed* polymer series and *exo*-enriched polymer series, the density decreases with increasing chain length. Comparing between the two series, the *exo*-enriched polymers are less dense than their *mixed* polymer counterparts in all cases. Fractional free volume (FFV) values increase with increasing chain length in both the *mixed* and *exo*-enriched polymer series. Higher FFV is seen in the *exo*-enriched polymers as compared to their *mixed* polymer counterparts. This data is shown pictorially in **Figure 3.1.** Wide-angle X-ray scattering (WAXS) revealed broad amorphous peaks for all polymers, with no sharp diffraction peaks,

suggesting that all polymers are amorphous. Calculated *d*-spacing values were not significantly different between the two-polymer series.

To gain insight into the impact stereochemistry has on gas transport properties, the ideal gas permeability and selectivity were measured using the constant-volume variable-pressure gas flux method. These values are reported below in **Table 3.3** and plotted on a log-log plot of ideal CO_2/N_2 selectivity (α) versus permeability (P) (**Figure 3.2**). As expected, permeability and selectivity decrease as alkoxy chain length increases in both series (**P1$_{Mix}$** – **P4$_{Mix}$** and **P1$_{Exo}$** – **P4$_{Exo}$**). These findings agree with what has been previously reported.[9] When comparing between the two series, there is a slight decrease in permeability of the *exo*-enriched polymers when compared to the *mixed*-polymer counterparts. Interestingly, there is no obvious trend in selectivity in comparing between the two series.

Table 3.2. Density and fractional free volume (FFV) of polymer films.

				d-spacing (Å)c			
Entry	Polymer	density (g/cm3)a	FFVb	(dB/dic)1	(dB/dic)2	(dB/dic)3	(dB/dic)4
1	**P1$_{Mix}$**	1.227	0.077	13.5/16.4	5.8/7.0	3.7/4.5	2.3/2.8
2	**P1$_{Exo}$**	1.190	0.105	13.6/16.6	6.0/7.3	4.2/5.1	2.3/2.9
3	**P2$_{Mix}$**	1.030	0.117	14.9/18.1	6.5/8.0	4.2/5.2	2.3/2.8
4	**P2$_{Exo}$**	1.117	0.144	15.0/18.3	6.5/8.0	4.2/5.2	2.3/2.8
5	**P3$_{Mix}$**	1.083	0.159	15.8/19.3	6.9/8.4	4.4/5.4	2.3/2.8
6	**P3$_{Exo}$**	1.042	0.168	15.8/19.2	6.9/8.4	4.4/5.4	2.3/2.9
7	**P1$_{Mix}$**	1.010	0.167	17.0/20.7	4.6/5.6	1.5/1.8	2.3/2.8
8	**P4$_{Exo}$**	0.980	0.192	16.6/20.3	5.0/6.1	2.4/2.9	1.8/2.1

[a]Determined using Archimedes' Principle. [b]Estimated using the Bondi method. [c]Measured using wide-angle X-ray scattering and d-spacing is calculated using Bragg's Law.

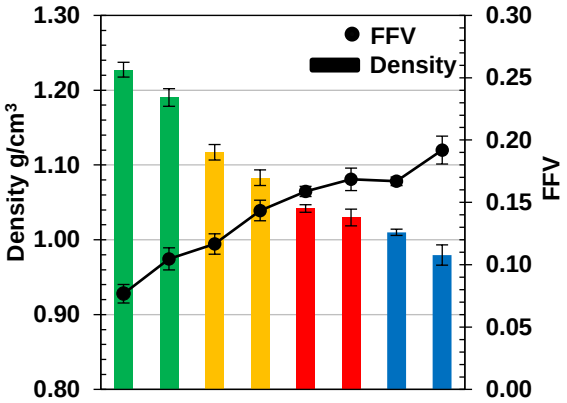

Figure 3.1. Stereochemical impact on polymer density.

Table 3.3. Ideal permeability and selectivity of the mixed and *exo*-enriched polymer series.

		P(Barrer)a		
Entry	Polymer	CO2	N2	α (CO2/N2)
1	**P1$_{Mix}$**	1449 ± 132	53 ± 7	27.2 ± 0.9
2	**P1$_{Exo}$**	1346 ± 66	49 ± 2	27.7 ± 2.1
3	**P2$_{Mix}$**	1026 ± 51	62 ± 3	16.5 ± 0.1
4	**P2$_{Exo}$**	931 ± 36	55 ±1	16.8 ± 0.1
5	**P3$_{Mix}$**	510 ± 27	35 ± 7	14.4 ± 0.3
6	**P3$_{Exo}$**	439 ± 13	36 ± 7	12.7 ± 2.1
7	**P1$_{Mix}$**	550 ± 51	43 ± 4	12.8 ± 0.2
8	**P4$_{Exo}$**	519 ± 32	42 ± 4	12.5 ± 0.8

[a]Permeability values of free-standing polymer films were obtained using the constant-volume, variable-pressure gas flux method at 20 psi upstream pressure. Ideal selectivity was calculated as a ratio of pure gas $P(CO_2)/P(N_2)$.

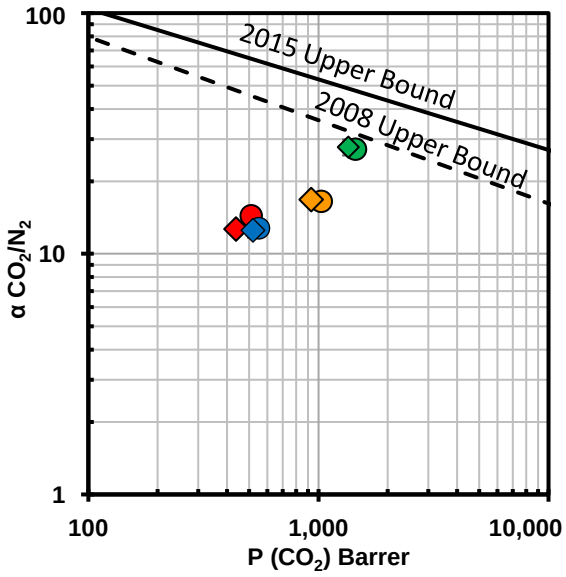

Figure 3.2. Robeson plot of polymers tested in this study. Green, orange, red, and black circles represent **P1$_{Mix}$**, **P2$_{Mix}$**, **P3$_{Mix}$**, and **P4$_{Mix}$** respectively. Green, orange, red, and black triangles represent **P1$_{Exo}$**, **P2$_{Exo}$**, **P3$_{Exo}$**, and **P4$_{Exo}$** respectively. Errors bars are included for each data point, but in some cases, the errors bars are smaller than the data marker.

To further understand potential differences between the two series of polymers, the mechanism of gas transport was investigated through analysis of the solubility and diffusivity coefficients. Pure gas sorption isotherms were collected by measuring concentration of sorbed gas as a function of pressure using the dual-volume pressure-decay method. Shown in **Figure 3.3**, the resulting isotherms were then fit using a custom Python script to either the dual-mode sorption model or linearly achieving good correlation factors ($R^2 \geq 0.999$ for CO_2 and N_2). Pure gas solubility coefficients (*S*) were then extracted from these isotherms by solving **eq 3** as pressure approaches 0 atm. The diffusion coefficients (*D*) were then determined algebraically using the experimentally determined *P* and *S* coefficients and the equation $D=P/S$ (**Table 3.4**).

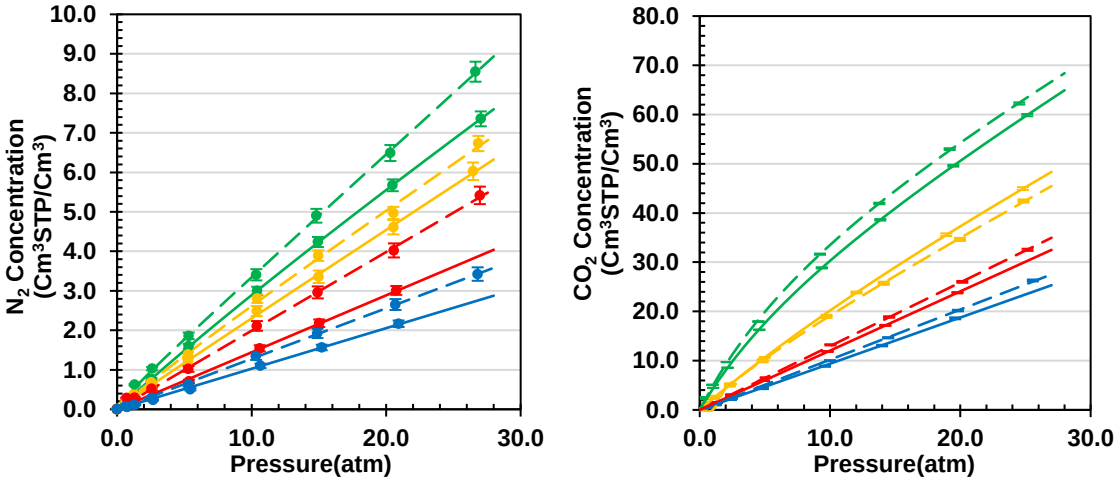

Figure 3.3. N_2 sorption isotherms (left) and CO_2 sorption isotherms (right) for polymers **P1$_{Mix}$** – **P4$_{Mix}$** and **P1$_{Exo}$** – **P4$_{Exo}$.**

Table 3.4. Diffusion and solubility coefficients of the mixed and *exo*-enriched polymer series, as well as individual Henry's Law and Langmuir sorption parameters.

	D[a] ($cm^2 \cdot s^{-1}) \cdot 10^{-6}$)			S[b] (cm^3[STP]$\cdot / cm^3 \cdot atm^1$)			CO_2		N_2	
Polymer	CO_2	N_2	D_{CO_2}/D_{N2}	CO_2	N_2	S_{CO_2}/S_{N2}	k_d	$C'_H b$	k_d	$C'_H b$
P1$_{Mix}$	2.43	1.30	1.87	4.53	0.31	14.64	1.53	2.99	0.23	0.07
P1$_{Exo}$	1.95	0.73	2.67	5.24	0.51	10.28	1.43	3.82	0.31	0.20
P2$_{Mix}$	3.41	1.87	1.83	2.29	0.25	9.16	1.30	0.99	0.22	0.03
P2$_{Exo}$	2.94	1.44	2.03	2.41	0.29	8.32	1.41	0.99	0.23	0.06
P3$_{Mix}$	3.22	1.84	1.75	1.20	0.14	8.57	1.20	—[c]	0.14	—[c]
P3$_{Exo}$	2.58	1.37	1.87	1.29	0.20	6.50	1.29	—[c]	0.20	—[c]
P1$_{Mix}$	4.46	3.18	1.40	0.94	0.10	9.40	0.94	—[c]	0.10	—[c]
P4$_{Exo}$	3.87	2.50	1.55	1.02	0.13	7.97	1.02	—[c]	0.13	—[c]

[a]Diffusion coefficients (D) were determined algebraically using the D=P/S. [b]Solubility coefficients (S) were measured using the dual-volume pressure decay method and reported as pressure approaches 0. [C]Not applicable as these isotherms were fit linearly.

Through comparative analysis of solubility and diffusivity coefficients with permeability, our group has previously reported a decrease in the solubility coefficient with increasing alkoxysilyl chain length giving rise to the overall decrease seen in permeability. This is primarily due to the decreased Henry's law of dissolution and Langmuir contributions as longer; flexible chains occupy the excess free volume within the polymer matrix. Conversely, it is the diffusivity selectivity that primarily drives the decrease in overall selectivity.[8]

Comparing the two series, there seems to be a counterbalance between the diffusivity coefficient and the solubility coefficient, wherein the diffusivity coefficient is decreased in the *exo*-enriched polymers compared to the mixed-polymer counterparts, yet the solubility coefficient is comparably greater. This increase in solubility arises from an increase in Henry's Law of dissolution for both gases in the exo-enriched polymer series. This, as well as the greater Langmuir contributions, give rise to an overall increase in solubility for *exo*-enriched polymers compared to mixed-polymers. We hypothesize that the stereoregularity of the exo-enriched polymer series prevents the alkoxysilyl chains from occupying excess free volume as readily as the mixed-polymer series, thereby increasing the overall Langmuir contribution and, in turn, solubility of the exo-enriched polymers. The diffusivity of both gas pairs is decreased for the *exo*-enriched polymers. We hypothesize that this is due to the increased stereoregularity inhibiting segmental motions and preventing the formation of transient voids within the polymer matrix. By comparing the diffusivity coefficient and solubility coefficients to permeability, we can conclude that the decrease in permeability seen for the exo-enriched polymers is primarily due to the decrease in their diffusivity.

The lack of a definitive trend when comparing the selectivity of the exo-enriched polymer series to the mixed-polymer series is better understood when comparing the diffusivity selectivity and solubility selectivity of the gas pair. The diffusivity selectivity of the exo-enriched polymers is slightly higher than the mixed-polymer series. The solubility selectivity directly contradicts this with the exo-enriched polymers having a slightly greater solubility selectivity than the mixed-polymer series. Because neither diffusivity selectivity nor solubility selectivity dominate, the overall selectivity between the two series is not greatly affected.

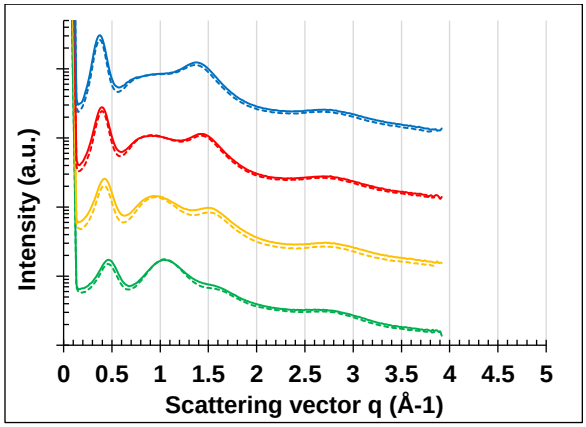

Figure 3.4. WAXS spectrum of mixed polymer series and *exo*-enriched polymer series.

3.4 Conclusions

3.5 Acknowledgements

3.6 Experimental

3.6.1 General Materials and Methods

All air-sensitive reactions were conducted under an inert atmosphere using an MBraun glovebox and a dry nitrogen atmosphere, unless noted otherwise. All monomers were synthesized using standard laboratory techniques and worked up in air. Synthesized monomers were dried using CaH_2, purified by vacuum distillation, degassed via iterative freeze-pump-thaw cycles (3X), and stored over 3 Å molecular sieves in the glovebox prior to use. Dicylcopentadiene was purchased from Acros Organics and used as received. Hydroquinone, hexanes and methanol for polymer precipitations, as well as chloroform for film casting were purchased from Fisher Scientific and used as received. Trimethoxyvinylsilane and triethoxyvinylsilane were all ordered from Gelest and used as received. Tripropoxyvinylsilane and tributoxyvinylsilane were synthesized according to literature procedure.[12] Dichloromethane (DCM) was purchased from Fisher Scientific, dried via passage through and Innovative Technologies PureSolv solvent purification system, and degassed via iterative freeze-pump-thaw cycles (3X) prior to use. Triphenylantimony, and nickel (II) bromide dimethoxyethane adduct were purchased from Strem and stored in the glovebox prior to use. N-Butyllithium (2.5 M in hexanes) was purchased from Fisher Scientific, and cannula transferred to Schlenk glassware for storage and air-free handling. The catalyst *trans*-$[Ni(C_6F_5)_2(SbPh_3)_2]$ was synthesized following literature procedure.[9]

3.6.2 Monomer and Polymer Characterization

The monomers bicyclo[2.2.1]hept-5-en-2-yltrimethoxysilane (**M1$_{Mix}$**, *exo: endo*= 65:35), bicyclo[2.2.1]hept-5-en-2-yltriethoxysilane (**M2$_{Mix}$**, *exo: endo*= 65:35), bicyclo[2.2.1]hept-5-en-2-yltrimpropoxysilane (**M3$_{Mix}$**, *exo: endo*= 65:35), and bicyclo[2.2.1]hept-5-en-2-yltributoxysilane (**M4$_{Mix}$**, *exo: endo*= 65:35) were synthesized via the Diels-Alder reaction following established literature procedures.[9, 12] The *exo*-isomer of monomers **M1$_{Mix}$ – M4$_{Mix}$** were obtained by running iterative columns (EtOAc:hexanes= 2:98)until ≥98% *exo*-isomer was isolated as confirmed *via* NMR (Figure SX-SX). ^{1}H NMR spectra of all monomers and polymers were obtained in $CDCl_3$ using a Varian 500 MHz spectrometer. All ^{1}H NMR spectra were referenced to the residual $CHCl_3$ peaks at δ= 7.26 ppm. Polymer molar masses and dispersities were measured relative to polystyrene standards using Tosoh EcoSEC GPC system with a tetrahydrofuran eluent at 40 °C. Polymer densities were determined via the Archimedes principle using a Mettler Toledo MS-DNY-43 density kit interfaced with a Mettler Toledo MS204S analytical balance.

3.6.3 Membrane Preparation

Membranes of all polymers discussed herein were prepared by solution casting from 3.2 wt% polymer solution in CHCl3. As an example, 10 mL of CHCl3 was added to a vial containing 0.5 g of polymer and a PTFE coated magnetic stir bar. This mixture was stirred until the polymer fully dissolved. The resulting polymer solution was filtered through a 0.45 μm PTFE syringe filter into a 6.5 cm diameter, cellophane-bottom dish. The dishes were covered with aluminum foil to allow for slow evaporation of solvent. The free-standing membranes were removed from their casting dishes after slowly evaporating for 48-72 h.

3.6.4 Permeation Analysis

Pure gas flux was measured using a custom-built, constant-volume, variable-pressure permeation instrument. Flux measurements were used to calculate permeability coefficients according to **eq. 1**.

$$\boldsymbol{P = \frac{V_d l}{P_u A R T}\left[\left(\frac{dp}{dt}\right)_i - \left(\frac{dp}{dt}\right)_{leak}\right]} \quad \textbf{(1)}$$

Downstream volumes (V_d) were determined through sequential Burnett expansions using He gas, as reported in the literature.[13] Membrane thicknesses (l) were directly measured using a Mitutoyo 293-832-30 digital micrometer and typically ranged between 80 and 150 μm. Upstream pressure (P_u) was recorded as a time weighted average for the duration of steady state flux measurements. Effective membrane surface area (A) was measured using the open-source image analysis software platform ImageJ, using images generated with an Epson Perfection V19 flatbed scanner. An example of membrane surface area can be found in the Supporting Information (Figure SX). $R = 0.278 \frac{[cm \cdot Hg \cdot cm^3]}{[cm^3(STP) \cdot K]}$. Temperature (T) was recorded using an analog alcohol thermometer mounted directly outside the permeation cell.

3.6.5 Determination of Diffusivity and Solubility

According to the solution-diffusion model of gas transport in dense polymeric membranes, membrane permeability is the product of its solubility and diffusivity coefficients, as described by **eq. 2**. To determine individual solubility and diffusivity coefficients, sorption isotherms were generated for each membrane material using a custom-built dual-volume, dual-transducer pressure decay instrument. The concentration of absorbed gas was calculated as described by Koros and Paul.[14] Sorption isotherms were fit either linearly or to **eq. 3** using a

custom python script utilizing a truncated Newtonian curve fitting method. Solubility coefficients were then calculated as p→ 0 using the k_d, C'_H, and b parameters determined through curve fitting. With both P and S measured directly, diffusivity coefficients D were determined algebraically using **eq. 2.**

$$\boldsymbol{P = S \cdot D} \tag{2}$$

$$\boldsymbol{S = \frac{C}{P} = k_d + \frac{C'_H b}{1+bp}} \tag{3}$$

3.6.6 General polymer Synthesis

All polymerizations were conducted in a MBraun glovebox using *trans*-[Ni(C_6F_5)$_2$($SbPh_3$)$_2$] as the vinyl-addition catalyst in dry and degassed DCM. For example, **P1$_{Mix}$** was synthesized adding 910 μL of a catalyst solution (5.1 mM) to a stirred solution of **M1$_{Mix}$** (1.0 g, 4.7 mmol) in DCM (4.7 mL). The polymerization was stirred for 1 hour before being removed from the glovebox, diluted with an additional 3 mL of DCM, and precipitated into excess stirred methanol. The resultant polymer was isolated via vacuum filtration and dried *in-vacuo* to constant weight (isolated yield= 52%, M_n= 118 kg/mol, $Đ$= 1.9.

3.6.7 Wide Angle X-Ray Scattering

Polymers were illuminated at normal incidence (transmission through the film) using a Xenocs GeniX 3D microfocus source with a copper target (wavelength λ=0.154 nm) under ambient conditions). The sample-detector distance was 0.045 m. A Pilatus3 R_300 K detector (Dectris) was used with pixel size of 172 μm × 172μm. The data acquisition time was 5 min. The two-dimensional images from each measurement were azimuthally integrated to yield one-

dimensional scattering profiles of intensity *I* (au) versus scattering vector *q* ($Å^{-1}$). Interchain distances were calculated via Bragg's law (**eq 4.**) to give d_B or a modified form of the Bragg law (**eq 5**) in which a correction factor of 1.22 is applied to give d_{ic}. This correction factor has been proposed to reflect interchain spacing more accurately for polymeric materials[15, 16].

$$\boldsymbol{d_B = \frac{\lambda}{2\,sin\,\Theta}} \quad (4)$$

$$\boldsymbol{d_B = \frac{1.22\lambda}{2\,sin\,\Theta}} \quad (5)$$

References

(1) Sholl, D. S.; Lively, R. P. Seven Chemical Separations to Change the World. *Nature* **2016**, *532* (7600), 435-437. DOI: 10.1038/532435a.
(2) Freeman, B. D. Basis of Permeability/Selectivity Tradeoff Relations in Polymeric Gas Separation Membranes. *Macromolecules* **1999**, *32* (2), 375-380. DOI: 10.1021/ma9814548.
(3) Robeson, L. M. Correlation of Separation Factor Versus Permeability for Polymeric Membranes. *Journal of Membrane Science* **1991**, *62* (2), 165-185. DOI: 10.1016/0376-7388(91)80060-j.
(4) Robeson, L. M. The Upper Bound Revisited. *Journal of Membrane Science* **2008**, *320* (1-2), 390-400. DOI: 10.1016/j.memsci.2008.04.030.
(5) Swaidan, R.; Ghanem, B.; Pinnau, I. Fine-Tuned Intrinsically Ultramicroporous Polymers Redefine the Permeability/Selectivity Upper Bounds of Membrane-Based Air and Hydrogen Separations. *ACS Macro Letters* **2015**, *4* (9), 947-951. DOI: 10.1021/acsmacrolett.5b00512.
(6) Comesana-Gandara;, B.; Chen;, J.; Bezzu;, C. G.; Carta;, M.; Rose;, I.; Ferrari;, M.-C.; Eliza Esposito; Allessio FUoco; McKeown, J. C. J. N. B. Redefining the Robeson Upper Bounds for CO_2/CH_4 and CO_2/N_2 Separations Using a Series of Ultrapermeable Benzotriptycene-based Polymers of Intrinisic Microporosity. *Energy Environ. Sci.* **2019**, *12*, 2733-2740.
(7) Budd, P.; Msayib, K.; Tattershall, C.; Ghanem, B.; Reynolds, K.; McKeown, N.; Fritsch, D. Gas Separation Membranes from Polymers of Intrinsic Microporosity. *Journal of Membrane Science* **2005**, *251* (1-2), 263-269. DOI: 10.1016/j.memsci.2005.01.009.
(8) C. R. Maroon, J. T., M. A. Higgins, D. J. Harrigan, B. J. Sundell, J. A. Lawrence III, J. T. O'Brien, D. O'Neal, K. D. Vogiatzis and B. K. Long. Addition-type alkoxysilyl-substituded polynorbornenes for post-combstion carbon dioxide separations. *J. Membr. Sci.* **2020**, *595*, 117532.
(9) Gmernicki, K. R.; Hong, E.; Maroon, C. R.; Mahurin, S. M.; Sokolov, A. P.; Saito, T.; Long, B. K. Accessing Siloxane Functionalized Polynorbornenes via Vinyl-Addition Polymerization for CO_2 Separation Membranes. *ACS Macro Lett.* **2016**, *5* (7), 879-883. DOI: 10.1021/acsmacrolett.6b00435.
(10) Bondi, A. van der Waals Volumes and Radii. *The Journal of Physical Chemistry* **1964**, *68* (3), 441-451. DOI: 10.1021/j100785a001.
(11) Wu, A. X.; Lin, S.; Mizrahi Rodriguez, K.; Benedetti, F. M.; Joo, T.; Grosz, A. F.; Storme, K. R.; Roy, N.; Syar, D.; Smith, Z. P. Revisiting Group Contribution Theory for Estimating Fractional Free Volume of Microporous Polymer Membranes. *J. Membr. Sci.* **2021**, *636*, 119526. DOI: 10.1016/j.memsci.2021.119526.
(12) Wang, X.; Wilson, T. J.; Maroon, C. R.; Laub, J. A.; Rheingold, S. E.; Vogiatzis, K. D.; Long, B. K. Vinyl-Addition Fluoroalkoxysilyl-Substituted Polynorbornene Membranes for CO_2/CH_4 Separation. *ACS Appl. Polym. Mater* **2022**, *4* (11), 7976-7988. DOI: 10.1021/acsapm.1c01833.
(13) Czichos, H. S., T.; Smith, L. *Springer Handbook of Materials Measurement Methods*; 2006.
(14) Koros, W. J. P., D. R. Design considerations for measurement of gas sorption in polymers by pressure decay. *J. Polym. Sci. Phys. Ed.* **1976**, *14* (10), 1903-1907. DOI: 10.1007/978-3-540-30300-8.

(15) Klug, H. P. A., L. E. *X-Ray Diffraction Procedures: For Polycrystalline and Amorphous Materials, 2nd ed.*; 1974.
(16) Sundell, B. J.; Lawrence Iii, J. A.; Harrigan, D. J.; Vaughn, J. T.; Pilyugina, T. S.; Smith, D. R. Alkoxysilyl functionalized polynorbornenes with enhanced selectivity for heavy hydrocarbon separations. *RSC Advances* **2016**, *6* (57), 51619-51628. DOI: 10.1039/c6ra10383a.

CHAPTER IV: Synthesis and Evaluation of Segmented Block Copolymer Gas Separation Membranes

4.1 Abstract

The development of polymers of intrinsic microporosity (PIMs) has marked a paradigm shift in the field of gas separation membranes. The rigid and kinked nature of the PIM backbone prevents polymer chain packing allowing for the formation of micropores within the polymer matrix that subsequently provides for a molecular sieving effect that gives rise to exceptional gas transport properties for several gas pairs. Notably, PIMs have been marked as a primary contributor to the revision of Robeson's upper bound in recent years. Despite the surge of research that has followed the initial development of PIM-1, rapid and extensive physical aging along with poor mechanical properties due to the brittle nature of these membranes has remained problematic. To mitigate these issues, our research aims to develop segmented block copolymers using **PIM-1** and ROMP polynorbornene (**PNB**) to investigate the effects of adding rubbery units on gas transport properties, physical aging, and mechanical properties. To do so, we have created two series of copolymers to explore the effects of increased concentration of **PIM-1** into the ROMP **PNB** backbone (Series 1), and conversely, the effects of increased ROMP **PNB** into the **PIM-1** backbone (Series 2). Through this systematic study we have found that while overall permeability and selectivity are expectedly decreased for both series, minimal to no physical aging is observed over a three-month period. Additionally, the tailored incorporation of ROMP **PNB** into the **PIM-1** backbone (and vice versa) allows for tunable mechanical properties with limited effect on permeability and selectivity. Overall, we offer an additional avenue by which to tune gas transport properties while simultaneously tailoring physical aging and mechanical properties. We suspect that through simple modifications of rubbery and microporous units

incorporated, these properties can be further tuned to provide insight into the structure-property relationship that governs gas transport.

4.2 Introduction

Dense polymeric membranes offer an energy efficient and low-cost alternative to current separation methods in several industries including natural gas purification, carbon capture, and hydrogen recovery.[1, 2] A common limitation of polymeric membranes, however, is the tradeoff relationship between permeability (pressure and thickness normalized flux) and selectivity (the preference of a membrane to permeate one gas over another gas).[3, 4] Research has heavily focused on methods to ease the effects of this tradeoff relationship. In 2004, polymers of intrinsic microporosity (PIMs) were introduced in the work of Budd and McKeown.[5, 6] This new class of polymers showcased a ladder-like backbone with random bends at spiro-centers giving rise to a uniquely inflexible and contorted structure. The rigidity and points of contortion present in the backbone prevent efficient chain packing and give rise to microporosity (pores <2 nm). Films cast from these materials subsequently showcase exceptional gas transport properties for several gas pairs, with permeability and selectivity values that surpass the former 1991 Robeson upper bound and contribute to Robeson's 2008 revision of the upper bound.[5, 7] As a consequence of the exceptional gas transport properties exhibited for PIM-1 and PIM-7, there has been a surge of research focused on the development of PIM derivatives.[8]

Despite their remarkable gas transport properties, PIMs are notorious for undergoing rapid and extensive physical aging. The large amount of nonequilibrium free volume present within the polymer matrix leads to high permeability; however, this same free volume densifies over time leading to significant decreases in permeability and corresponding increases in

selectivity. While this phenomenon is common in all glassy polymers, PIMs exhibit physical aging at an advanced rate due to the excessive amount of free volume present in its backbone.[9] In addition to rapid and extensive physical aging, the rigid backbone in PIMs gives rise to poor mechanical properties-notably these materials are highly brittle.[10-12]

While great strides have been made in the design of PIMs in the past 20 years, the issues of physical aging and poor mechanical properties persist. A common approach to mitigate these issues has been to form blends, copolymers, and mixed matrix membranes with PIMs.[13-15] One such example comes from the work of Filiz and coworkers in which they completed a comprehensive study of the effects of adding polyethylene glycol (PEG) to PIM-1 through the formation of blends, diblocks, multiblocks, and side chain units of PEG from the backbone of PIM-1.[16] Inspired by this work, we were interested in further studying how the addition of rubbery units into the backbone of PIMs affects the material's gas transport properties, physical aging, and mechanical properties. To investigate this, we propose synthesizing segmented block copolymers of **PIM-1** with hexyl polynorbornene (**PNB**) in varying concentrations of the two polymers as depicted in **Figure 4.1**. We hypothesize that the addition of rubbery units will lead to an overall decrease in permeability, but that this reduction in initial gas transport properties will be accompanied by a decrease in the rate of physical aging and improved mechanical properties. Indeed, we show that greater concentrations of **PNB** into the copolymer backbone decreased permeability. However, we also note that permeability and selectivity are largely unaffected over a three-month period and the ductility of the films increases leading to highly flexible and easy to handle materials.

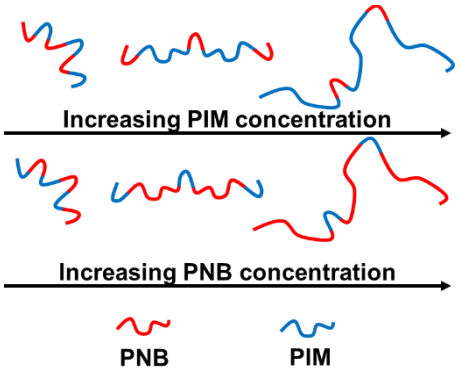

Figure 4.1. Pictorial representation of copolymer series tested in this study.

4.3 Results and Discussion

4.3.1 Polymer Synthesis and Characterization

When deciding on a suitable route for the synthesis of our copolymers, the choice of the PIM unit and the rubbery unit were of utmost importance. We envisioned applying similar conditions used for the synthesis of **PIM-1**[11] to link our two polymeric units together. Specifically, we aimed to end-functionalize one of our homopolymers with aromatic fluorines and the other with aromatic alcohols (catechols) to promote linkage through nucleophilic aromatic substitution. The synthesis of **PIM-1** offers a viable route to end-functionalization due to the step-growth nature of the polymerization. It is well known that the Carothers equation can be modified to account for stoichiometric imbalance of monomer incorporation (**eq 1**).[17]

$$\overline{X}_n = \frac{1+r}{1+r-2rp} \qquad \textbf{(eq 1)}$$

Here, *r* represents stoichiometric imbalance of one monomeric species over another and can be used to determine the degree of polymerization. Therefore, we used stoichiometric excess of tetrafluorophthalonitrile (**DCTB**) to not only control molar mass, but also preferentially endcap **PIM-1** with the **DCTB** monomer as shown in **Scheme 4.1**. Three **PIM-1** homopolymers

with molar masses of 10 kg/mol (**P^{10}**), 25 kg/mol (**P^{25}**), and 40 kg/mol (**P^{40}**) kg/mol were synthesized (**Table 4.1**).

A requirement for our rubbery unit was that it should be functionalized with catechol groups so that future copolymerization synthesis could proceed through nucleophilic aromatic substitution. Ring opening metathesis polymerization (ROMP) is a technique used to polymerize cyclic monomers while maintaining the double bond within the polymer backbone. When norbornene and norbornene derivatives are polymerized via ROMP, the conservation of the double bond within the backbone gives rise to rubbery polymers. Norbornene offers additional benefits in that functional groups on the monomer are easily tailored to allow for facile alteration of polymer properties. This provides future avenues for investigating substituent effects on gas transport properties. Finally, ROMP offers an efficient route to end-functionalize polymers through incorporation of a chain transfer agent (CTA). Several groups have shown that adding symmetric or asymmetric olefins, along with a Grubbs catalyst, yields telechelic polymers in situ.[18, 19] While there are a number of effective CTAs reported in the literature and available commercially, we were unable to find a suitable option for our needs. Therefore, we synthesized (Z)-but-2-ene-1,4-diyl bis(3,4-dihydroxybenzoate) (CTA-1), a new symmetric CTA containing catechol functional groups. The synthesis of CTA-1 is outlined in the experimental section. Subsequently, we proceeded with synthesizing our rubbery units through the polymerization of 5-hexylbicyclo[2.2.1]hept-5-ene (NB) using Grubbs second generation catalyst (GII), and CTA-1 to yield polyhexylnorbornene (PNB) (**Scheme 4.2**). By controlling the ratio of NB:CTA-1:GII, a series of telechelic PNB's was successfully synthesized with increasing molar masses of 10 kg/mol (NB10), 25 kg/mol (NB25), and 40 kg/mol (NB40) (**Table 1**).

Scheme 4.1. General Synthesis of **PIM-1** Homopolymers.

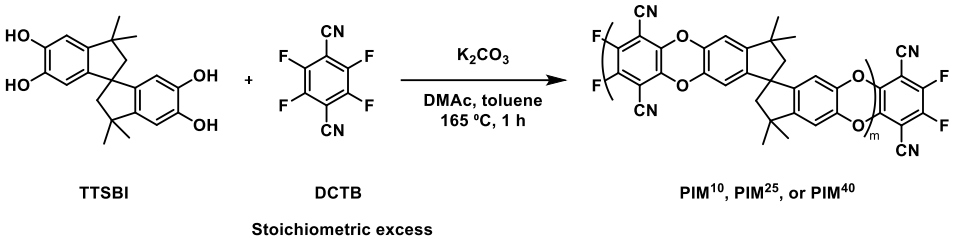

Scheme 4.2. General synthesis of **PNB** Homopolymers.

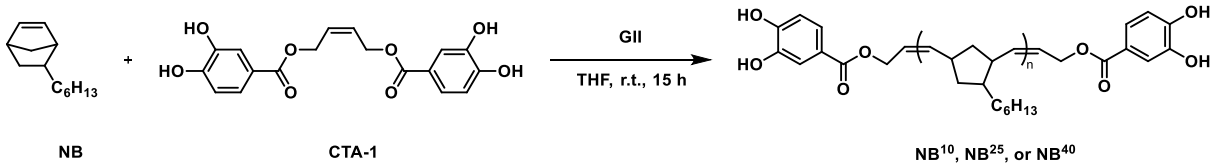

Scheme 4.3. General Synthesis of Copolymers.

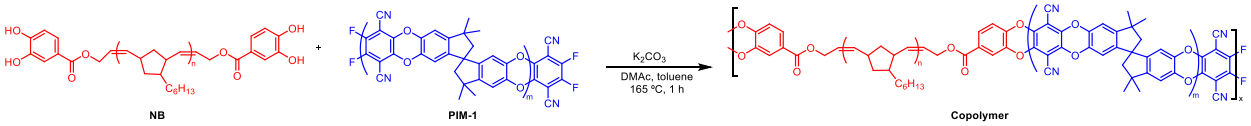

Copolymers were synthesized through a nucleophilic aromatic substitution of **PIM-1** and **PNB** homopolymers using a procedure similar to that used for the polymerization of **PIM-1** (**Scheme 4.3**). All three of the **PIM-1** homopolymers were polymerized with the three **PNB** homopolymers to yield a total of nine copolymers. Copolymers were named using the molar mass of the **PNB** unit and the molar mass of the **PIM-1** unit. For example, a copolymer synthesized from $\mathbf{PNB^{10}}$ and $\mathbf{PIM^{25}}$ would be named $\mathbf{P^{10:25}}$. All nine copolymers were analyzed via ^{1}H NMR spectroscopy along with diffusion order spectroscopy (DOSY) and gel permeation chromatography (GPC) to confirm attachment of the two polymeric units (**Table 4.1**). All DOSY spectra show protons from the **PIM-1** segment and the **PNB** segment diffusing at similar rates which is indicative of these protons being attached to the same polymeric structure. Upon GPC analysis, however, it was noted that the experimental molar mass was suspiciously lower thanexpected based on the molar mass of the starting homopolymers. For example, $\mathbf{P^{40:40}}$ (**Table 4.1**, entry 15) was synthesized using $\mathbf{PIM^{40}}$ and $\mathbf{PNB^{40}}$, yet the molar mass of the final copolymer was 54 kg/mol, and the dispersity was 2.2. Based on these results and those found through DOSY analysis, we believe that, while a portion of the homopolymers had reacted with one another to form copolymers, there remains unreacted homopolymer in the mixture. This is not unsurprising considering the step-growth nature of polymerization and the need for stringent molar equivalencies of each homopolymer. Unlike monomers, however, the homopolymers **PIM-1** and **PNB** have disperse molar masses, and accurate calculation of 1:1 stoichiometric equivalence is nearly impossible. This, in turn, leads to a low degree of polymerization and unreacted homopolymers within the copolymer mixture.

Table 4.1. Characterization of all Homopolymers and Copolymers.

Entry	polymer	yield (%)	M_n (kg/mol)[a]	$Đ$[a]	T_d (°C)	T_g (°C)
1	**PIM^{10}**	93	9.4	1.7	394	–[b]
2	**PIM^{25}**	99	25	1.9		–[b]
3	**PIM^{40}**	57	42	1.8	474	–[b]
4	**NB^{10}**	80	15	1.9	411	-10.2
5	**NB^{25}**	66	28	1.6		-11.1
6	**NB^{40}**	67	45	1.7	412	-11.0
7	**P$^{10:10}$**	88	36	1.7	416	-8.3
8	**P$^{10:25}$**	91	48	3.3		-10.4
9	**P$^{10:40}$**	91	63	2.2	402	-9.2
10	**P$^{25:10}$**	86	46	1.6		-10.0
11	**P$^{25:25}$**	87	42	2.7		-9.7
12	**P$^{24:40}$**	72	90	3.1		-6.4
13	**P$^{40:10}$**	75	65	2.2	415	-10.3
14	**P$^{40:25}$**	85	52	1.8		-7.3
15	**P$^{40:40}$**	78	54	2.2		-9.2

[a]Molar masses and dispersity were measured using gel permeation chromatography at 40 C in THF relative to polystyrene standards. [b]Glass transition temperature was undetectable by DSC analysis.

4.3.2 Gas Transport Properties

Initially, we were interested in testing the gas transport properties of all nine copolymers as well as **PIM-1**. This thorough analysis would give us information on how increasing the concentration of **PIM-1** vs. increasing the concentration of **PNB** affects gas transport properties. Polymer films for gas transport measurements were cast from 3.2 wt% solutions in chlorobenzene. We noted early on that low vapor pressure solvents such as chloroform and tetrahydrofuran (THF) evaporated at too fast of a rate and led to cracked or deformed films. We found that higher vapor pressure solvents such as chlorobenzene evaporated at a rate slow enough to prevent this. The polymer-chlorobenzene solutions were syringe-filtered into cellophane covered dishes, which were then covered with a Kimwipe, and the solvent was allowed to evaporate for 10 days. For many of the films cast, we noticed macrophase separation occurring after film formation. This was particularly prevalent in the copolymers $\mathbf{P^{25:25}}$, $\mathbf{P^{25:40}}$, $\mathbf{P^{40:25}}$, and $\mathbf{P^{40:40}}$. Notably, these were the copolymers that displayed unexpectedly low molar masses and are believed to contain a high percentage of unreacted homopolymer based on GPC results. Due to their macrophase separation, these four copolymers were deemed unfit to be tested, and we continued the study with the remaining five copolymers ($\mathbf{P^{10:10}}$, $\mathbf{P^{10:25}}$, $\mathbf{P^{10:40}}$, $\mathbf{P^{25:10}}$ $\mathbf{P^{40:10}}$). The three copolymers $\mathbf{P^{10:10}}$, $\mathbf{P^{10:25}}$, and $\mathbf{P^{10:40}}$ (Series 1) were used to investigate the effect of increasing **PIM-1** molar mass on gas transport properties while **PNB** molar mass remained unchanged (i.e., increasing **PIM-1** concentration). Conversely, the three copolymers, $\mathbf{P^{10:10}}$$\mathbf{P^{25:10}}$, and $\mathbf{P^{40:10}}$ (Series 2), were used to investigate the effect of increasing **PNB** molar mass on gas transport properties while **PIM-1** molar mass remained unchanged (i.e., increasing the concentration of **PNB**).

The density of each copolymer was measured using Archimedes' principle, and those values were used to estimate fractional free volume (FFV) using the Bondi method (**Table 4.2**). There were no clear trends in density or FFV for either Series 1 or Series 2; however, there was an overall decrease in density and an increase in FFV in the copolymers as compared to pure **PIM-1**. To gain insight into the impact **PNB** incorporation has on gas transport properties, the ideal gas permeability was measured using a constant-volume, variable pressure gas flux method. These values are reported in **Table 4.2** and are plotted on a log-log plot of ideal CO_2/N_2 selectivity (α) vs. CO_2 permeability (P) (**Figure C30**). Permeability was overall decreased in the copolymers as compared to pure **PIM-1**. In Series 1, as the concentration of **PIM-1** is increased there is an increase in permeability for CO_2. In Series 2, as the concentration of **PNB** is increased, the permeability for CO_2 remains relatively constant (**Figure 4.2**).

Table 4.2. Ideal Permeability and Selectivity of Polymers.

				P(Barrer)[c]		
Entry	Polymer	density (g/cm^3)[a]	FFV[b]	CO_2	N_2	α (CO_2/N_2)
1	$P^{10:10}$	0.93±0.07	0.39±0.04	64±4	3.7±0.7	17±3
2	$P^{10:25}$	1.1±0.03	0.28±0.02	75±6	3.3±0.4	23±2
3	$P^{10:40}$	1.0± 0.03	0.31±0.02	288±5	14±3	21±5
4	$P^{25:10}$	1.0 ±0.02	0.35±0.01	50±1	2.5±0.1	20±0.63
5	$P^{40:10}$	0.90±0.01	0.41±0.01	51±6	3.1±0.4	17±3
6	PIM-1	1.2±0.01	0.26±0.01	683±92	27±3.1	25±1.0

[a]Determined using Archimedes' Principle. [b]Estimated using the Bondi method. [c]Permeability values of free-standing polymer films were obtained using the constant-volume, variable-pressure gas flux method at 20 psi upstream pressure. Ideal selectivity was calculated as a ratio of pure gas $P(CO_2)/P(N_2)$.

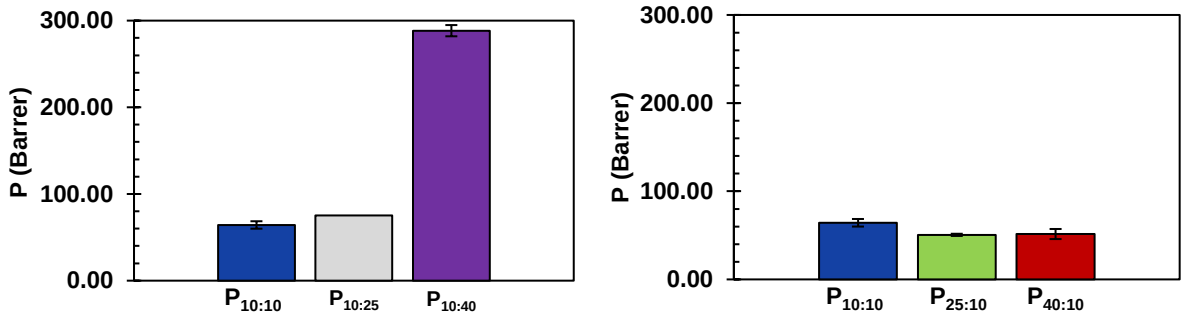

Figure 4.2. Comparison of permeability vlaues for copolymer series of increasing **PIM** concetration (left) and copolymer series of increasing **PNB** concentration (right).

To further understand potential differences between the two series of polymers, the mechanism of gas transport was investigated through analysis of solubility and diffusivity coefficients. Pure gas sorption isotherms were collected by measuring concentration of sorbed gas as a function of pressure using the dual-volume pressure-decay method. Shown in **Figure C31**, the resulting isotherms were then fit using a custom Python script to either the dual-mode-sorption model or linearly achieving good correlation factors ($R^2 \geq 0.999$ for CO_2 and N_2). Pure gas solubility coefficients (S) were then extracted from these isotherms by solving **eq. 4** as pressure approaches 0 atm. The diffusion coefficients (D) were then determined algebraically using the experimentally determined P and S coefficients and the equation D=P/S (**Table C1**).

Gas transport and separation in glassy polymers is generally diffusivity controlled. However, the high CO_2 permeability and selectivity of **PIM-1** are linked to their large CO_2 solubility coefficients. The increase in solubility has been ascribed to the microporous nature of **PIM-1** which increases gas uptake while also maintaining selectivity. Additionally, the nitrile groups present within the **PIM-1** backbone seemingly increase intermolecular forces between the polymer and CO_2.[7, 20] Unsurprisingly, when we incorporate **PNB** units into the **PIM-1** backbone we see a drastic decrease in CO_2 solubility coefficients (51-93%). This is presumably from the

decreased concentration of microporosity, and nitrile functionality present within the polymer matrix. This is further confirmed when we analyze the trends in solubility coefficients present in our two copolymer series. In Series 1, we note an increase in the CO_2 solubility coefficient with increasing **PIM-1** concentration (**Table S1**, entries 1-3). This seems to be primarily driven by the increase in the Langmuir coefficient. Conversely, in Series 2 there is a decrease in the CO_2 solubility coefficient and Langmuir component with increasing **PNB** concentration (**Table S1**, entries 1, 4-5) as microporosity is reduced.

The diffusivity coefficients in our two copolymer series show some interesting trends. In both Series 1 and Series 2 the CO_2 diffusivity coefficients increase. That is to say, as when we increase the concentration of **PIM-1** or **PNB**, we see an increase in the CO_2 diffusivity coefficient. While this is initially counterintuitive, when we consider that rubbery polymers transport gas through transient voids formed via segmental motion of polymer chains, whereas PIMs transport gas through "permanent" pores, we can see that it is not simply the "amount" of diffusivity we must consider, but also "what type" of diffusivity is occurring. Therefore, as we increase the concentration of **PNB**, we are increasing the flexibility of our copolymer and thus increasing the FFV created by transient voids within the polymer matrix. Conversely, as we increase the concentration of **PIM-1** we are increasing the microporosity of our polymer and this increases the FFV through increased pore volume and distribution within the polymer matrix.

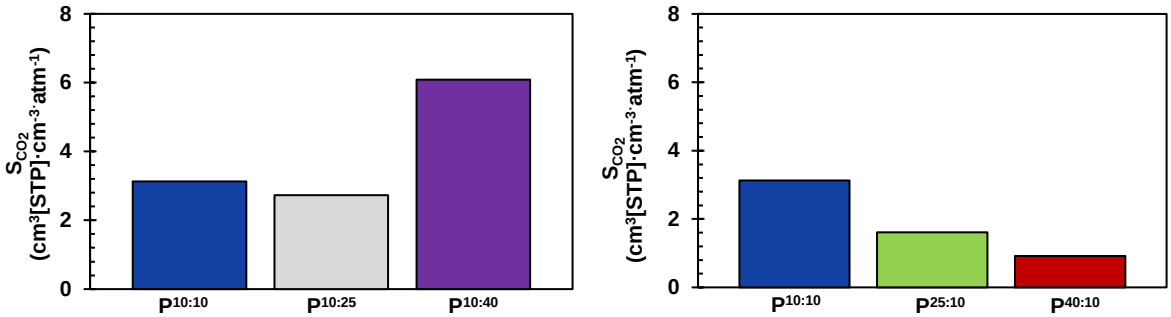

Figure 4.3. Solubility coefficients for colpolymer Series 1 (left) and copolymer Series 2 (right).

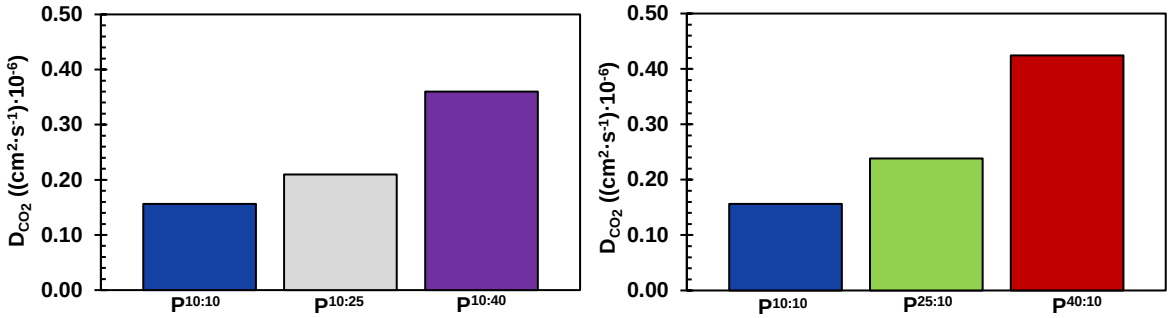

Figure 4.4. Diffusicity coefficients for colpolymer Series 1 (left) and copolymer Series 2 (right).

4.3.3 Physical Aging Studies

Physical aging is a phenomenon common to glassy polymers wherein the nonequilibrium free volume present within the polymer matrix is filled over time as segmental motion shifts the polymer chains to a state of equilibrium. This in turn gives rise to a decrease in permeability and a slight increase in selectivity. **PIM-1** notoriously undergoes physical aging more extensively and rapidly than what is seen in other glassy polymers due to the excess amount of nonequilibrium free volume present within the polymer matrix. Consequently, the impressive permeability and selectivity of **PIM-1** diminishes in a matter of weeks. As we noted earlier, the addition of **PNB** into the backbone of **PIM-1** reduces permeability and selectivity due to a decrease in the microporosity of the copolymer. The same copolymers, however, show little to no signs of physical aging over a three-month period (**Figure 4.5**). We propose two plausible explanations for this. The first relates back to the overall decrease in microporosity previously mentioned. The incorporation of rubbery units into the backbone of **PIM-1** decreases permeation via micropores and increases the permeation of gas through transient voids. Therefore, the loss in permeability due to densification of the polymer membrane is reduced because the nonequilibrium free volume within the copolymers has been reduced. The second explanation deals with the casting conditions used to prepare films. As previously noted, we experienced issues with highly volatile solvents evaporating too quickly and leading to cracked or deformed films. Therefore, we used chlorobenzene to cast films which consequently leads to slower evaporation rates (~10 days). Because **PIM-1** undergoes most of its physical aging within two weeks[9], it is highly possible that our copolymers have undergone the majority of their physical aging during the casting process. To confirm this, we cast **PIM-1** films from chlorobenzene and

tested their aging properties. Indeed, we found that **PIM-1** cast from chlorobenzene did not undergo physical aging to the extent that is commonly seen. Based on these results, we believe that the decrease in the rate and extent of physical aging noted in our copolymers is due to a combination of decreased microporosity as well as physical aging occurring during casting.

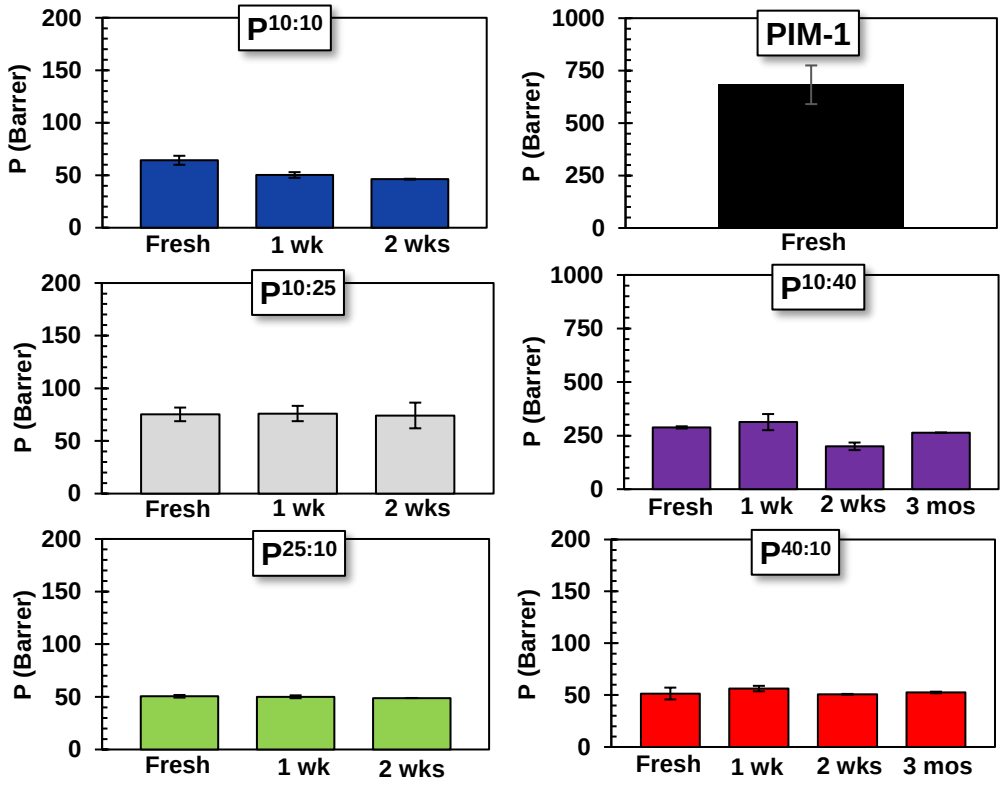

Figure 4.5. Physical aging of copolymers and **PIM-1**.

4.3.4 Mechanical Properties

The rigid and tortuous backbone present in **PIM-1** gives rise to brittle polymers. We ran tensile testing on our five copolymers as well as **PIM-1**. In Series 1, increasing the concentration of **PIM-1** increases Young's modulus and tensile strength while the elongation at break decreases (**Figure 4.6**). Conversely, in Series 2, the increased concentration of **PNB** decreases the Young's modulus and tensile strength while the elongation at break increases (**Figure 4.6**).

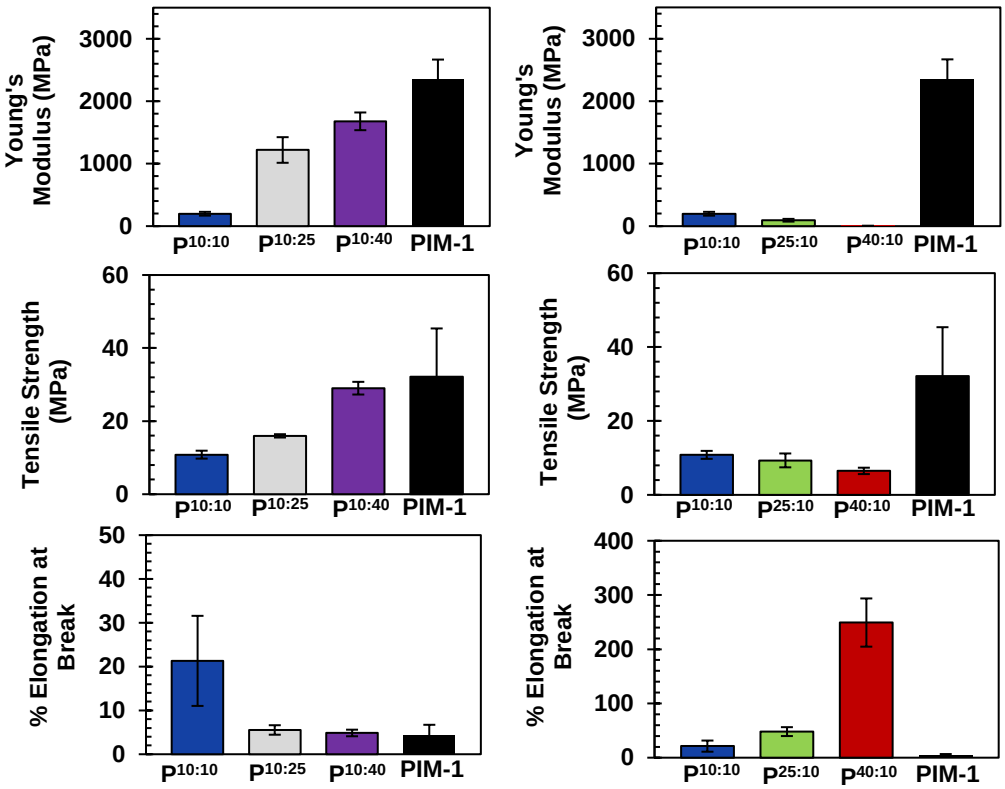

Figure 4.6. Results from mechanical testing of each copolymer series.

4.4 Conclusion

Segmented block copolymers consisting of a glassy unit and a rubbery unit were synthesized, and their gas transport, physical aging, and mechanical properties were tested and analyzed. **PIM-1** was used as the glassy unit due to its well-established synthetic procedure and step-growth polymerization method that allows for control of the molar mass and end-functionalization through stoichiometric imbalance. **NB** was polymerized via ROMP to synthesize the rubbery unit (**PNB**) for two primary reasons. One, CTAs can be utilized in ROMP to control molar mass and end-functionalize polymers using a symmetric or asymmetric olefin. Additionally, norbornene derivatives are easily tailored, and this simple modification of monomeric structure offers numerous future avenues for investigating the structure-property

relationships that govern gas transport properties. Copolymers were synthesized through nucleophilic aromatic substitution and cast from chlorobenzene into free standing films.

Analysis of gas transport data shows that the introduction of rubbery **PNB** units into the **PIM-1** backbone decreases CO_2 permeability through a reduction in microporosity and subsequent decrease in solubility. Despite the loss in CO_2 permeability, physical aging is drastically reduced upon the incorporation of **PNB**. This is presumably due to two causes. One, the overall microporosity and nonequilibrium free volume is decreased with the incorporation of flexible **PNB**. Additionally, extended casting times allow for most of the physical aging to occur during the casting period. Tensile testing showed an overall decrease in Young's modulus and tensile strength with **PNB** incorporation; however, the ductility of the polymers increased as shown from the increase in percent elongation at break.

These results display the potential for segmented block copolymer to act as tailorable gas separation membranes. Through modulation of block type and incorporation concentration, gas transport, physical aging, and mechanical properties can be tuned to meet specific requirements and needs. We envision that exchanging the nonpolar norbornene derivative used in this work with a polar norbornene derivative containing CO_2-philic moieties could increase the solubility coefficient and offer another method for tuning membrane properties.

4.5 Acknowledgements

4.6 Experimental

4.6.1 General Materials and Methods

All air-sensitive reactions were conducted under an inert atmosphere using an MBraun glovebox and a dry nitrogen atmosphere, unless noted otherwise. The monomer, 5-

hexylbicyclo[2.2.1]hept-5-ene (**M1**, endo: exo= 21:77), was gifted from Promerus LLC and purified via vacuum distillation from CaH_2, degassed using iterative freeze-pump-thaw cycles (3X), and stored in the glovebox prior to use. The starting material, 3,4-dihydroxybenzoic acid was purchased from Thermo Scientific and used as received. α,α-dichlorodiphenylmethane and 4-dimethylaminopyridine (DMAP) were purchased from TCI and used as received. *Cis*-2-butene-1,4-diol and ethyl vinyl ether were purchased from Acros Organics and used as received. 1-ethyl-3-(3-dimethylaminopropyl)carbodiimide (EDC) was purchased from AK scientific and used as received. Methanol for polymer precipitation, chlorobenzene for film casting, n-Hexanes and ethyl acetate for small molecule purification, as well as acetone, dimethylacetamide (DMAc), and N,N-dimethylformamide (DMF) for synthesis were purchased from Fischer Scientific and used as received. THF and toluene was purchased from Fisher Scientific, dried via passage through an Innovative Technologies PureSolv solvent purification system, and degassed via iterative freeze−pump−thaw cycles (3X) prior to use. Sodium bicarbonate ($NaHCO_3$), magnesium sulfate ($MgSO_4$), and potassium carbonate (K_2CO_3) were purchased from Sigma-Aldrich and used as received. Grubbs II catalyst was purchased from UMI Corp and used as received.

The starting materials 5,5',6,6'-tetrahydroxy-3,3,3',3'-tetramethyl-1,1'-spirobisindane (**TTSBI**) and tetrafluoroterephthalonitrile (**DCTB**) were purchased from Fischer Scientific and Oakwood Chemical respectively. The monomers were purified and dried according to previous literature procedure.[11]

4.6.2 Monomer and Polymer Characterization

^{1}H NMR spectra of polymers were obtained using a Bruker 500 MHz spectrometer. All ^{1}H NMR spectra were referenced to the residual $CHCl_3$ peaks at δ = 7.26 ppm or the DMSO peak at δ =2.50 ppm. All^{13}C spectra were referenced to the residual CDCl3 peak at δ = 77.00 ppm or the residual DMSO peak at δ =40.45 ppm for ^{13}C spectra. Polymer molecular weights were measured relative to polystyrene standards using an Agilent 1260 Infinity II system at 25 ºC. Polymer densities were determined via the Archimedes principle using a Mettler Toledo MS-DNY-43 density kit interfaced with a Mettler Toledo MS204S analytical balance.

4.6.3 Membrane Preparation

Membranes of all polymers discussed herein were prepared through solution casting a 3.2 wt.% polymer solution in chlorobenzene. As an example, 5 mL of chlorobenzene was added to a vial containing 0.1 g of polymer and a PTFE coated magnetic stir bar. This mixture was stirred until the polymer was fully dissolved. The resulting polymer solution was then filtered through a 0.45 µm PTFE syringe filter into a fresh, 6.5 cm diameter, cellophane-bottom dish. The dishes were covered with a Kimwipe to allow for slow evaporation of solvent. Fabricated membranes were removed from the casting dishes after slowly evaporating for 10 days.

4.6.4 Permeation Analysis

Pure gas flux was measured using a custom-built, constant-volume, variable-pressure permeation instrument. Flux measurements were used to calculate permeability coefficients according to **eq 1**.

$$P = \frac{V_d l}{P_u A R T}\left[\left(\frac{dp}{dt}\right)_{ss} - \left(\frac{dp}{dt}\right)_{leak}\right] \quad \textbf{(2)}$$

Downstream volumes (V_d) were determined through sequential Burnett expansions using He gas, as reported in the literature.[21] Membrane thicknesses (l) were directly measured using a

Mitutoyo 293-832-30 digital micrometer and typically ranged between 80 and 150 μm. Upstream pressure (P_u) was recorded as a time weighted average for the duration of steady state flux measurements. Effective membrane surface area (A) was measured using the open-source image analysis software platform ImageJ, using images generated with an Epson Perfection V19 flatbed scanner. An example of membrane surface area can be found in the Supporting Information (Figure C29). $R = 0.278 \frac{[cm \cdot Hg \cdot cm^3]}{[cm^3(STP) \cdot K]}$. Temperature (T) was recorded using an analog alcohol thermometer mounted directly outside the permeation cell.

4.6.5 Determination of Diffusivity and Solubility

According to the solution-diffusion model of gas transport in dense polymeric membranes, membrane permeability is the product of its solubility and diffusivity coefficients, as described by **eq. 3**. To determine individual solubility and diffusivity coefficients, sorption isotherms were generated for each membrane material using a custom-built dual-volume, dual-transducer pressure decay instrument. The concentration of absorbed gas was calculated as described by Koros and Paul.[22] Sorption isotherms were fit either linearly or to **eq. 4** using a custom python script utilizing a truncated Newtonian curve fitting method. Solubility coefficients were then calculated as p→ 0 using the k_d, C'_H, and b parameters determined through curve fitting. With both P and S measured directly, diffusivity coefficients D were determined algebraically using **eq. 3.**

$$\boldsymbol{P = S \cdot D} \quad \textbf{(3)}$$

$$\boldsymbol{S = \frac{C}{P} = k_d + \frac{C'_H b}{1+bp}} \quad \textbf{(4)}$$

4.6.6 Synthesis of (Z)-but-2-ene-1,4-diyl bis(3,4-dihydroxybenzoate) (CTA)

The chain transfer agent used in the polymerization of **PNB^{10}, PNB^{25}, and PNB^{40}** was synthesized through a three-step process as described here. In the first step, the starting materials, 3,4-dihydroxybenzoic acid (11.9436 g, 77.5 mmol) and α, α-dichlorodiphenylmethane (20.2161 g, 85.2 mmol), were added to a 250 mL round-bottom flask equipped with a magnetic stir bar. The reaction flask was sealed with a rubber septum and purged with N_2 gas for 20 minutes before heating to 180 $^{\circ}$C and stirring for 1 hour under light flow if N_2. After 1 h, the mixture was cooled and loaded onto silica gel. The crude product was purified through column chromatography using a 95:5 ratio of hexanes to ethyl acetate. This afforded 13.8043 g of 2,2-diphenylbenzo[*d*] [1,3] dioxole-5-carboxylic acid (**1**) as a white solid (56% isolated yield). ^{1}H NMR (DMSO): δ= 7.13 (d, 1H), 7.44 (br m, 6H), 7.49 (br s, 1H), 7.54 (m, 4H), 7.58 (d, 1H), 12.79 (br s, 1H).

The product from the first step (**1**) (4.6551 g, 14.6 mmol), *cis*-2-butene-1,4-diol (0.5989 g, 6.8 mmol), DMAP (0.4042 g, 3.3 mmol), EDCI (3.5814 g, 18.7 mmol), and DMF (110 mL) were added to a 250 mL round-bottom flask equipped with a magnetic stir bar. The flask was sealed with a septum and the reaction mixture was allowed to stir for 15 hours at room temperature under a light flow of N_2. The reaction mixture was diluted with water then extracted with ethyl acetate, washed with brine and dried over $MgSO_4$. The resulting mixture was concentrated and loaded onto silica gel. The crude product was purified through column chromatography using a 90:10 ratio of hexanes and ethyl acetate as the eluent to afford 2.9936 g of (*Z*)-but-2-ene-1,4-diyl bis(2,2-diphenylbenzo[*d*] [1,3] dioxole-5-carboxylate) (**2**) as a white solid (64 % isolated yield). ^{1}H NMR ($CDCl_3$): δ= 4.92 (d, 4H), 5.89 (t, 2 H), 6.88 (d, 2H), 7.37 (m, 12H), 7.55 (m, 9 H), 7.66 (dd, 2H)

In the final step, the isolated product (**2**) (5.0743 g, 7.4 mmol), acetic acid (266 mL), and water (66 mL) were added to a 500 mL round-bottom flask. The reaction flask was then equipped with a condenser and refluxed at 120 ^{o}C for 6 hours. The resulting mixture was diluted with water until a white precipitate formed then extracted with ethyl acetate. This was neutralized with a saturated solution of $NaHCO_3$ then washed with brine and dried over $MgSO_4$. The solution was concentrated *in-vacuo* and afforded 0.78 g of (Z)-but-2-ene-1,4-diyl bis(3,4-dihydroxybenzoate) (**CTA**) as a white powder (76% isolated yield). ^{1}H NMR (DMSO)= 4.88 (d, 4H), 5.85 (3, 2H), 6.81 (d, 2H), 7.32 (dd, 2H), 7.37 (d, 2H), 9.36 (s, 2H), 9.83 (s, 2H).

4.6.7 General NB Polymerization

In a typical polymerization procedure **NB** was added to a vial equipped with a magnetic stir bar in a glove box. Solutions of both **GII** and **CTA-1** were prepared in THF. A portion of the **GII** solution and the **CTA-1** solution were mixed at volumes such that the desired ratio of **GII**:**CTA-1** was achieved and stirred at room temperature for 10 minutes. Following, a specific volume of the catalyst and CTA mixture were added to the monomer such that the desired monomer:cat:CTA ratio was achieved. The final reaction mixture was allowed to stir for 15 hours at room temperature. The polymerization was quenched with ethyl vinyl ether and diluted with THF before precipitating in stirring methanol. The resulting polymer was isolated via vacuum filtration and dried under vacuum. ^{1}H NMR ($CDCl_3$) polymer repeat units = 0.88 (br m, 2H), 0.88-0.98 (br m, 6H), 1.92 (br m, 1H), 2.27-2.99 (br m, 1H), 5.20 (br m, 2H); **CTA-1** end caps 6.87 (br d, 2H), 7.55 (br, m, 4H). Note that the integration representative of the protons within the polymer repeat units and the protons of the CTA end caps will change relative to one

another as polymer molar mass is changed. Therefore, the integrations recorded above for the CTA are not integrated with respect to the polymer repeat units.

4.6.8 General PIM-1 Polymerization

All samples of PIM-1 were synthesized following modified literature procedures.[11] To successfully end cap **PIM-1** with **DCTB** and control the molar mass of the final polymers, stoichiometric excess of **DCTB** was added to the reaction flask. The exact amount of excess **DCTB** was determined using the modified Carothers equation (eq. X) and the desired theoretical molar mass.

$$\bar{X}_n = \frac{1+r}{1+r-2rp} \quad \textbf{(5)}$$

4.6.9 General Copolymer Synthesis

In a typical polymerization of **PIM-1** (15.1 kg/mol) with P**NB** (9.4 kg/mol), **PIM$_{10}$** (3.0060 g, 0.20 mol), **NB$_{10}$** (1.8774 g, 0.20 mmol), and K_2CO_3 (98.5 mg, 0.71 mmol) were weighed into a 100 mL 3-neck round bottom equipped with a magnetic stir bar. The reaction flask was sealed and purged with N_2 for 20 min. The polymers were then dissolved in dry DMAc (20 mL) and dry toluene (10 mL). The reaction flask was placed in an oil bath set to 165 ºC and stirred under a light flow of N_2 for 1 hour. After an hour, the reaction flask was cooled to room temperature, the viscous solution was diluted with 50 mL of toluene, precipitated into stirring MeOH, and filtered via vacuum filtration. The yellow solid was then placed in a cellulose thimble and washed with water overnight via Soxhlet extraction. The polymer was redissolved in 100 mL of THF and precipitated a second time in stirring MeOH. The precipitate was filtered and dried under vacuum at 65 ºC overnight to yield 4.3157 g of the polymeric product (88 %).

4.6.10 Thermal Analysis

Thermogravimetric analysis (TGA) was performed using a TA Instruments Q-50 TGA with a heating rate of 10 ºC/min under an N_2 purge. All T_d values are reported as the temperature corresponding to 5% weight loss.

Differential Scanning Calorimetry (DSC) was performed on a TA Instruments Q-2000 DSC. All samples were run at a ramp rate of 10 ºC/min in the range of -70-200 ºC.

4.6.11 Mechanical Testing

Films for tensile testing were cast using a 20 mil BYK Doctor Blade and cut into a dog bone shape with an ASTM D638 type V dye. All tensile testing was performed on a Instron 5965 Universal Testing System with 5 kN pneumatic side action tensile grips at a quasistatic speed of 10 mm/min at an ambient temperature of 20 ºC. Samples exhibiting any structural damage, notches, or slipping in clamps were excluded from the results. To control variability, 10 samples were run for each polymer.

References

(1) Park, H. B.; Kamcev, J.; Robeson, L. M.; Elimelech, M.; Freeman, B. D. Maximizing the right stuff: The trade-off between membrane permeability and selectivity. *Science* **2017**, *356* (6343). DOI: 10.1126/science.aab0530.
(2) Galizia, M.; Chi, W. S.; Smith, Z. P.; Merkel, T. C.; Baker, R. W.; Freeman, B. D. 50th Anniversary Perspective: Polymers and Mixed Matrix Membranes for Gas and Vapor Separation: A Review and Prospective Opportunities. *Macromolecules* **2017**, *50* (20), 7809-7843. DOI: 10.1021/acs.macromol.7b01718.
(3) Robeson, L. M. Correlation of Separation Factor Versus Permeability for Polymeric Membranes. *Journal of Membrane Science* **1991**, *62* (2), 165-185. DOI: 10.1016/0376-7388(91)80060-j.
(4) Freeman, B. D. Basis of Permeability/Selectivity Tradeoff Relations in Polymeric Gas Separation Membranes. *Macromolecules* **1999**, *32* (2), 375-380. DOI: 10.1021/ma9814548.
(5) Budd, P. M.; Elabas, E. S.; Ghanem, B. S.; Makhseed, S.; McKeown, N. B.; Msayib, K. J.; Tattershall, C. E.; Wang, D. Solution-Processed, Organophilic Membrane Derived from a Polymer of Intrinsic Microporosity. *Advanced Materials* **2004**, *16* (5), 456-459. DOI: 10.1002/adma.200306053.
(6) Budd, P. M.; Ghanem, B. S.; Makhseed, S.; McKeown, N. B.; Msayib, K. J.; Tattershall, C. E. Polymers of intrinsic microporosity (PIMs): robust, solution-processable, organic nanoporous materials. *Chemical Communications* **2004**, (2), 230. DOI: 10.1039/b311764b.
(7) Budd, P.; Msayib, K.; Tattershall, C.; Ghanem, B.; Reynolds, K.; McKeown, N.; Fritsch, D. Gas Separation Membranes from Polymers of Intrinsic Microporosity. *Journal of Membrane Science* **2005**, *251* (1-2), 263-269. DOI: 10.1016/j.memsci.2005.01.009.
(8) McKeown, N. B. The synthesis of polymers of intrinsic microporosity (PIMs). *Science China Chemistry* **2017**, *60* (8), 1023-1032. DOI: 10.1007/s11426-017-9058-x.
(9) Swaidan, R.; Ghanem, B.; Litwiller, E.; Pinnau, I. Physical Aging, Plasticization and Their Effects on Gas Permeation in "Rigid" Polymers of Intrinsic Microporosity. *Macromolecules* **2015**, *48* (18), 6553-6561. DOI: 10.1021/acs.macromol.5b01581.
(10) Polak-Kraśna, K.; Dawson, R.; Holyfield, L. T.; Bowen, C. R.; Burrows, A. D.; Mays, T. J. Mechanical characterisation of polymer of intrinsic microporosity PIM-1 for hydrogen storage applications. *Journal of Materials Science* **2017**, *52* (7), 3862-3875. DOI: 10.1007/s10853-016-0647-4.
(11) Song, J.; Du, N.; Dai, Y.; Robertson, G. P.; Guiver, M. D.; Thomas, S.; Pinnau, I. Linear High Molecular Weight Ladder Polymers by Optimized Polycondensation of Tetrahydroxytetramethylspirobisindane and 1,4-Dicyanotetrafluorobenzene. *Macromolecules* **2008**, *41* (20), 7411-7417. DOI: 10.1021/ma801000u.
(12) Du, N.; Robertson, G. P.; Pinnau, I.; Guiver, M. D. Polymers of Intrinsic Microporosity with Dinaphthyl and Thianthrene Segments. *Macromolecules* **2010**, *43* (20), 8580-8587. DOI: 10.1021/ma101930x.
(13) Sekizkardesa;, A. K.; Budhathokia;, S.; Zhua;, L.; Kusumaa;, V.; Tonga;, Z.; McNally;, J. S.; Steckela;, J. A.; Yia;, S.; Hopkinsona;, D. Molecular design and fabrication of PIM-1/polyphosphazene blend membranes with high performance for CO2/N2 separation. *J. Membr. Sci* **2021**, *640*, 119764. DOI: https://doi.org/10.1016/j.memsci.2021.119764

(14) Yong, W. F.; F.Y.Li; Xiao, Y. C.; Li, P.; Pramoda, K. P.; Tong, Y. W.; Chung, T. S. Molecular engineering of PIM-1/Matrimid blend membranes for gas separation. *J Membr. Sci.* **2012**, *407-408*, 47-57. DOI: doi:10.1016/j.memsci.2012.03.038.
(15) Wang, L.; Guo, X.; Zhang, F.; Li, N. Blending and in situ thermally crosslinking of dual rigid polymers for anti-plasticized gas separation membranes *J. Membr. Sci* **2021**, *638*, 1119668.
(16) Bengtson;, G.; Neumann;, S.; Filiz, V. Membranes of Polymers of Intrinsic Microporosity (PIM-1) Modified by Poly(ethylene glycol). *Membranes* **2017**, *7* (2), 28. DOI: 10.3390/membranes7020028.
(17) Stevens, M. P. *Polymer Chemistry: An Introduction*; Oxford University Press, 1999.
(18) Bielawski, C. W.; Benitez, D.; Morita, T.; Grubbs, R. H. Synthesis of End-Functionalized Poly(norbornene)s via Ring-Opening Metathesis Polymerization. *Macromolecules* **2001**, *34* (25), 8610-8618. DOI: 10.1021/ma010878q.
(19) Vanbiervliet, E.; Fouquay, S.; Michaud, G.; Simon, F.; Carpentier, J.-F.; Guillaume, S. M. From Epoxide to Cyclodithiocarbonate Telechelic Polycyclooctene through Chain-Transfer Ring-Opening Metathesis Polymerization (ROMP): Precursors to Non-Isocyanate Polyurethanes (NIPUs). *Macromolecules* **2017**, *50* (1), 69-82. DOI: 10.1021/acs.macromol.6b02137.
(20) Li, P.; Chung, T. S.; Paul, D. R. Gas sorption and permeation in PIM-1. *Journal of Membrane Science* **2013**, *432*, 50-57. DOI: 10.1016/j.memsci.2013.01.009.
(21) Czichos, H. S., T.; Smith, L. *Springer Handbook of Materials Measurement Methods*; 2006.
(22) Koros, W. J. P., D. R. Design considerations for measurement of gas sorption in polymers by pressure decay. *J. Polym. Sci. Phys. Ed.* **1976**, *14* (10), 1903-1907. DOI: 10.1007/978-3-540-30300-8.

CHAPTER V: CONCLUSIONS AND OUTLOOK

This work is centered around deepening the understanding of polynorbornene synthesis and application as dense polymeric gas separation membranes. Norbornenes can be polymerized through a variety of methods, notably vinyl addition polymerization (VAP) and ring opening metathesis polymerization. While VAP is commonly employed to polymerize polynorbornenes with robust thermomechanical properties, the catalysts typically employed for these polymerizations are often sensitive to functional groups. ROMP, while it gives rise to less thermally and chemically stable polymers, is considerably more functional group tolerant and allows in situ end group functionalization through the incorporation of chain transfer agents (CTAs).

Chapter II focuses on our efforts to better understand the coordination environment between single-site neutral Ni-based catalysts and polar-functionalized norbornenes in VAP. Preliminary results from our lab show that polar functionalized norbornene monomers give rise to low molar mass polymers in low yields compared to nonpolar functionalized norbornenes monomers. We hypothesized that the differences in polymerization results were due to coordination/chelation of the polar moiety to the metal center. We investigated this possibility by looking at the coordination environment of our catalyst with polar monomers and ethyl acetate using IR and ^{19}F NMR spectroscopy. These results suggest coordination of two molecules of our monomer or the ethyl acetate molecule via the carbonyl group in *cis* fashion to the Ni center. Additional single-site, neutral Ni catalysts were synthesized and used to polymerize both polar and nonpolar monomers. The ligand strength of these catalyst was also determined, and it was

revealed that the polymerization of the nonpolar norbornene monomers is strongly dependent on ligand strength; however, this is not the case for nonpolar norbornene monomers.

Chapter II reports on the role monomer stereochemistry plays in gas transport through dense polymeric membranes. We found that when the *exo*-isomer of a series of four alkoxysilylnorbornene monomers was separated and subsequently polymerized using VAP, the permeability of CO_2 in the exo-enriched polymers is slightly decreased with no change observed for selectivity (CO_2/N_2). Further investigations reveal that the diffusivity of the *exo*-enriched polymers is slightly decreased compared to the mixed polymer counterparts. This was hypothesized to arise from the stereoregularity of the polymer chain preventing segmental motion and suppressing transient movement of gas through the membranes. Conversely, the solubility coefficient is increased in the *exo*-enriched polymers. This is accompanied by an increase in FFV that is presumably due to the stereoregularity of the polymer chains preventing packing. The increase in FFV is slight, and analysis via WAXS does not reveal any notable differences in chain packing between the two series. Therefore, it is a loss in diffusivity that leads to an overall decrease in permeability for the *exo*-enriched polymers.

Chapter III continues to investigate the structure-property relationship that gpversn gas transport properties. Segmented block copolymers are synthesized using PIM-1 and polynorbornene synthesized via ROMP. Two series of copolymers are developed to systematically investigate (series 1) the effects of incorporating rubbery polymer units into the backbone of microporous polymers and (series 2) the effects of incorporating microporous polymer units into the backbone of rubbery polymers on gas transport properties, physical aging, and mechanical properties. Our research reveals that when polynorbornene units are incorporated

into the backbone of PIM-1, there is a decrease in CO_2 permeability that arises due to a decrease in solubility. Despite the loss in permeability, physical aging is reduced, and the mechanical properties of the copolymers are modulated according to incorporation ratio of each polymer.

APPENDICES

Appendix A: Supporting Information for Chapter II

A.1 NMR spectra of M3

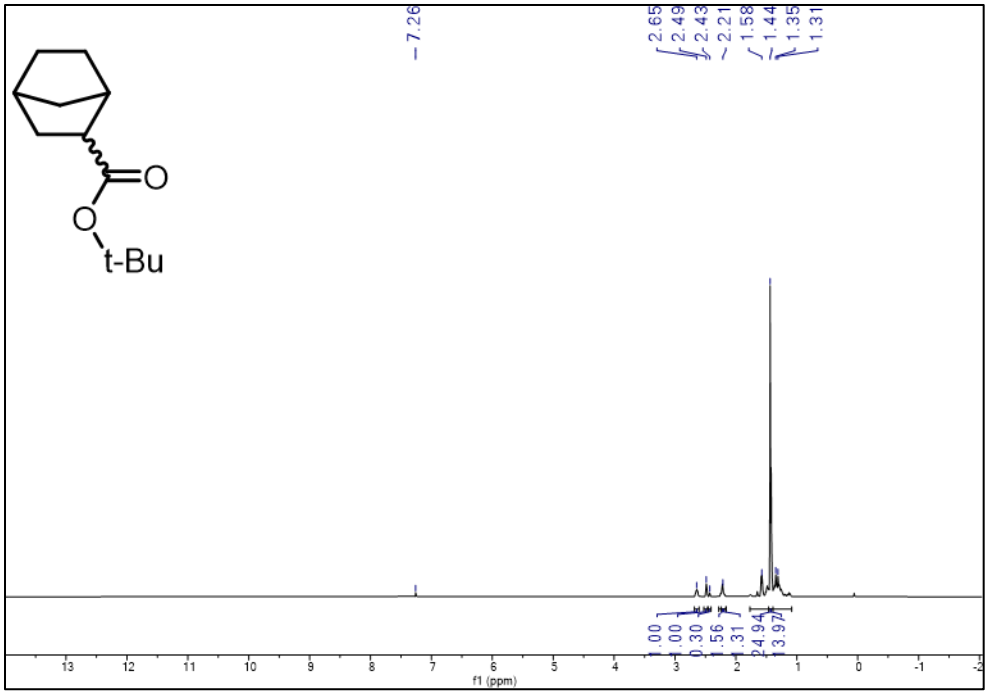

Figure A1. ^{1}H NMR spectrum of **M3** in $CDCl_3$.

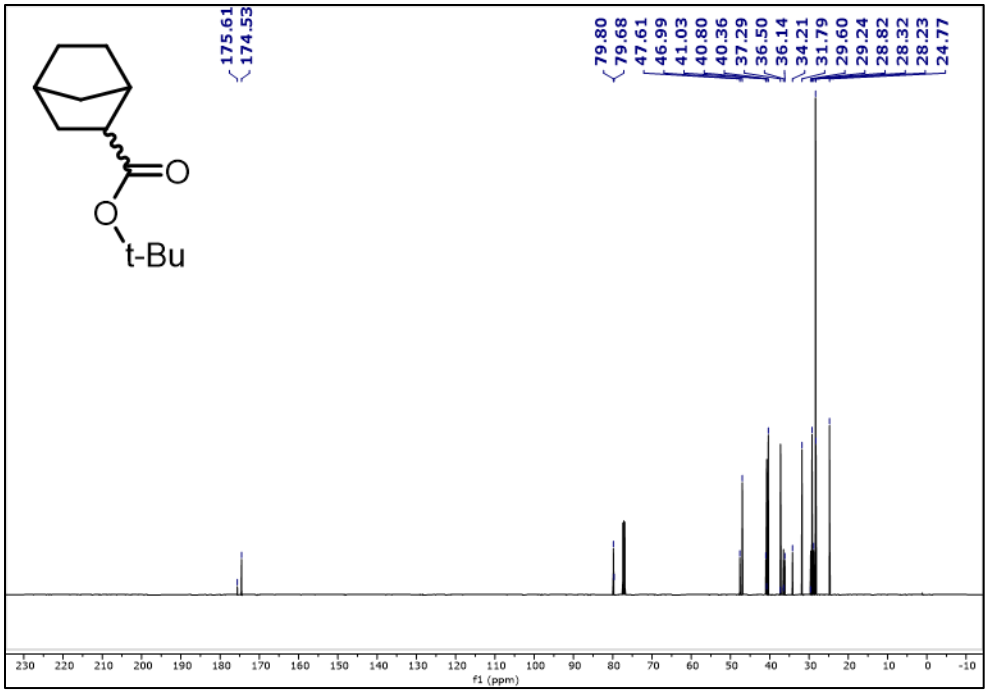

Figure A2. ^{13}C NMR spectrum of **M3** in $CDCl_3$

A.2 NMR spectra of Neutral Nickel Catalysts

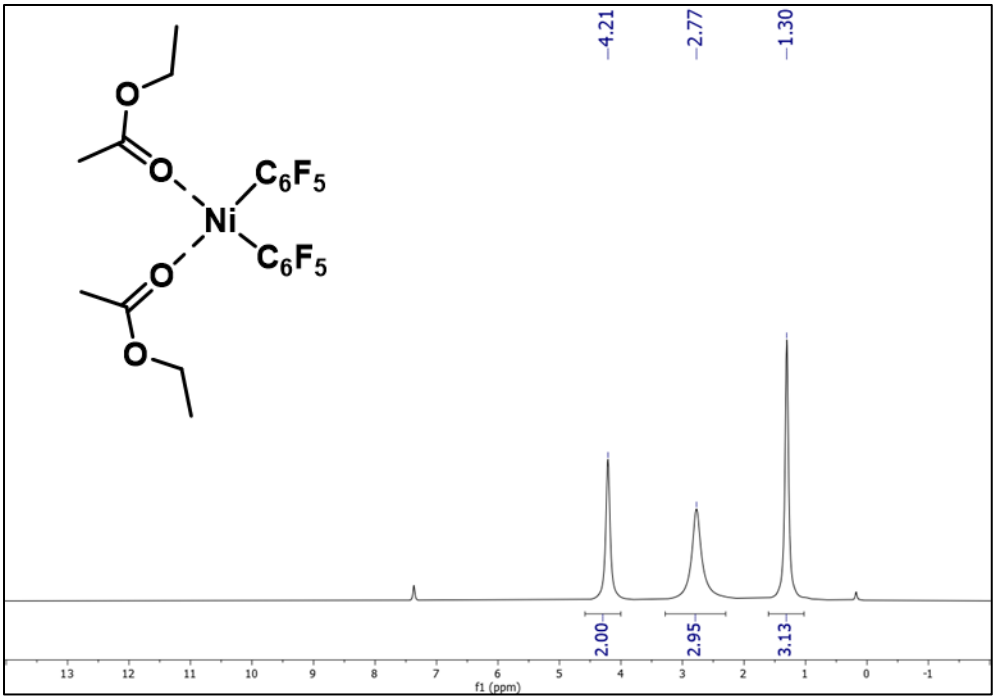

Figure A3. ^{1}H NMR spectrum of **Ni3** in $CDCl_3$.

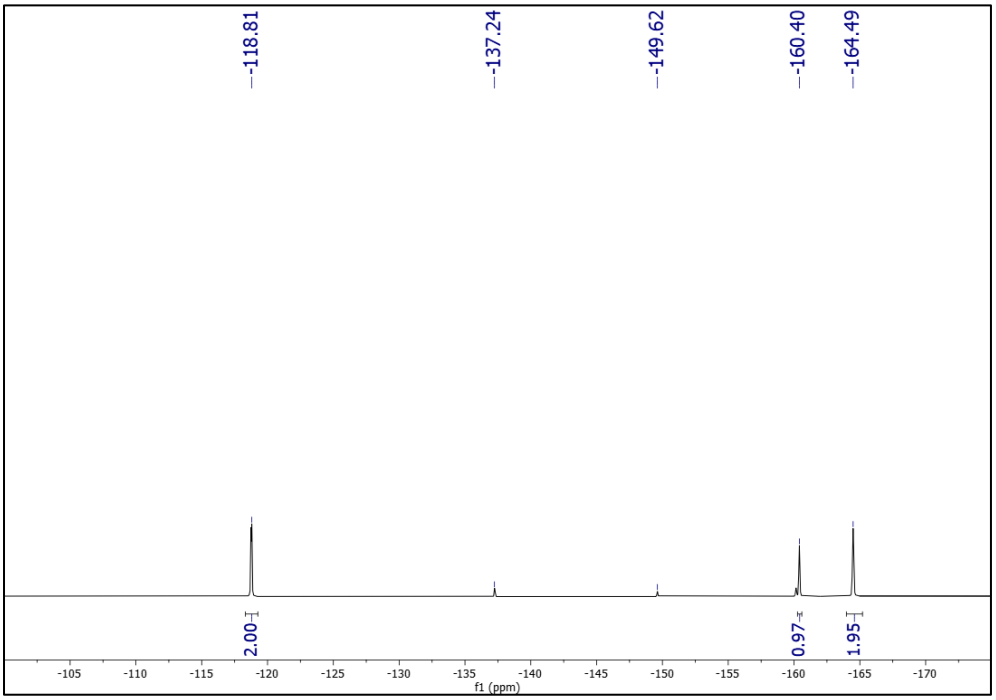

Figure A4. ^{19}F spectrum of **Ni3** in $CDCl_3$.

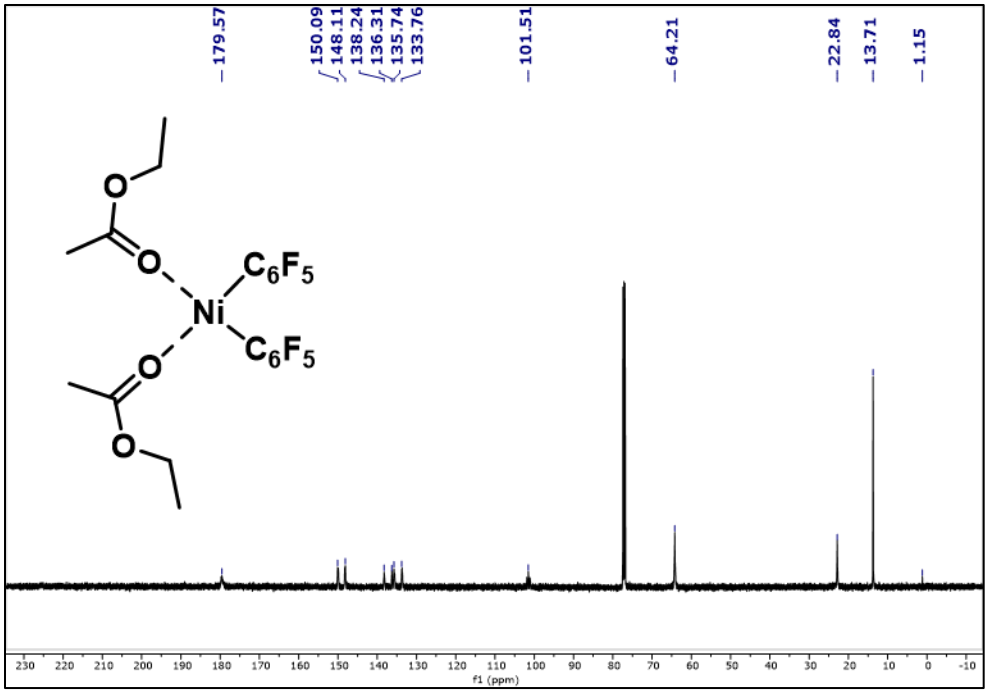

Figure A5. ^{13}C spectrum of **Ni3** in $CDCl_3$.

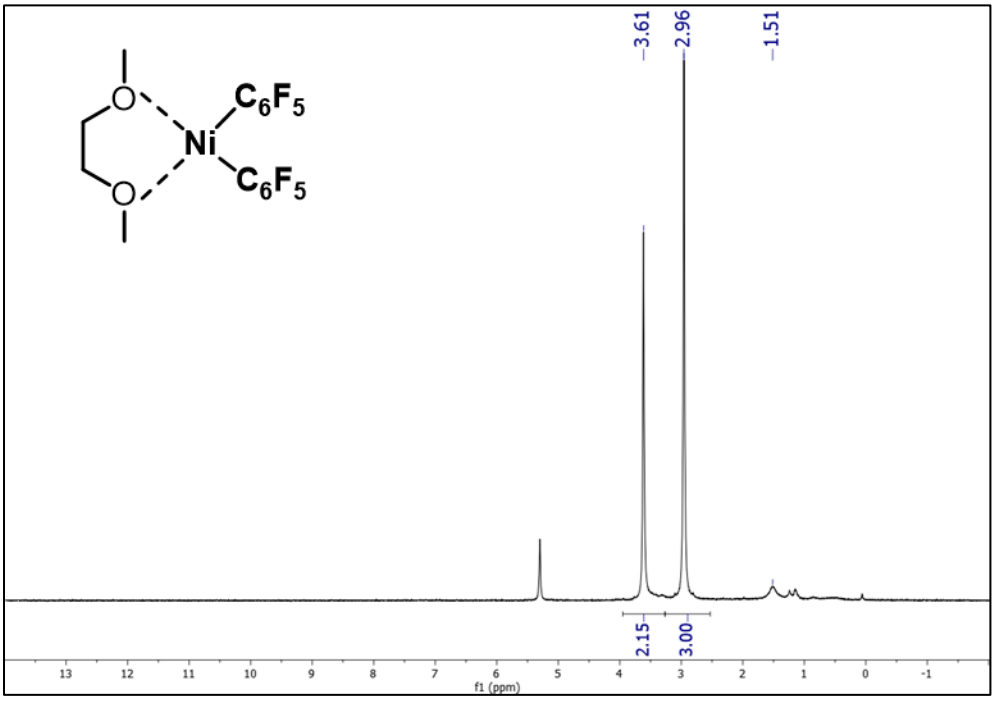

Figure A6. ^{1}H NMR spectrum of **Ni5** in CD_2Cl_2.

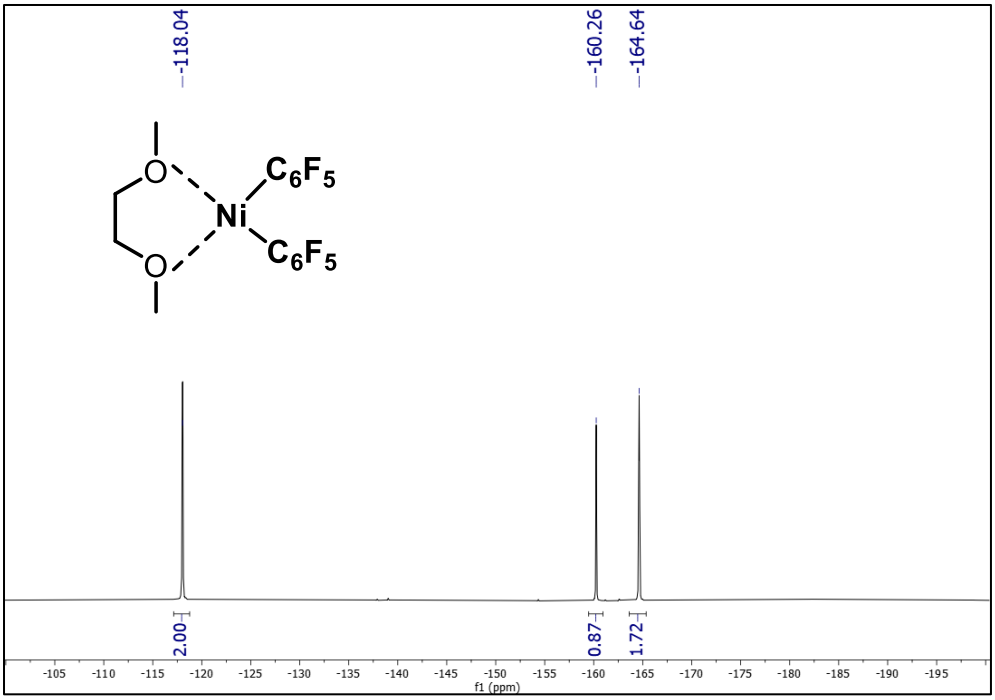

Figure A7. ^{19}F NMR spectrum of **Ni5** in CD_2Cl_2.

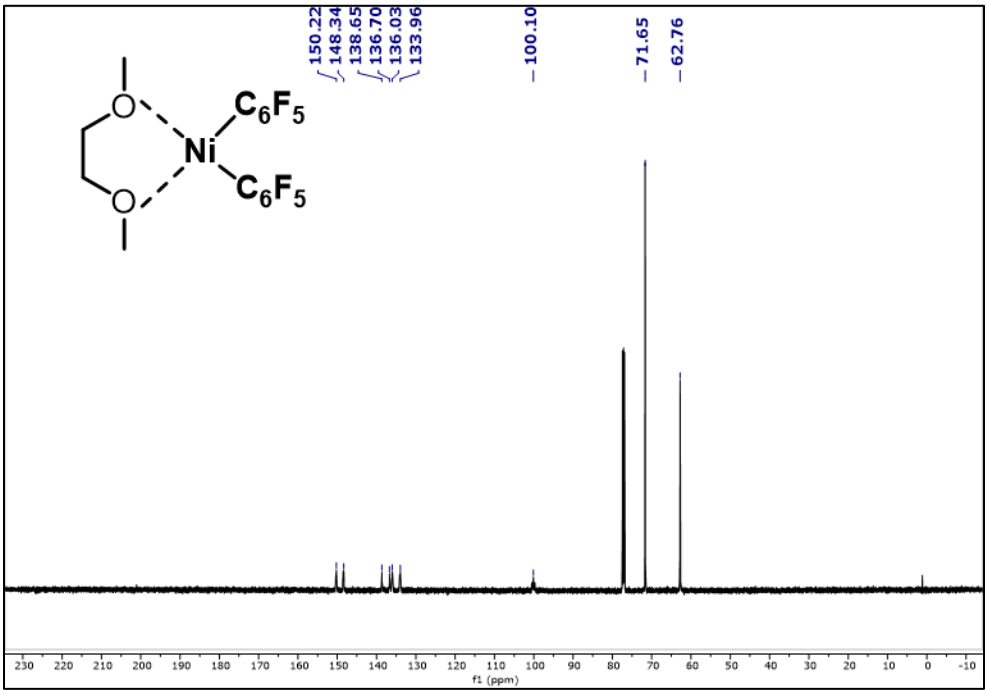

Figure A8. ^{13}C NMR spectrum of **Ni5** in $CDCl_3$.

A.3 Monitoring Equilibria via ^{19}F NMR Spectroscopy

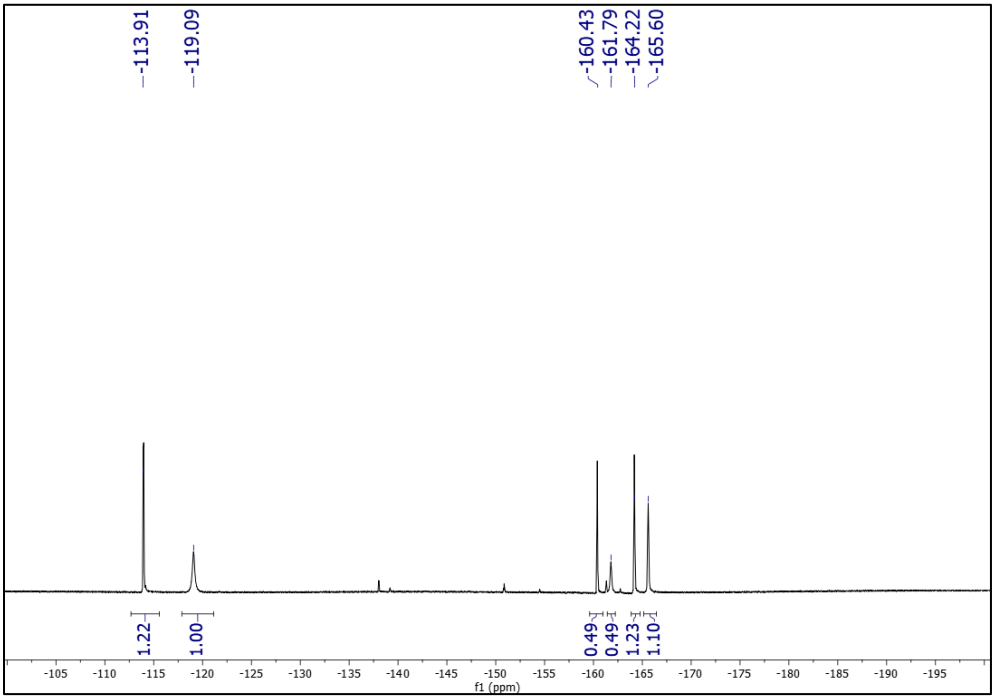

Figure A9. ^{19}F NMR spectrum of equilibrium between **Ni1** and EtOAc in CD_2Cl_2.

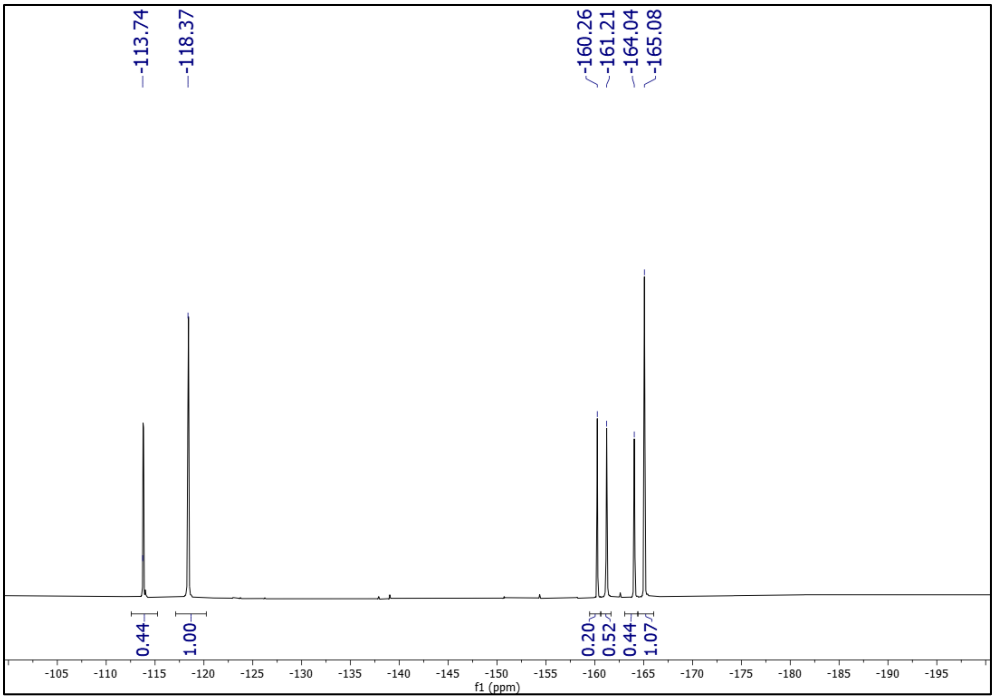

Figure A10. ^{19}F NMR spectrum of equilibrium between **Ni1** and THF in CD_2Cl_2.

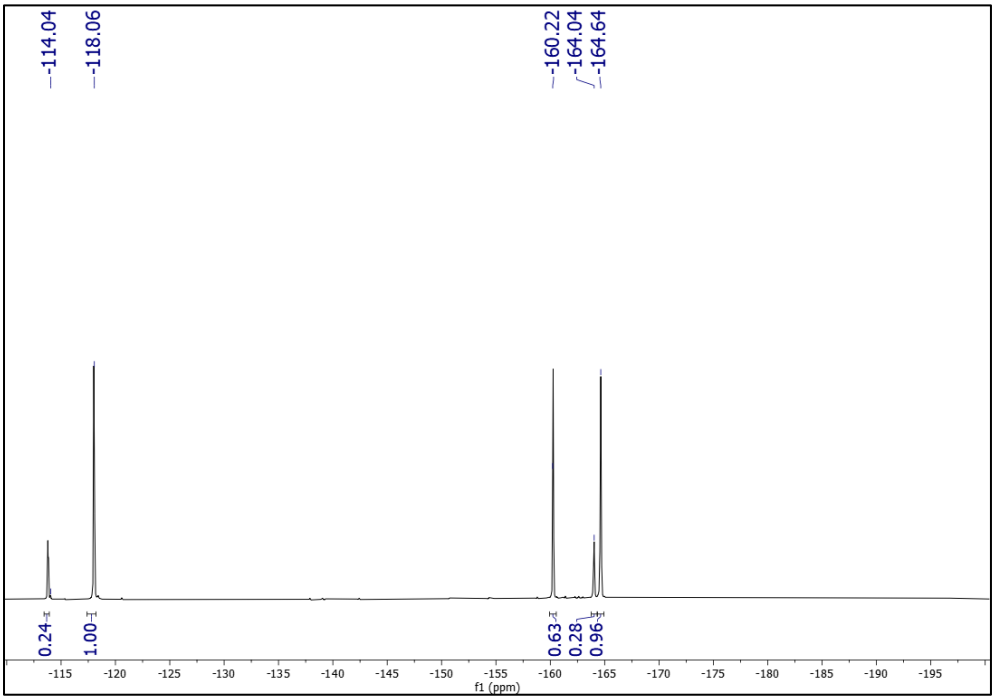

Figure A11. ^{19}F NMR spectrum of equilibrium between **Ni1** and DME in CD_2Cl_2.

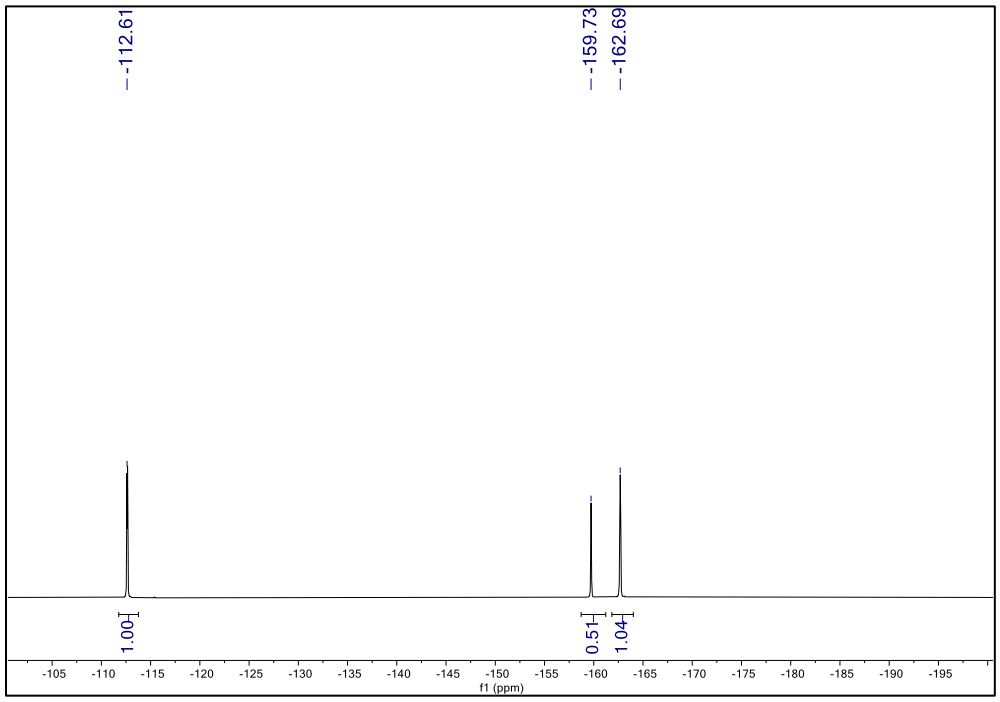

Figure A12. ^{19}F NMR spectrum of equilibrium between Ni2 and M3 in CD_2Cl_2.

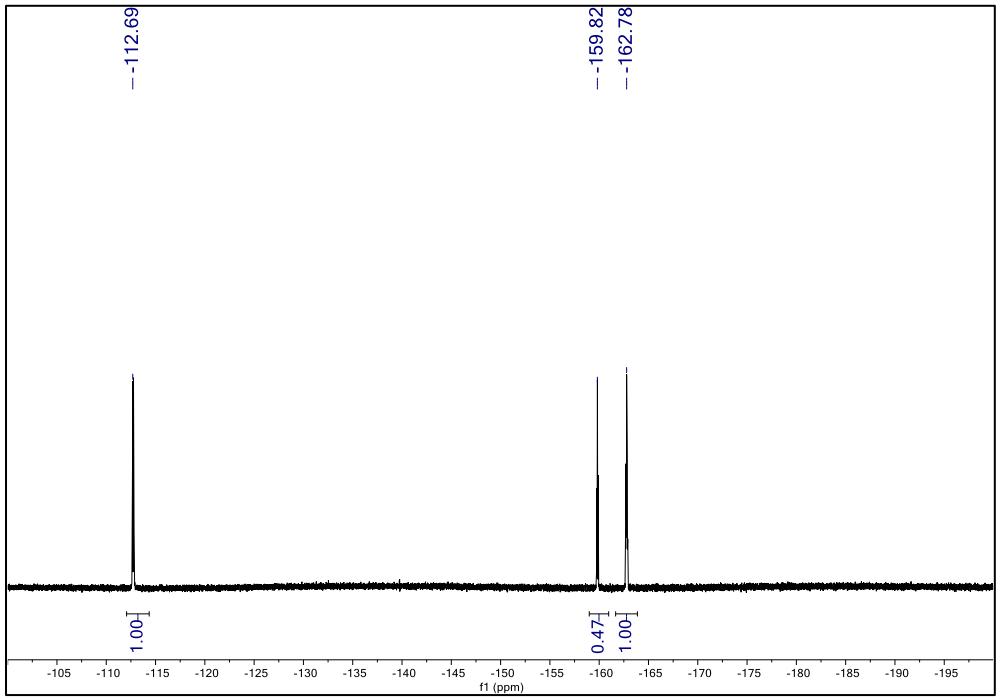

Figure A13. ^{19}F NMR spectrum of equilibrium between **Ni2** and EtOAc in CD_2Cl_2.

A.4 IR Spectra

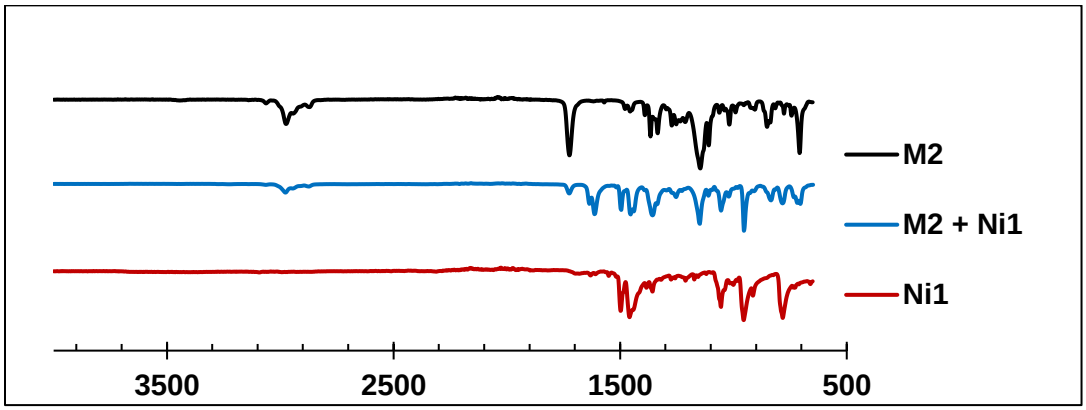

Figure A14. IR spectra of **M2** (top), **Ni1** (bottom), and **M2** + **Ni1**(middle) .

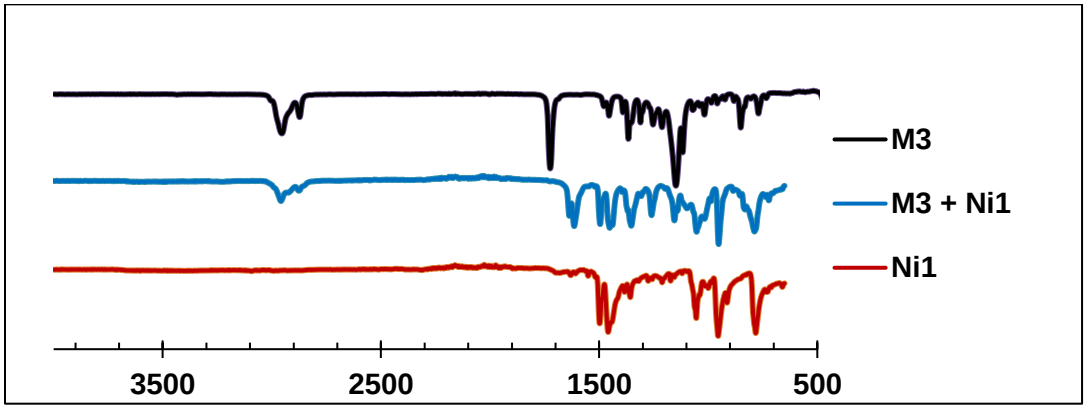

Figure A15. IR spectra of **M3** (top), **Ni1** (bottom), and **M3** + **Ni1** (middle) .

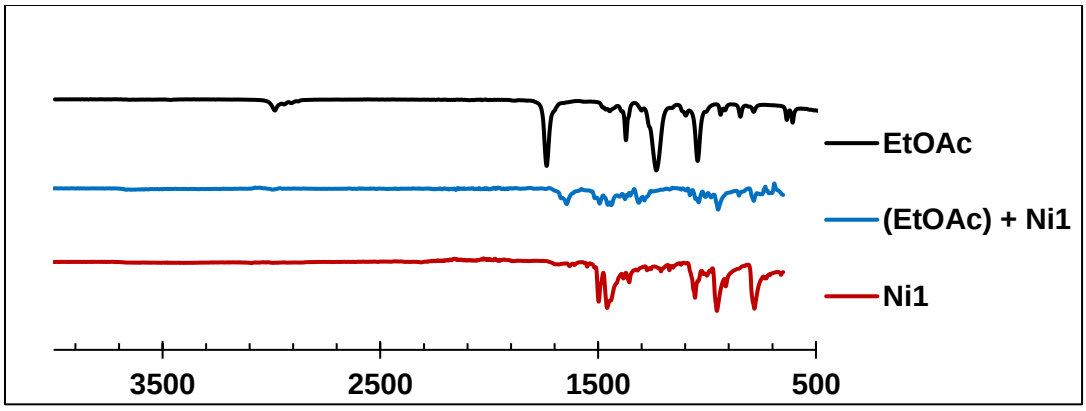

Figure A16. IR spectra of EtOAc (top), **Ni1** (bottom), and EtOAc + **Ni1** (middle).

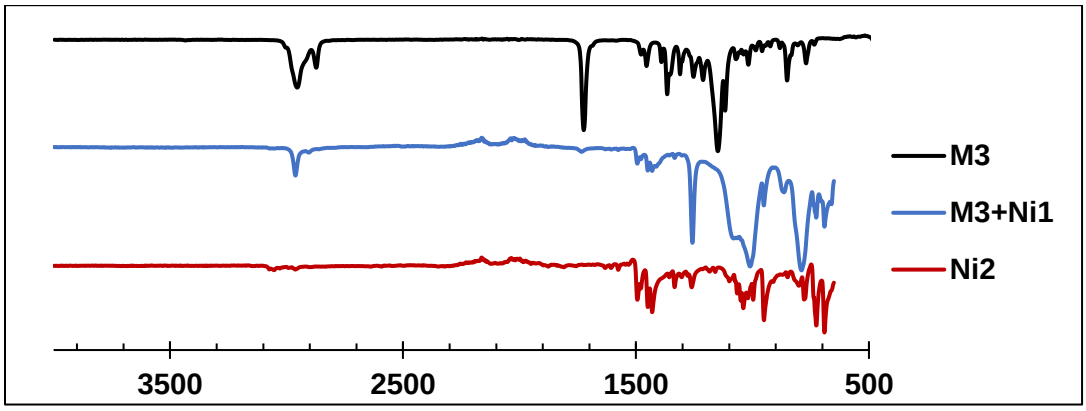

Figure A17. IR spectra of **M3** (top), **Ni2** (bottom), and **M3** + **Ni2** (middle).

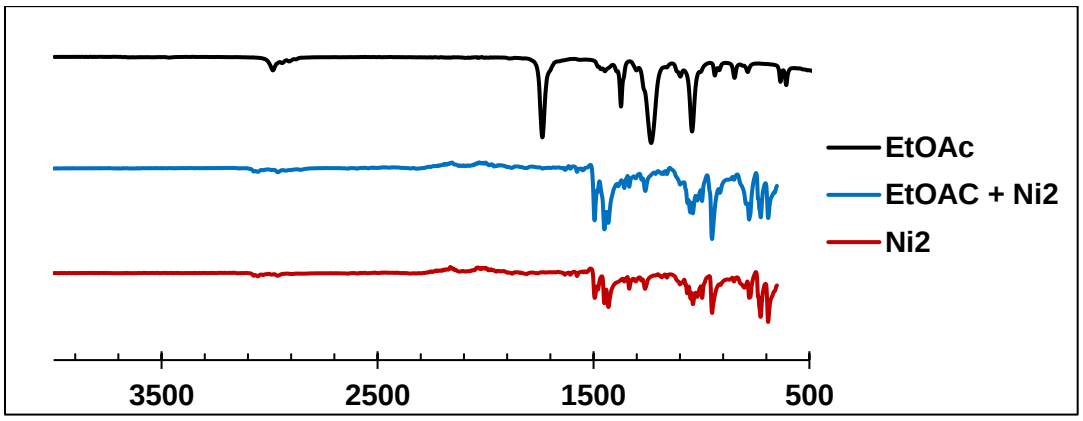

Figure A18. IR spectra of EtOAc (top), **Ni2** (bottom), and EtOAc + **Ni2** (middle).

A.5 GPC Traces

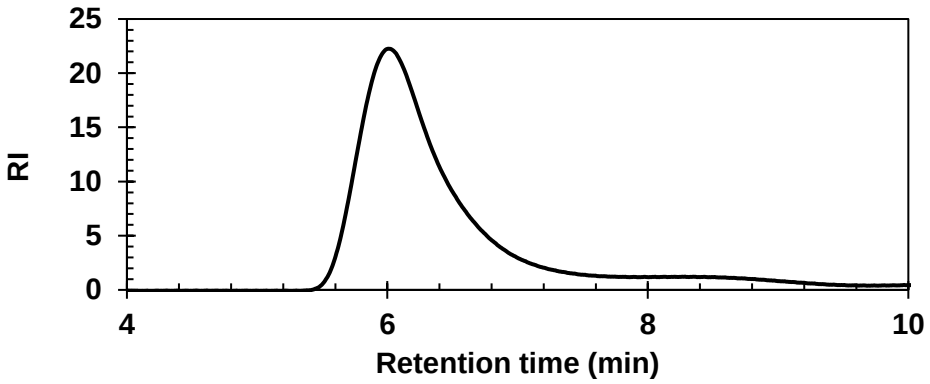

Figure A19. GPC trace of **M1** polymerized with **Ni1**.

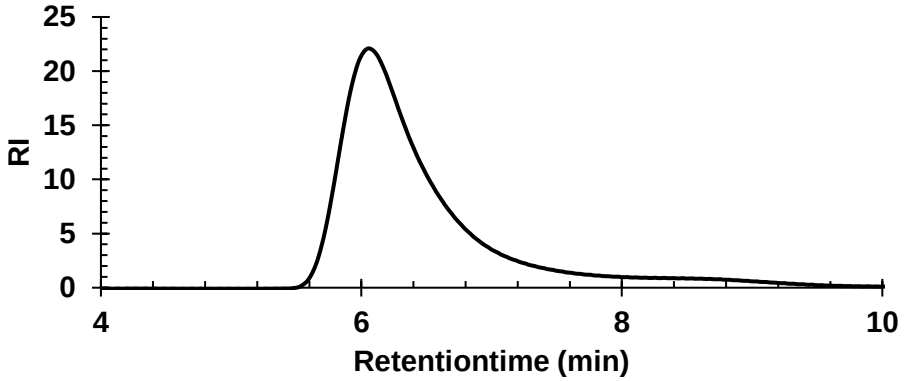

Figure A20. GPC trace of **M1** polymerized with **Ni2**.

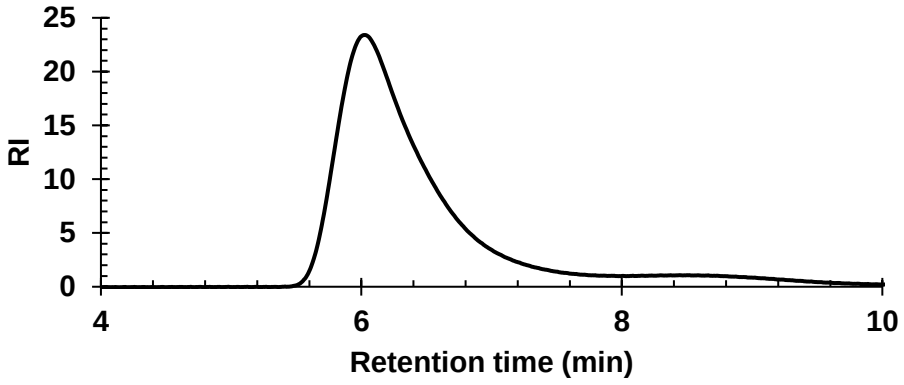

Figure A21. GPC trace of **M1** polymerized with **Ni3**.

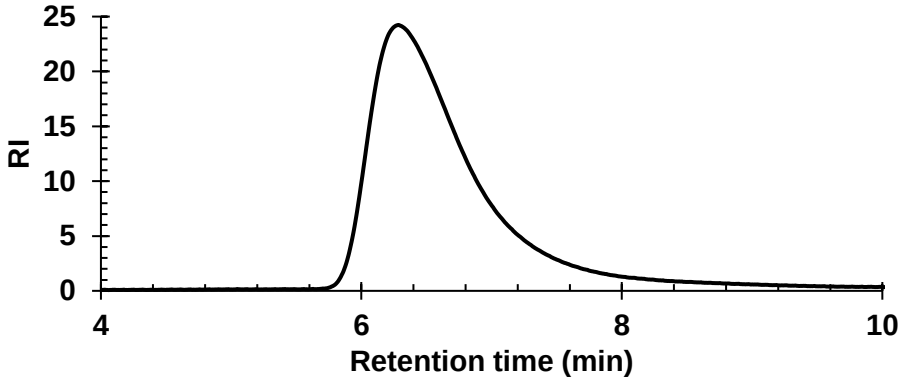

Figure A22. GPC trace of **M1** polymerized with **Ni4**.

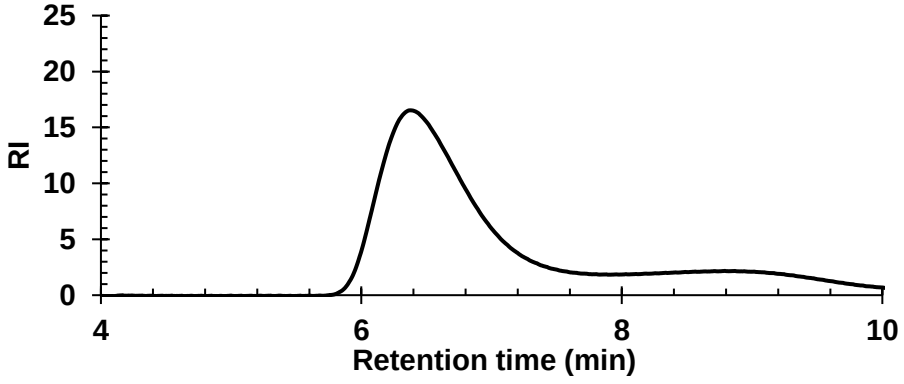

Figure A23. GPC trace of **M1** polymerized with **Ni5**.

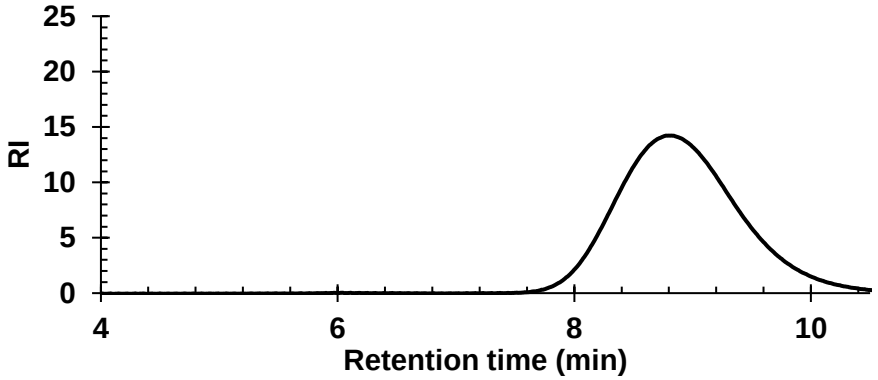

Figure A24. GPC trace of **M2** polymerized with **Ni1**.

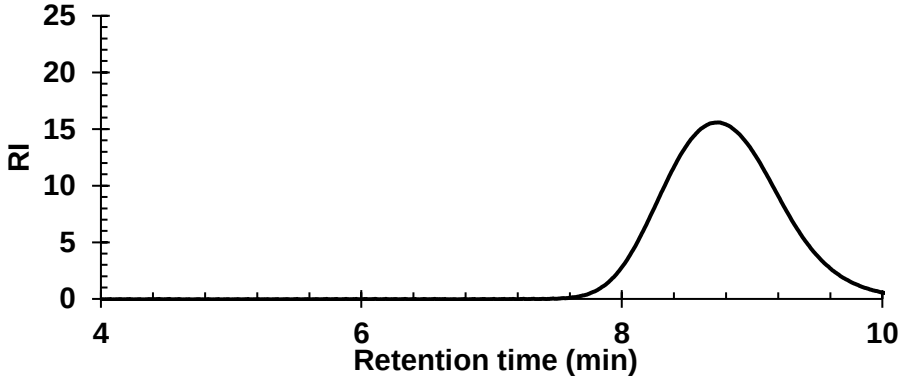

Figure A25. GPC trace of **M2** polymerized with **Ni2**.

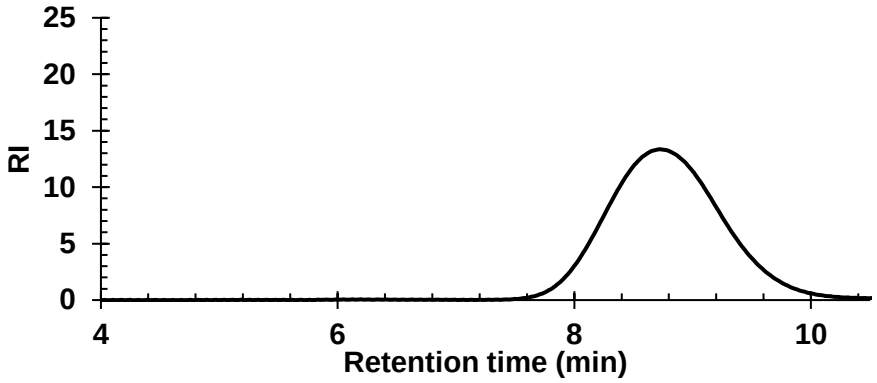

Figure A26. GPC trace of **M2** polymerized with **Ni3**.

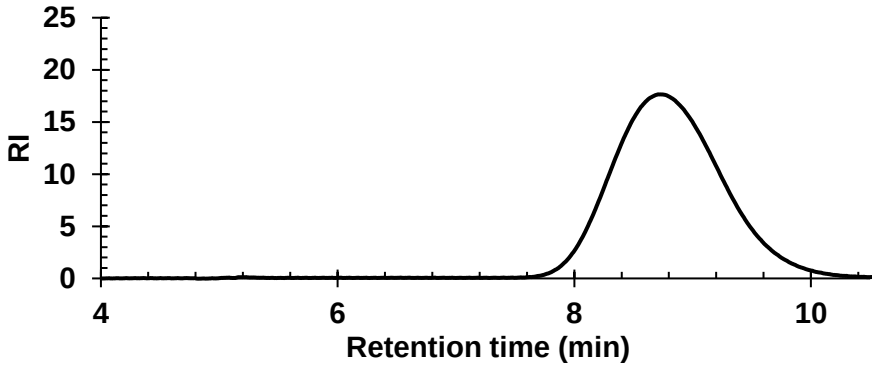

Figure A27. GPC trace of **M2** polymerized with **Ni4**.

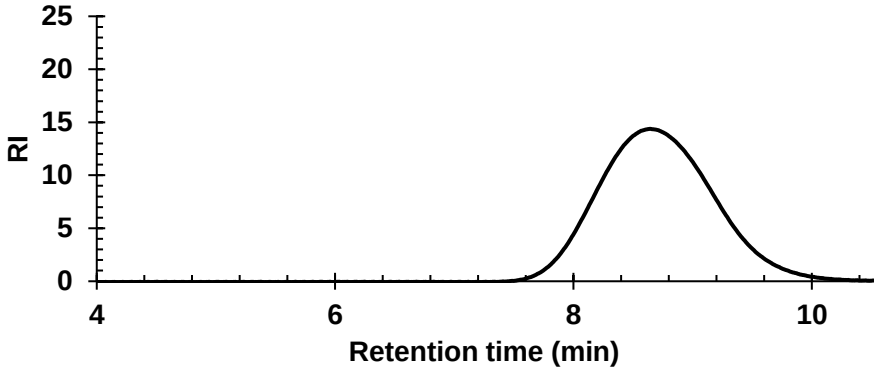

Figure A28. GPC trace of **M2** polymerized with **Ni5**.

A.6 X-Ray Crystallographic Data

The structural data for **Ni5**, the previously-published[1] **Ni4**, and the two different isolated crystalline forms of **Ni3** are presented in Table A2 along with those of a previously published Ni^{2+} species.[2] It should be noted that two forms of **Ni3** were grown under essentially the same conditions, and their crystal structures were determined more than 20 years apart. They will be designated as **m-Ni3** and **o-Ni3** herein and their molecular structures are compared below.

X-ray quality single crystals of **m-Ni3**, **o-Ni3** and **Ni5** were grown over several days from layering a concentrated solution of the complex dissolved in ethyl acetate or 1,2-dimethoxyethane (DME), respectively, with hexanes. Data was collected using MoKα radiation (λ = 0.71073) on a Bruker P4 Autodiffractometer (legacy data, **m-Ni3**) at -50 ºC or on a Bruker D8 Venture Single Crystal Diffractometer equipped with a Photon II detector (**o-Ni3** and **Ni5**) at -173 ºC. Crystal structure and refinement data is summarized in Table S1 with additional details in the deposited CIF files.

The general structural features for the first four square-planar compounds in Table A2 (Figures A29-A32) are not unexpected. All four are fairly good examples of square-planar four-coordinate d^8-Ni^{2+} with τ_4 values[3] for the first three, which all contain *cis*-coordinated monodentate O-donor ligands, ranging from 0.040 to 0.077. The τ_4 value is 0.112 for the fourth compound, **Ni5**, which contains a bidentate DME ligand. Molecules in the first three have O···O polyhedral edges that range from 2.644(7) Å to 2.738(5) Å. The O···O edge for **Ni5** which contains a bidentate DME ligand is understandably shorter at 2.565(3) Å. The C···C polyhedral edge lengths for all four range from 2.584(7) Å to 2.629(6) Å, and the C···O polyhedral edge lengths span a broader range from 2.730(6) Å to 2.884(3) Å. The C···O polyhedral edge lengths

in **Ni5** are significantly longer than those in the first three, and ω_x, ω_y, and ψ_{Ni} values all indicate that it has the largest deviation from idealized square-planar coordination. The Ni-C coordinate-covalent bond lengths for all four are quite similar with a range of 1.864(6) Å to 1.887(2) Å. The Ni-O bond lengths range from several near 1.953(4) Å for the first three molecules to the two 1.962(2) Å and 1.980(2) Å Ni-O bond lengths for **Ni5**.

As indicated above, the crystal structure of the monoclinic form of **Ni3**, which is denoted as m-**Ni3**, was determined in 2001 and the structure of the orthorhombic form, denoted as o-**Ni3**, was determined in 2024. The same solvent systems and conditions were used to obtain both forms. The **m-Ni3** crystal contained a disordered EtOAc solvent molecule of crystallization, but the o-**Ni3** crystal did not. Diffraction data for m-**Ni3** was collected on a serial diffractometer, and the data for o-Ni3 was collected with an area detector. Nonetheless, there are no significant (>3 s.u.) differences in their coordinate-covalent bond lengths and only slightly more significant differences in bond angles. However, one clear difference is the approximately 50% lower precision obtained for the earlier **m-Ni3** structure relative to the recent structure for **o-Ni3**. While this difference in precision could be solely due to the two different crystalline forms of **Ni3** and/or disordered solvent present in the **m-Ni3** structure, it is most likely due to the better/improved instrumentation that is presently available and the ability to quickly collect more extensive and redundant high-quality data sets.

While seeing this close agreement for bond lengths and angles for **m-Ni3** and **o-Ni3** was gratifying, the observation that the 25 atoms of their neutral $(C_6F_5)_2NiO_2$ cores could be superimposed with a root-mean-square estimated standard deviation (RMSD) of 0.14 Å was even more so (see Figure A33). Omitting the two coordinated oxygen atoms reduced the

superposition RMSD to 0.09 Å. Packing forces, if nothing else, might be expected to prevent such a close similarity. Somewhat more surprising was the fact that the 25 atom $(C_6F_5)_2NiO_2$ cores of **Ni4** and **Ni5** also superimposed quite well with the one for **m-Ni3** with 25- and 23-atom OFIT RMSD values of 0.20 Å and 0.18 Å, respectively for **Ni4** and 0.44 Å and 0.0.09 Å, respectively for **Ni5**. The larger RMSD value for the 25-atom superposition for **Ni5** is obviously due to the $-CH_2CH_2-$ link between the coordinated DME oxygen atoms.

A detailed examination of the entries in Table A2 reveals that the Ni···F contacts systematically break down into two pairs for both Ni3 molecules as well as all others containing *cis*- C_6F_5 rings. The *ortho*-F atoms on each C_6F_5 ring will be placed near the Ni atom when the ligand binds to the metal. The data in Table S2 indicate that these Ni···F contacts are all near the 3.10 Å sum of the van der Waals radii for Ni and F[4]. Closer examination reveals that there is a shorter Ni···F_S pair for F atoms closer to the square-planar grouping and a longer Ni···F_L pair. Although the shorter pair for each molecule is still much longer than the short 2.594(5) Å pair observed in pseudo-octahedral compound 5 of Table A2 where the two *ortho*-fluorine atoms in C_6F_5 are replaced by two CF_3 groups[2], there is a similar trend to form a short Ni···F_S pair for compounds 1-4. Both CF_3 groups in 5 rotated about their C-C bonds to produce the short Ni···F interaction instead of rotating to minimize the interaction. Each C_6F_5 ring in the present group of $(C_6F_5)_2NiO_2$ complexes is clearly tipped slightly toward the Ni atom. Molecules in m-Ni3 and o-Ni3 both possess rigorous crystallographically-imposed C_2 symmetry, and the others possess pseudo-C_2 symmetry.

Tipping of the (C_6F_5) rings toward the Ni atom in 1-4, produces one shorter Ni···F_S contact and one longer Ni···F_L contact in each. The fluorine with the shorter Ni···F_S separation is

slightly closer to the mean plane of the 5-atom Ni square-planar unit. Since the Ni^{2+} ion in both Ni3 structures sits on a crystallographic C_2-axis, there will be two identical Ni···F_S contacts in each molecule with a highly obtuse F_S···Ni···F_S angle near 152°. There will also be two identical contacts in each molecule with a smaller F_L···Ni···F_L angle. This tipping should also produce smaller Ni-C_1-C_S angles for the short Ni···F_S contact and larger Ni-C_1-C_L angles for the long Ni···F_L contact. This is the case. Very similar relationships exist for 3 and 4, but they are not imposed by rigorous crystallographic C_2 symmetry.

The data in Table A2 show that this short nonbonded Ni···F_S interaction in 5 results in a more pronounced tipping of each coordinated phenyl ring toward the Ni atom than was observed with the pentafluorophenyl ligands. This produces even larger differences between the Ni-C_1-C_S and Ni-C_1-C_L angles for the *ortho* phenyl carbons containing CF_3 groups, one of which is involved in a short nonbonding interaction with the Ni.

Given these similarities for 1-4, it is probably not surprising that other species containing the neutral $(C_6F_5)_2Ni$ synthon have solid-state structures with their 25-atom $(C_6F_5)_2NiO_2$ or 23-atom $(C_6F_5)_2Ni$ groups being closely superimposable on those same atoms for m-Ni3. They also have the same pairs of Ni---F_S and Ni···F_L separations with F_S···Ni···F_S angles near 150°. The dicarbonyl complex $(C_6F_5)_2Ni(CO)_2$[1] with crystallographically-imposed C_2 symmetry has Ni···F_S and Ni···F_L separations of 3.046(3) Å and 3.150(3) Å, respectively with a F_S···Ni···F_S angle of 152.0(2)°. The Ni-C_1-C_S and Ni-C_1-C_L angles are 120.3(2) ° and 124.2(2) °, respectively. Atoms of the 25-atom $(C_6F_5)_2NiO_2$ group overlap with those for m-Ni3 with a RMSD displacement of 0.11 Å while the RMSD displacement for the 23-atom $(C_6F_5)_2Ni$ groups is

reduced to 0.09 Å due to removal of the two *trans*-coordinated atoms and the difference in the Ni-O and Ni-C(carbonyl) bond lengths.

The larger OFIT RMSD values for each of the 25-atom superpositions relative to the 23-atom superpositions appears to not only be caused by having different ligands situated *trans* to the coordinated (C_6F_5) ligands but also by a slight tetrahedral distortion of the square-planar Ni coordination. The *trans*-coordinated atoms always have large, if not the largest, individual displacements for the 25-atom $(C_6F_5)_2NiO_2$ superpositions.

Table A1. Crystal and Refinement data for m-**Ni3**, o-**Ni3** and **Ni5**.

Code	m-Ni3[a]	o-Ni3[a]	Ni5
CCDC accession code	2348761	2354741	2354742
Empirical formula	$C_{12}H_{12}F_5Ni_{0.50}O_3$[b]	$C_{20}H_{16}F_{10}NiO_4$	$C_{16}H_{10}F_{10}NiO_2$
Formula weight	328.57	569.04	482.95
Temperature, K	223(2)	105(2)	105(2)
Wavelength	0.71073	0.71073	0.71073
Crystal system	Monoclinic	Orthorhombic	Orthorhombic
Space group	*C2/c*	*Fdd*2	$P2_12_12_1$
a	18.560(3)	33.679 (3) Å	18.034 (1) Å
b	13.051(2)	10.6879 (7) Å	8.8772 (5) Å
c	13.715 (1)	11.8081 (8)Å	10.9076 (6) Å
α	90°	90°	90°
β	117.735(9)	90°	90°
γ	90°	90°	90°
Volume	2940.4(6)	4250.4 (5) $Å^3$	1746.2 (2)$Å^3$
Z	8	8	4
Density (calculated)	1.484 g/cm^3	1.778 g/cm^3	1.837 g/cm^3
Absorption coefficient	0.76 mm^{-1}	1.03 mm^{-1}	1.22 mm^{-1}
F(000)	1336.0	2288.0	960.0

Crystal size	0.60 x 0.35 x 0.15 mm^3	0.31 × 0.12 × 0.09 mm^3	0.43 × 0.31 × 0.26 mm^3
Theta range	2.2 to 26.4°	2.6 to 26.7°	2.6 to 27.5°
Index ranges	$-1 \leq h \leq 23$, $-16 \leq k \leq 1$, $-17 \leq l \leq 15$	$-42 \leq h \leq 42$, $-13 \leq k \leq 13$, $-14 \leq l \leq 14$	$-23 \leq h \leq 23$, $-11 \leq k \leq 11$, $-14 \leq l \leq 13$
Reflections collected	3598	36534	41485
Independent reflections	3005 [R_{int} = 0.0310, R_{sigma} = 0.0621]	2238 [R_{int} = 0.0491, R_{sigma} = 0.0216]	4022 [R_{int} = 0.0430, R_{sigma} = 0.0233]
Completeness/θ_{max}	99.6%/26.40	98.9%/26.73	99.8%/27.5
Absorption correction	Empirical	Multi-scan	Multi-scan
Max./Min. Transmission	0.710 and 0.648	0.739 and 0.691	0.746 and 0.631
Refinement method	Full-matrix least-squares on F^2	Full-matrix least-squares on F^2	Full-matrix least-squares on F^2
Data/restraints/parameters	3005/12/202	2238/1/162	4022/0/265
Goodness-of-fit on F^2	1.05	1.04	1.12
Final R indices [I>2σ(I)]	R_1 = 0.0618, wR_2 = 0.1440	R_1 = 0.0169, wR_2 = 0.0401	R_1 = 0.0229, wR_2 = 0.0575
R indices (all data)	R_1 = 0.1102, wR_2 = 0.1695	R_1 = 0.0183, wR_2 = 0.0408	R_1 = 0.0236, wR_2 = 0.0578
Largest diff. peak & hole	0.32/-0.30 e $Å^{-3}$	0.19/-0.14 e $Å^{-3}$	0.34/-0.27 e $Å^{-3}$
Absolute Structure Parameter	-	0.02(1)	0.11(1)

[a] The codes **m-Ni3** and **o-Ni3** are used to distinguish between the monoclinic and orthorhombic forms of $(C_6F_5)_2Ni(EtOAc)_2$, respectively. The monoclinic form of the structure was determined in 2001 and found to contain a severely disordered solvent molecule of crystallization. It is included here for a comparison of metrical parameters.

[b] For **m-Ni3** (the monoclinic form of **Ni3**), the $CH_3CO_2C_2H_5$ solvent molecule of crystallization is disordered about the crystallographic C2 axis located at (1/2, y, 3/4) in the unit cell and not all of the solvent nonhydrogen atoms were successfully located with the 2001 data. The values

reported here are based on the formulation of ½ $CH_3CO_2C_2H_5$ solvent molecule per asymmetric unit.

Appendix B: Supporting Information for Chapter III

B.1 GPC Traces

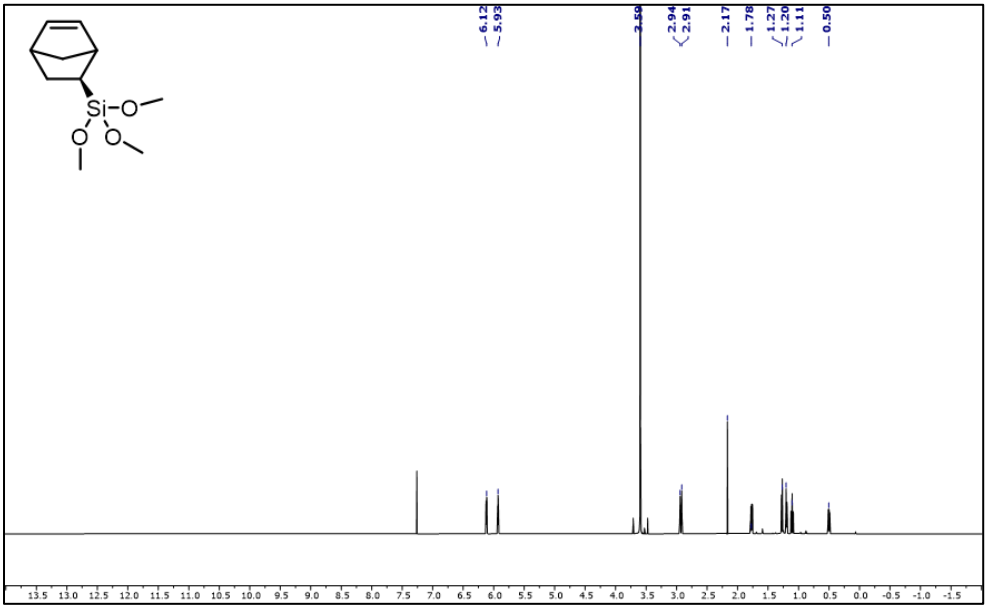

Figure B1. ^{1}H NMR spectrum of **M1$_{Exo}$** in $CDCl_3$.

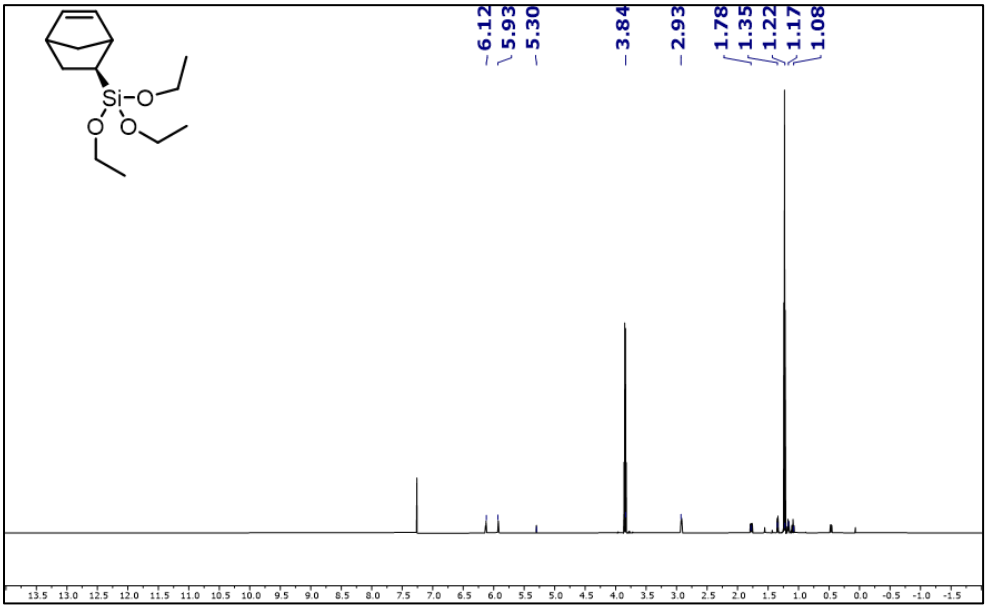

Figure B2. ^{1}H NMR spectrum of **M2$_{Exo}$** in $CDCl_3$.

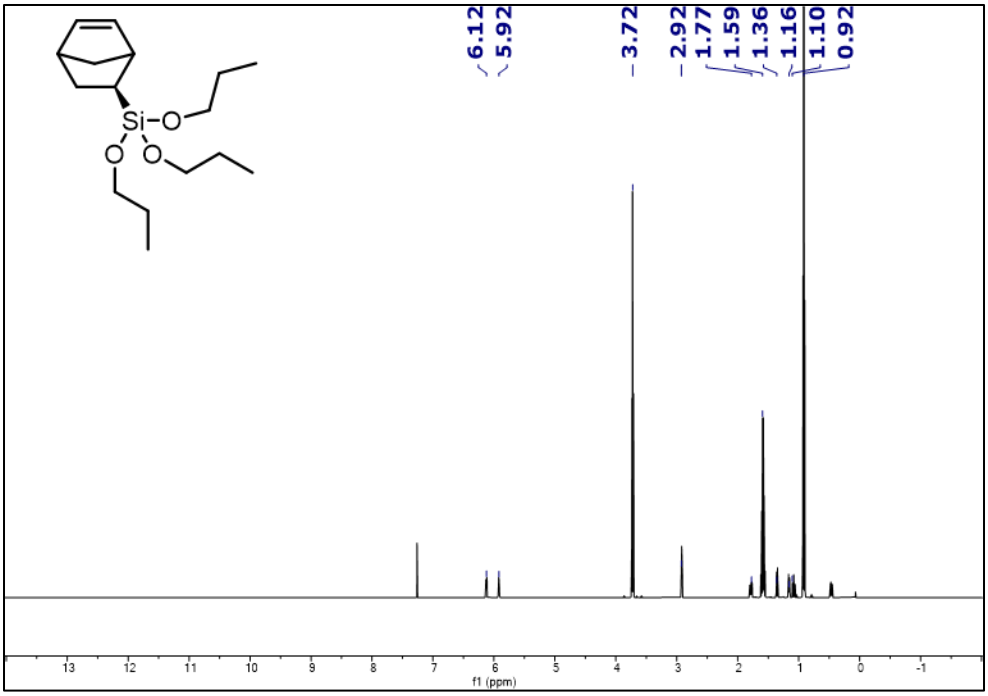

Figure B3. ^{1}H NMR spectrum of **M3$_{Exo}$** in $CDCl_3$**.**

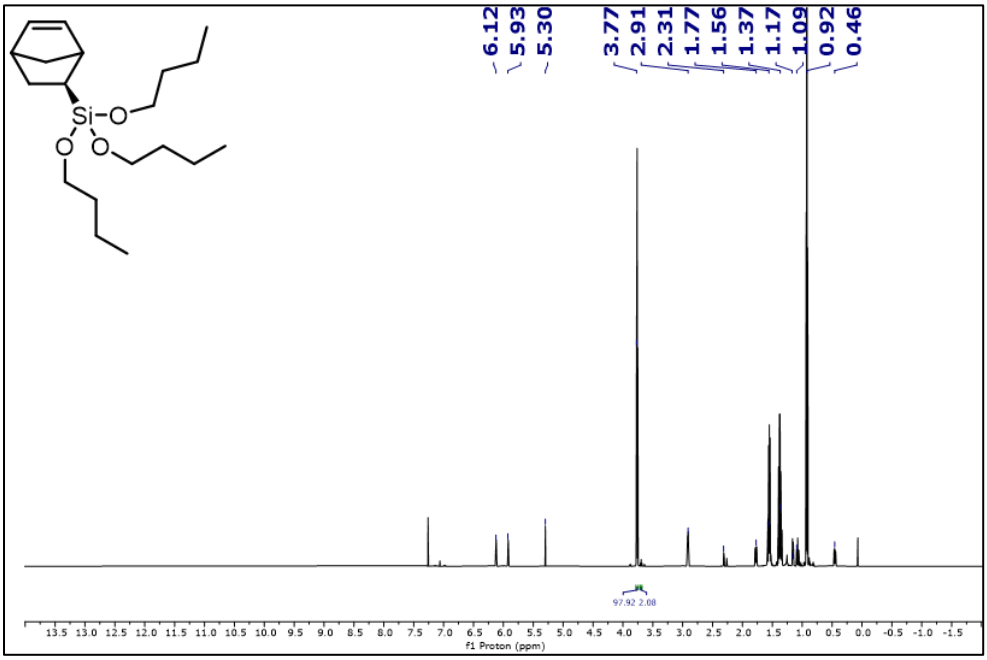

Figure B4. ^{1}H NMR spectrum of **M4$_{Exo}$** in $CDCl_3$.

B.2 GPC Traces

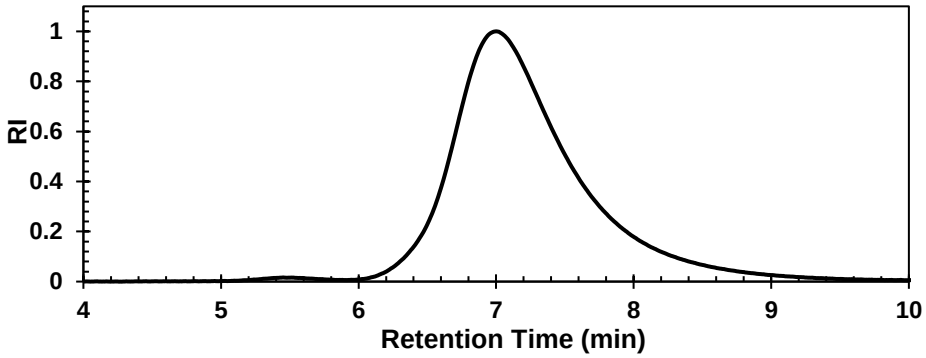

Figure B5. GPC trace of **P1$_{Mix}$**.

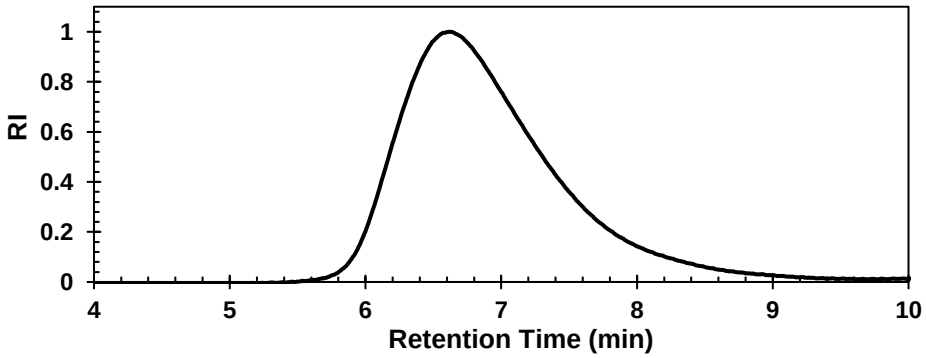

Figure B6. GPC trace of **P1$_{Exo}$**.

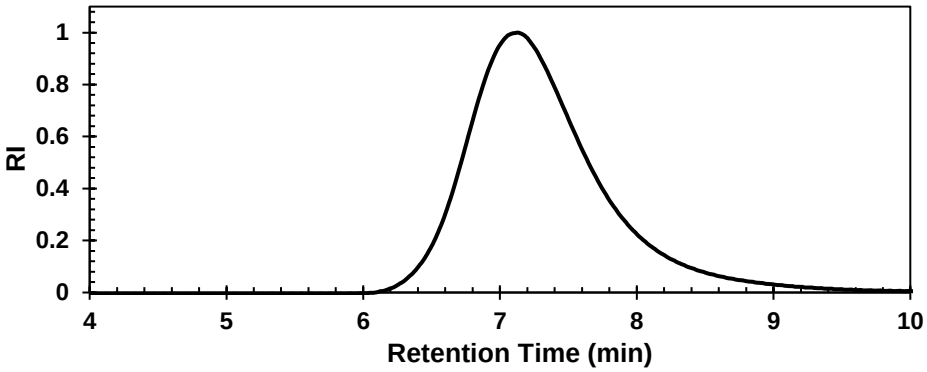

Figure B7. GPC trace of **P2$_{Mix}$**.

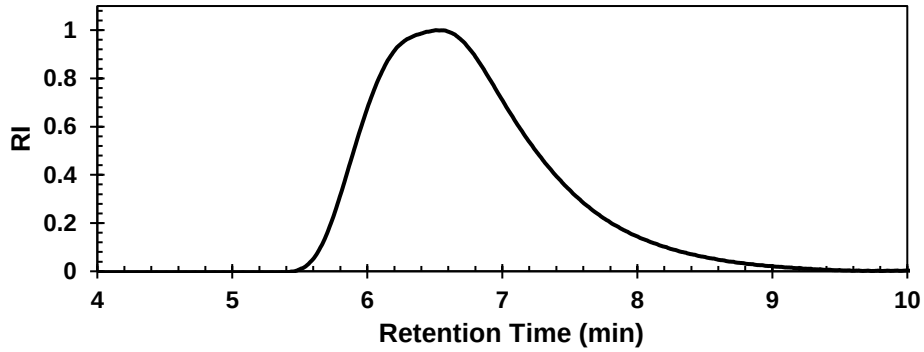

Figure B8. GPC trace of **P2$_{Exo}$**.

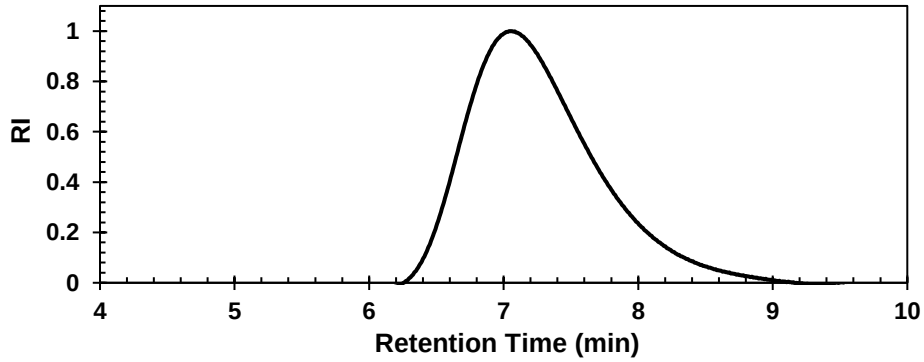

Figure B9. GPC trace of **P3$_{Mix}$**.

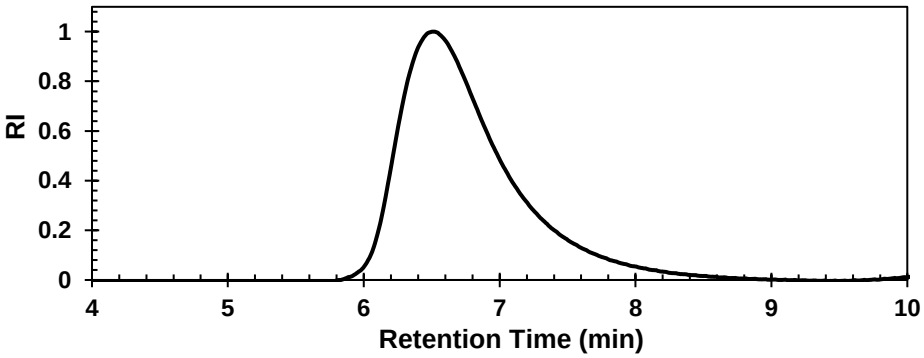

Figure B10. GPC trace of **P3$_{Exo}$**.

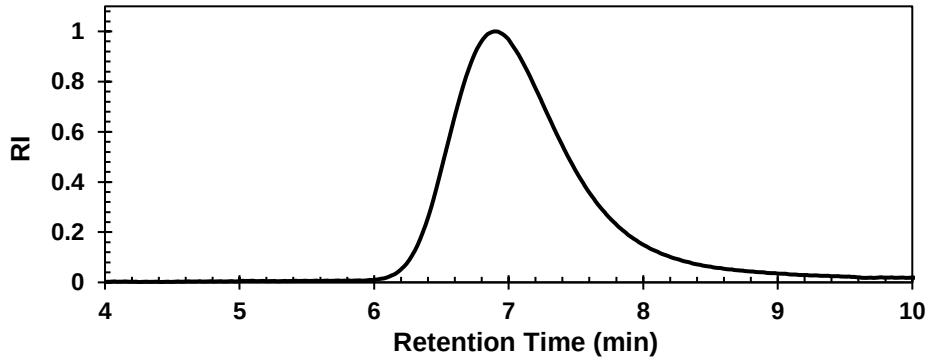

Figure B11. GPC trace of **P4$_{Mix}$**.

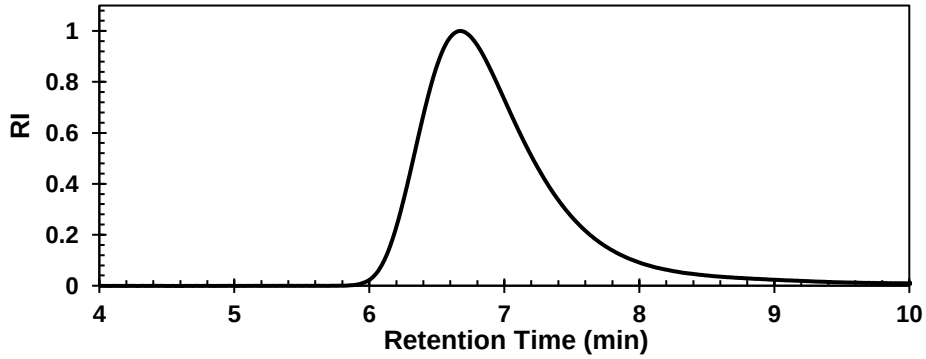

Figure B12. GPC trace of **P4$_{Exo}$**.

Appendix C: Supporting Information for Chapter IV

C.1 NMR Spectra

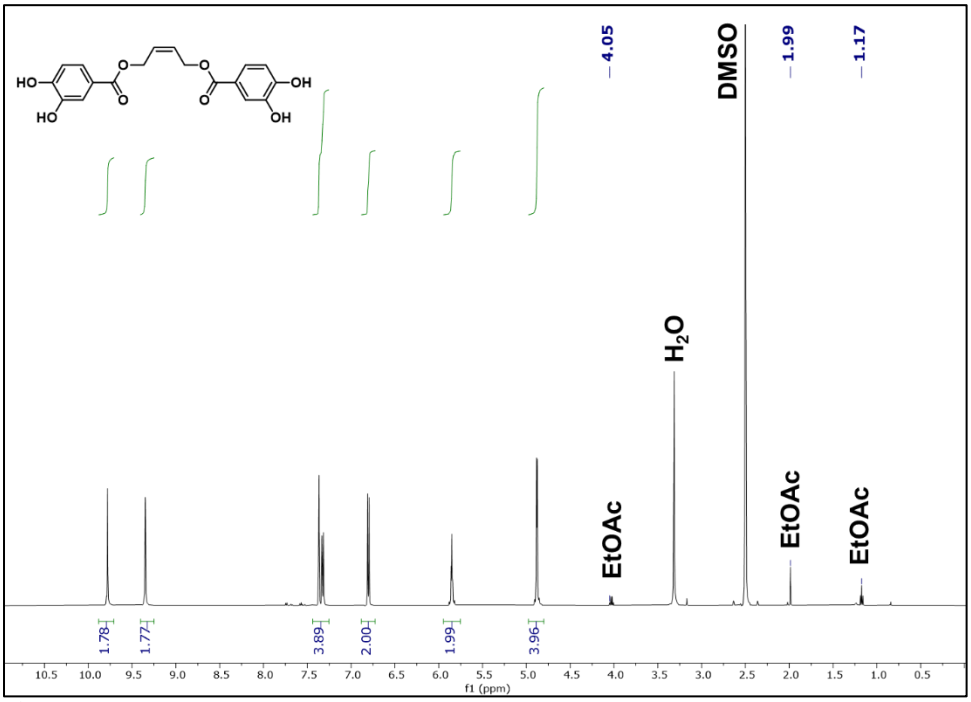

Figure C1. ^{1}H NMR of **CTA-1**.

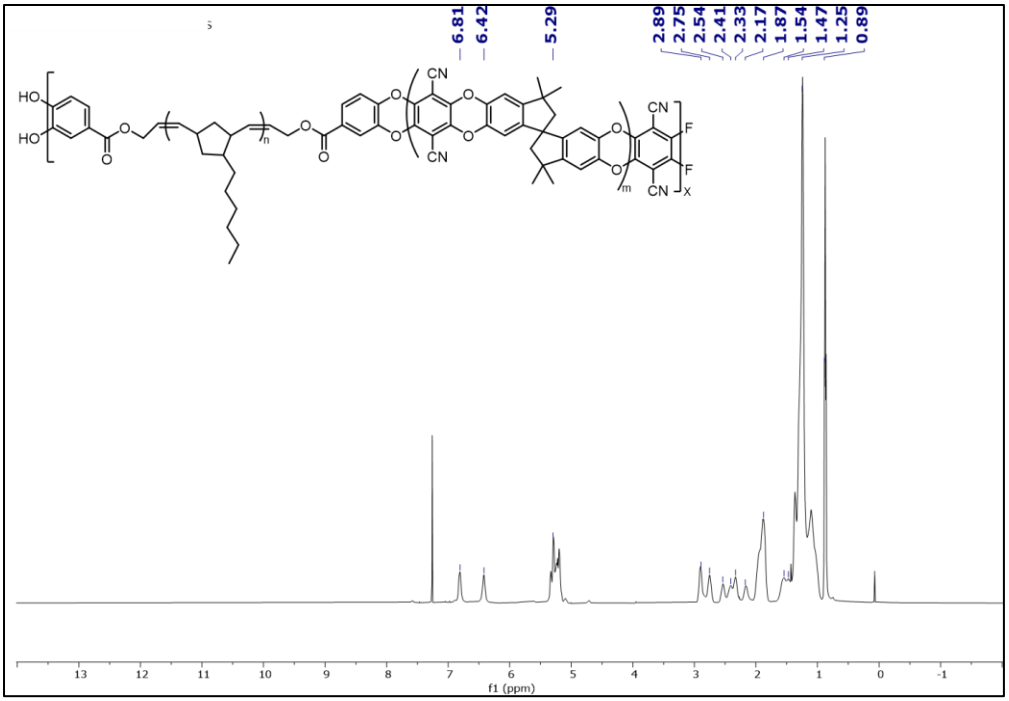

Figure C2. ^{1}H NMR spectrum of $\mathbf{P^{10:10}}$.

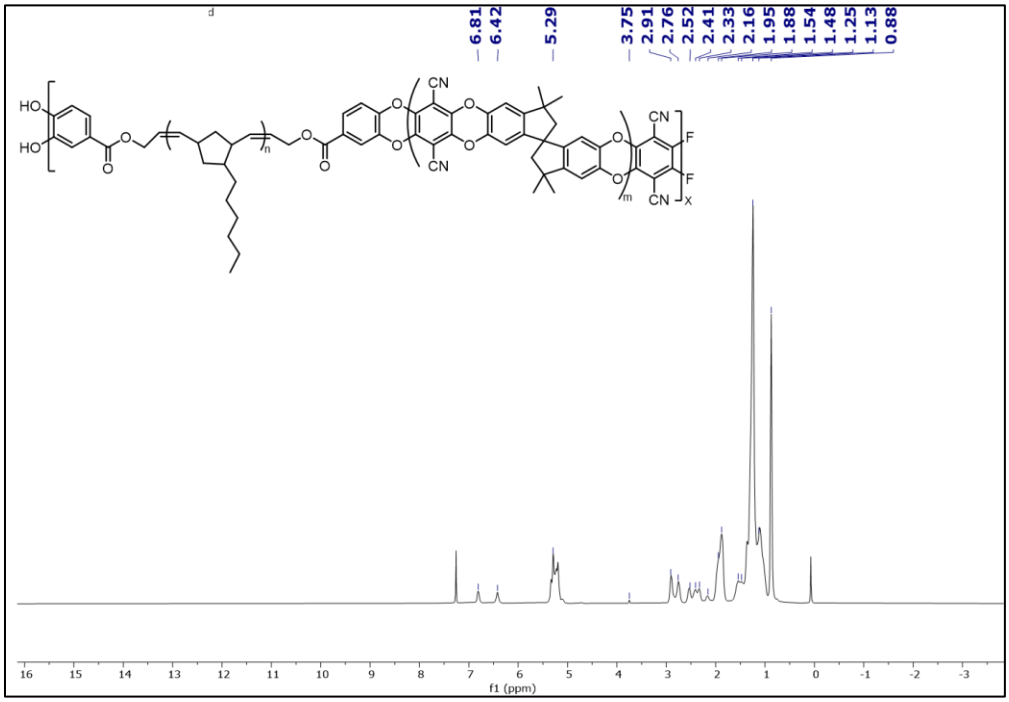

Figure C3. ^{1}H NMR spectrum of $\mathbf{P^{10:25}}$.

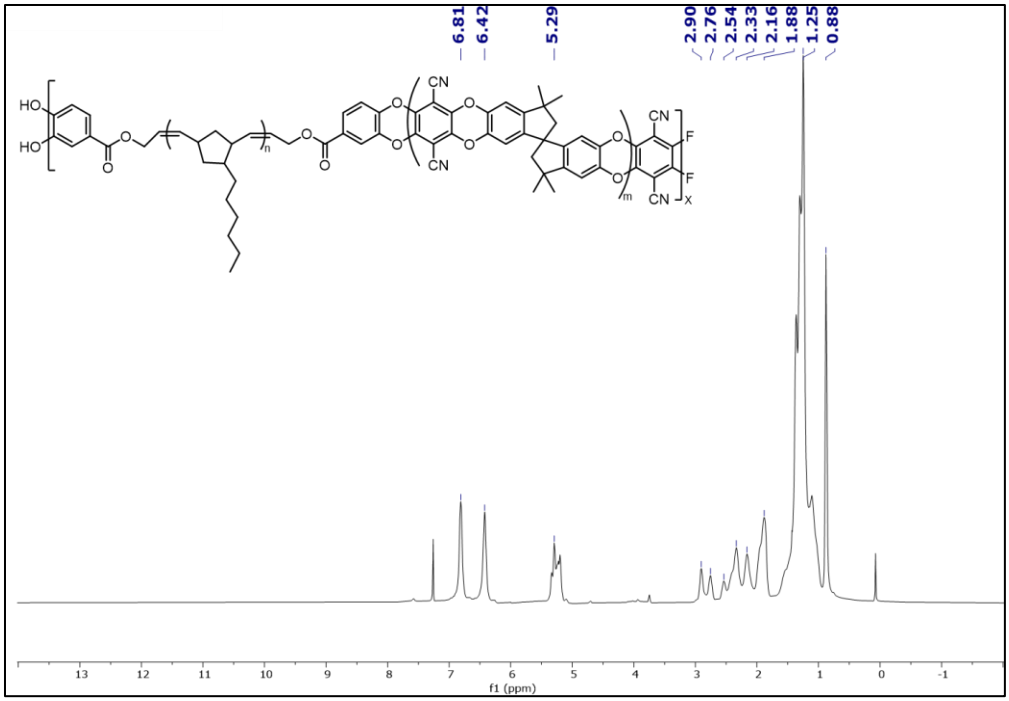

Figure C4. ^{1}H NMR spectrum of $\mathbf{P_{10:40}}$.

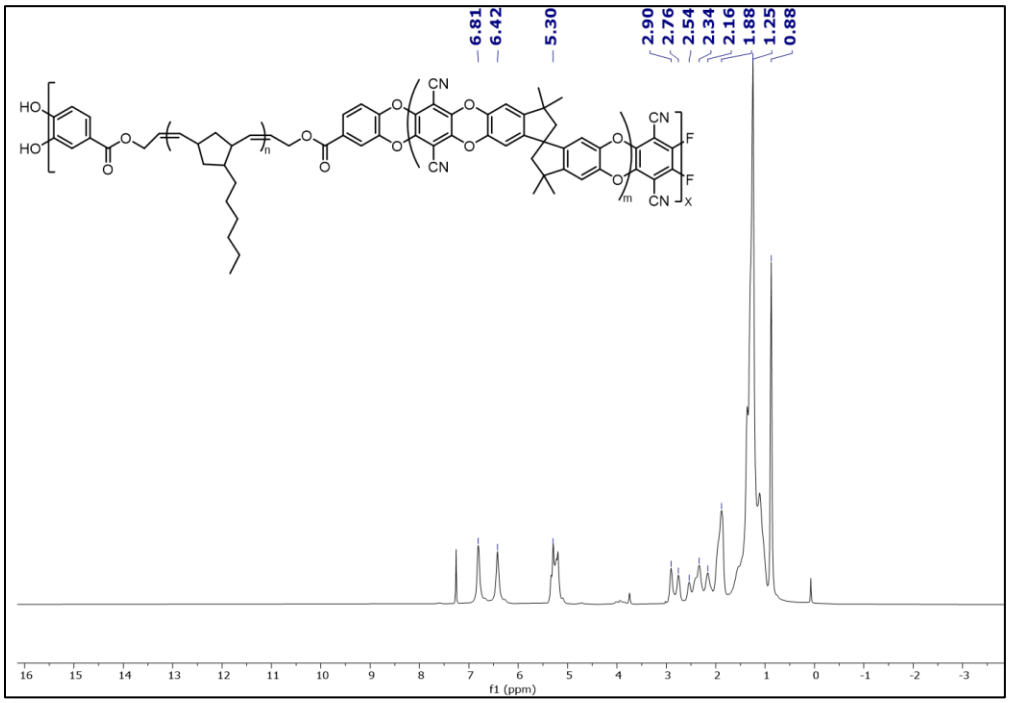

Figure C5. ^{1}H NMR spectrum of $\mathbf{P^{25:10}}$.

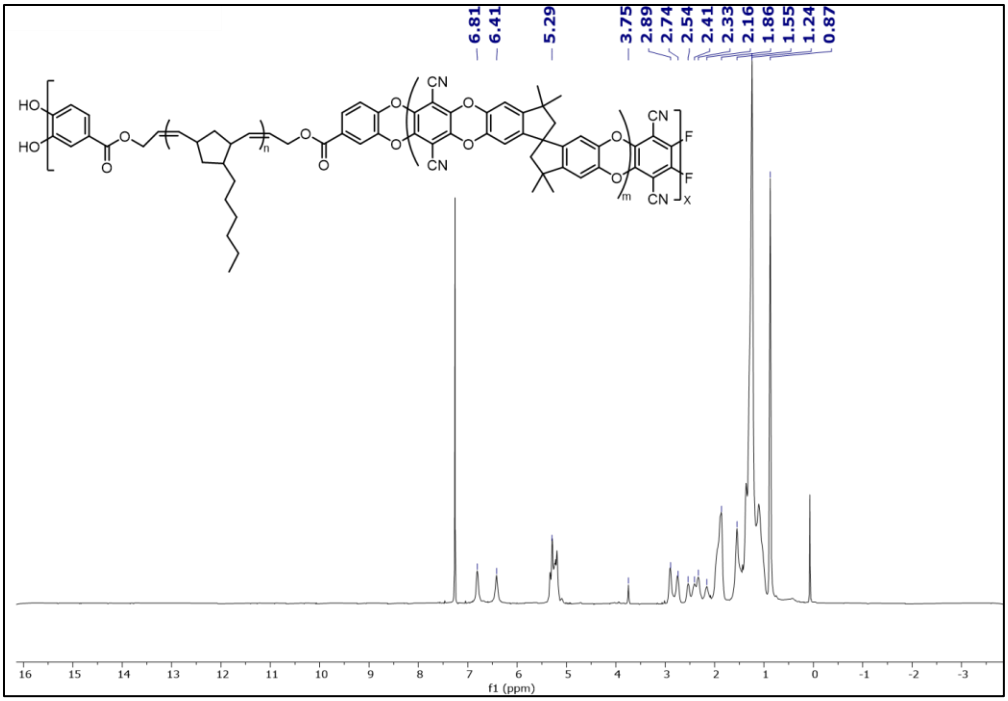

Figure C6. ^{1}H NMR spectrum of $\mathbf{P^{25:25}}$.

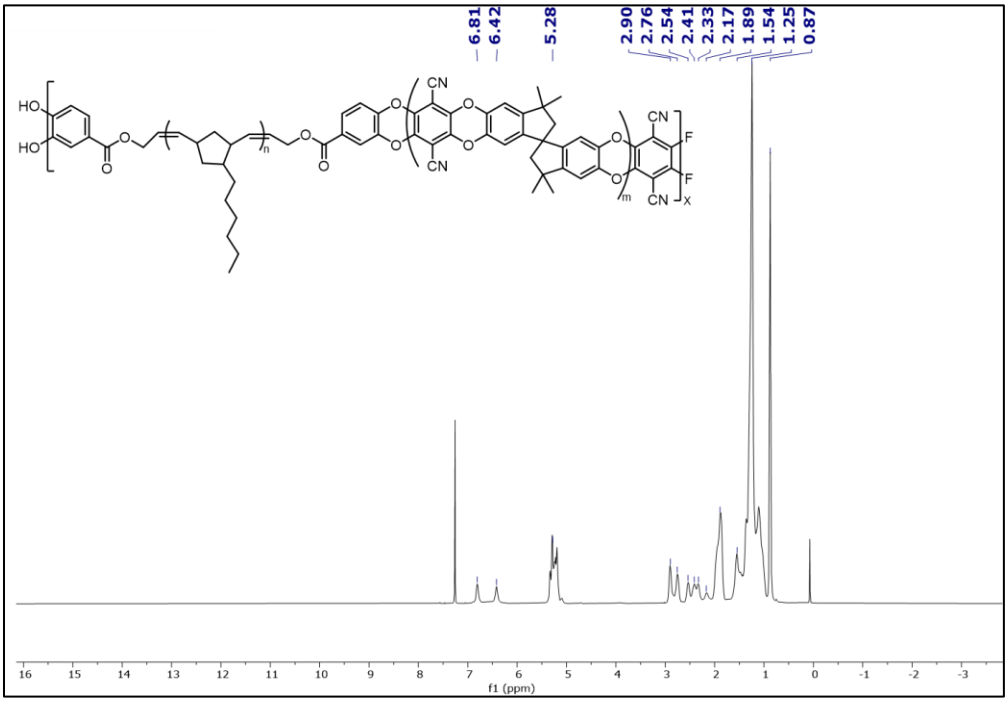

Figure C7. ^{1}H NMR spectrum of $\mathbf{P^{25:40}}$.

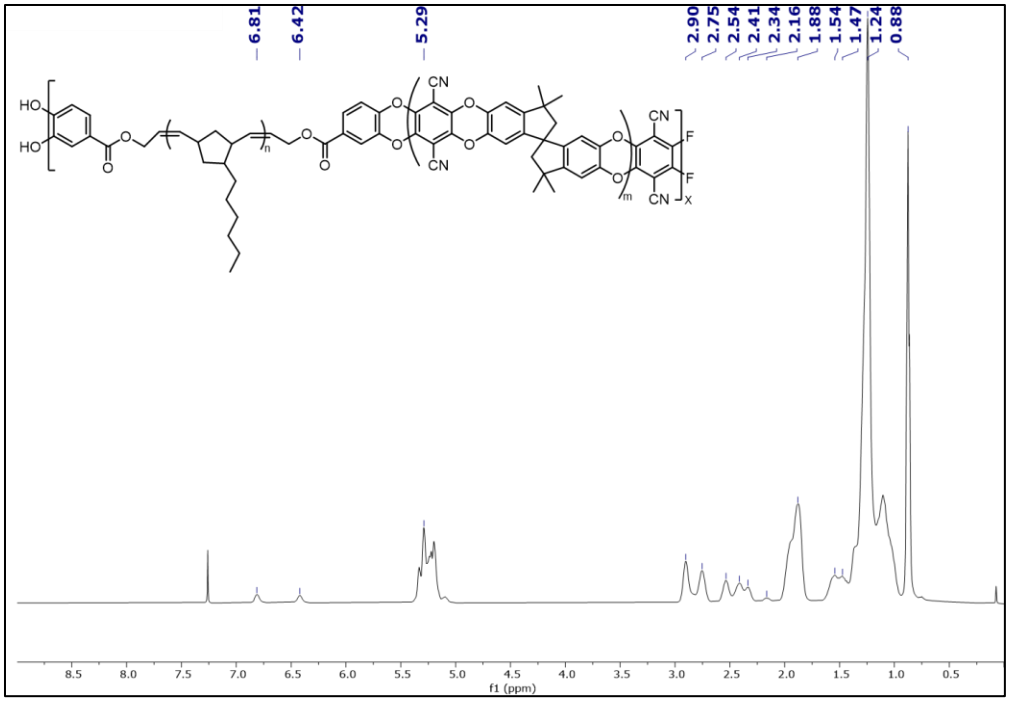

Figure C8. ^{1}H NMR spectrum of $\mathbf{P^{25:10}}$.

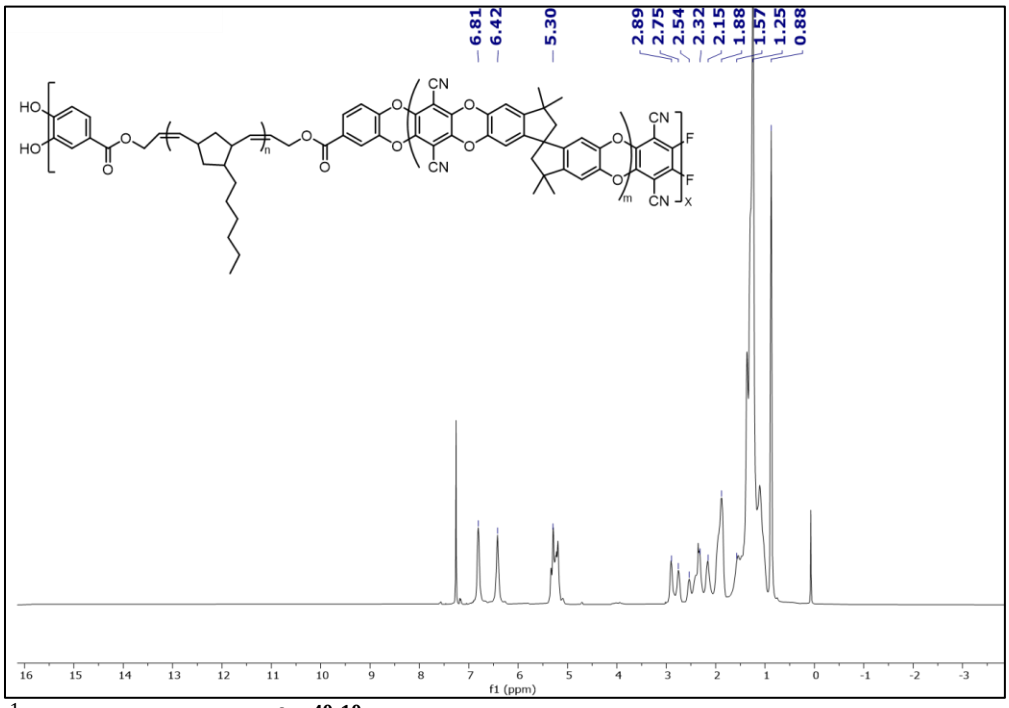

Figure C9. ^{1}H NMR spectrum of $\mathbf{P^{40:10}}$.

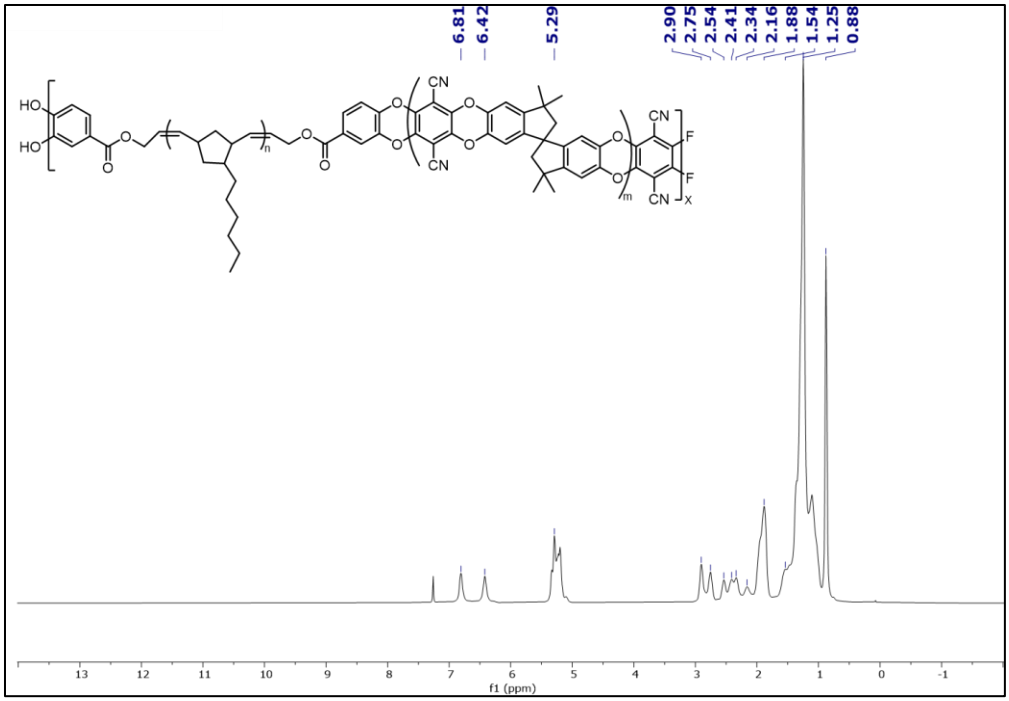

Figure C10. ^{1}H NMR spectrum of $\mathbf{P^{40:40}}$.

C.2 DOSY Spectra of Copolymers

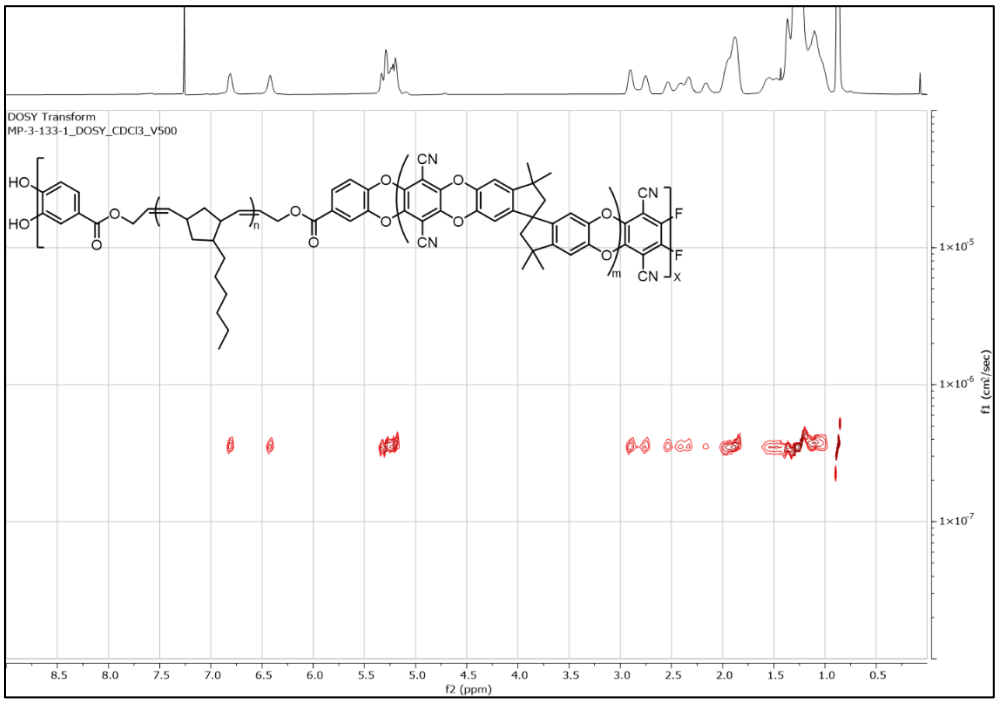

Figure C11. DOSY spectrum of $\mathbf{P^{10:10}}$.

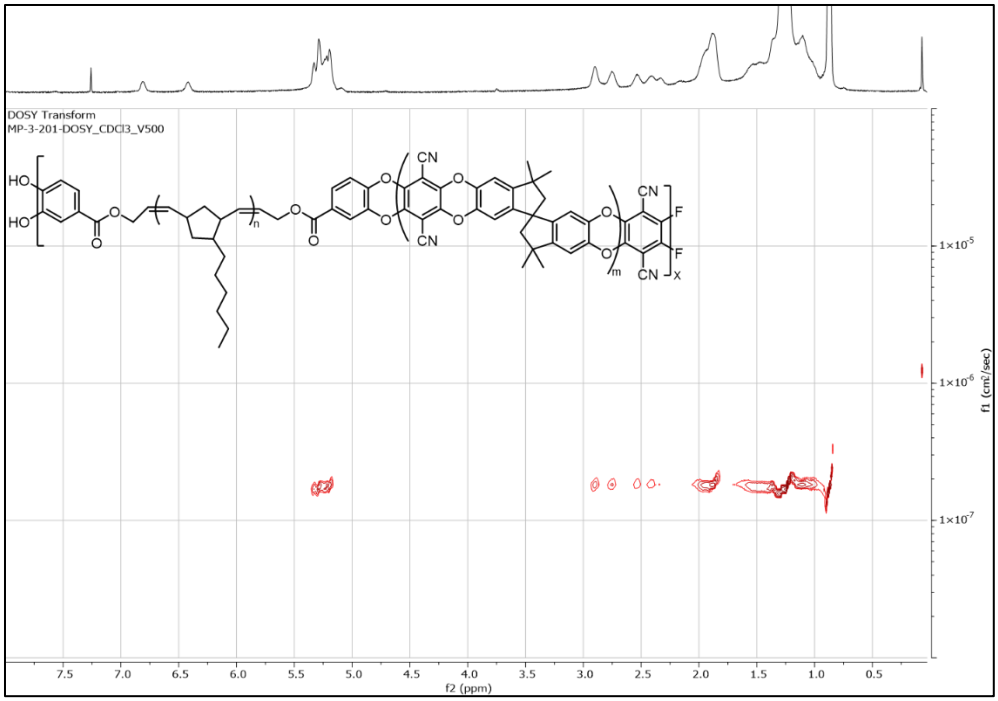

Figure C12. DOSY spectrum of $\mathbf{P^{10:25}}$.

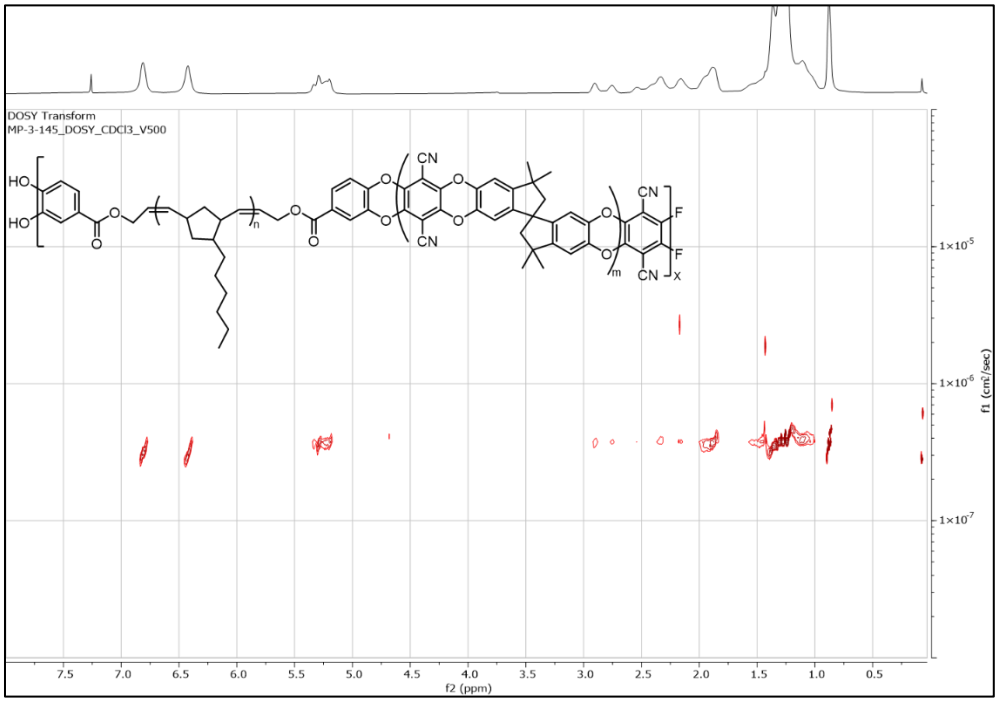

Figure C13. DOSY spectrum of $\mathbf{P^{10:40}}$.

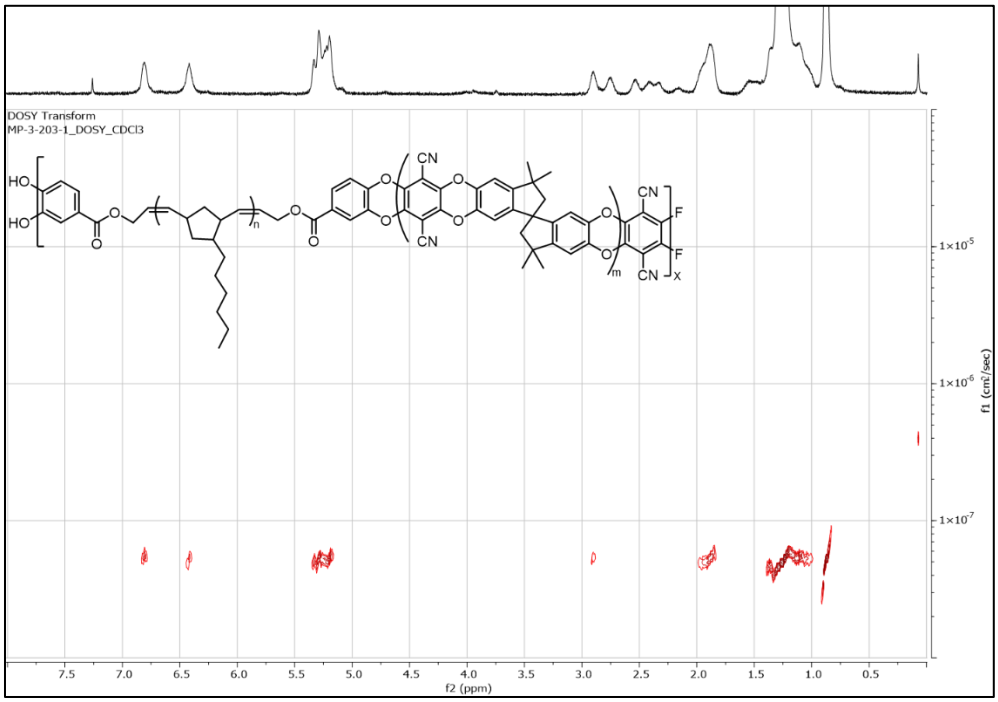

Figure C14. DOSY spectrum of $\mathbf{P^{25:10}}$.

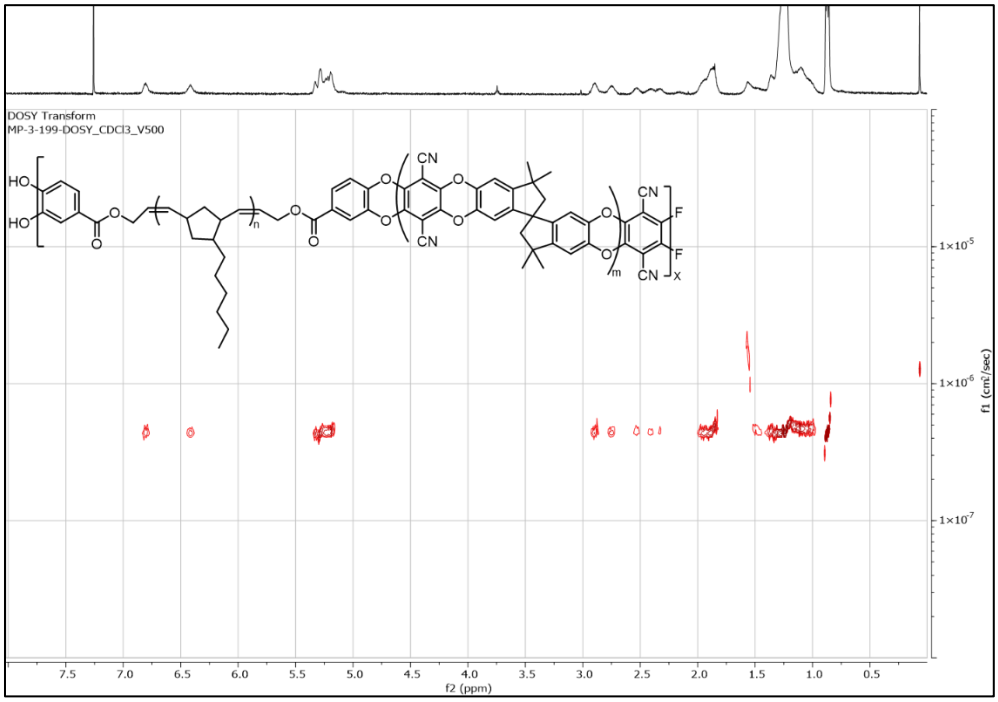

Figure C15. DOSY spectrum of $\mathbf{P^{25:25}}$.

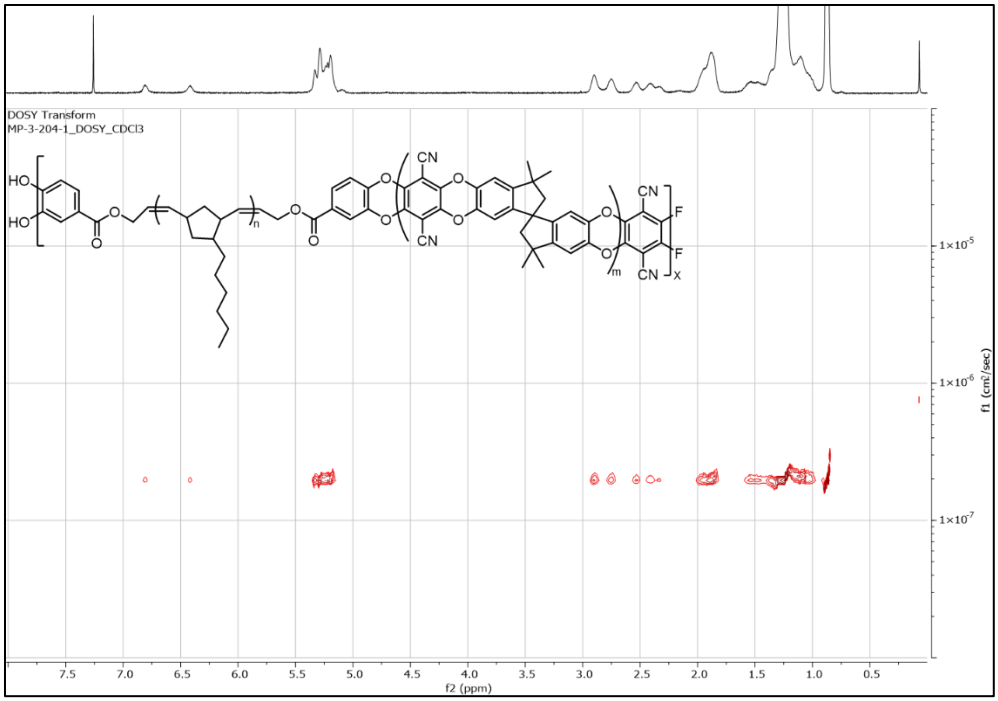

Figure C16. DOSY spectrum of $\mathbf{P^{25:40}}$.

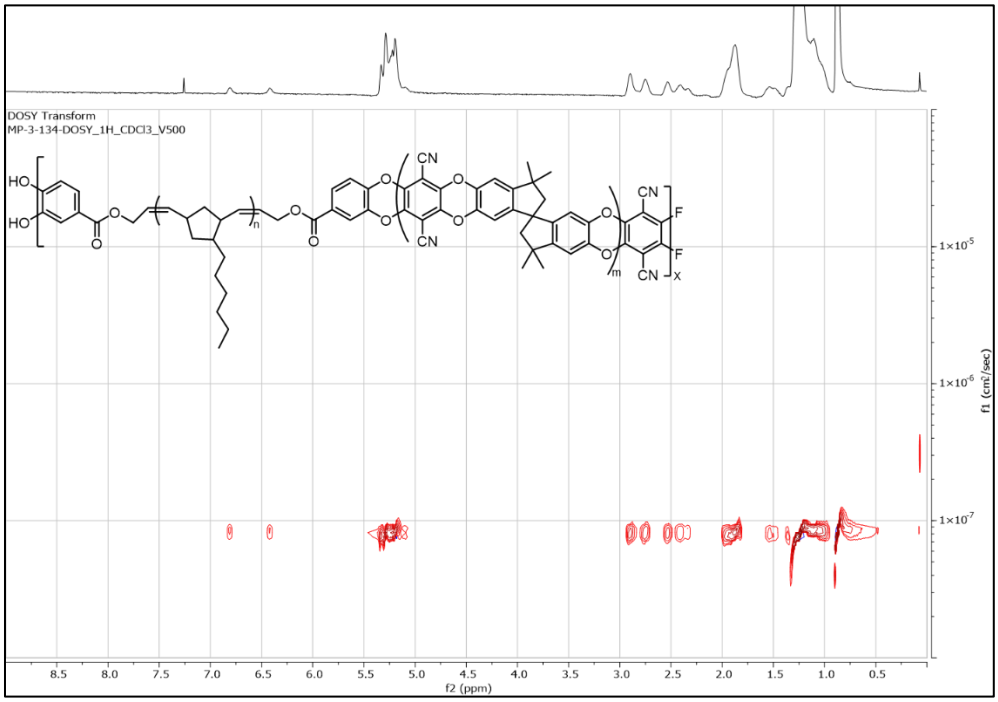

Figure C17. DOSY spectrum of $\mathbf{P^{40:10}}$.

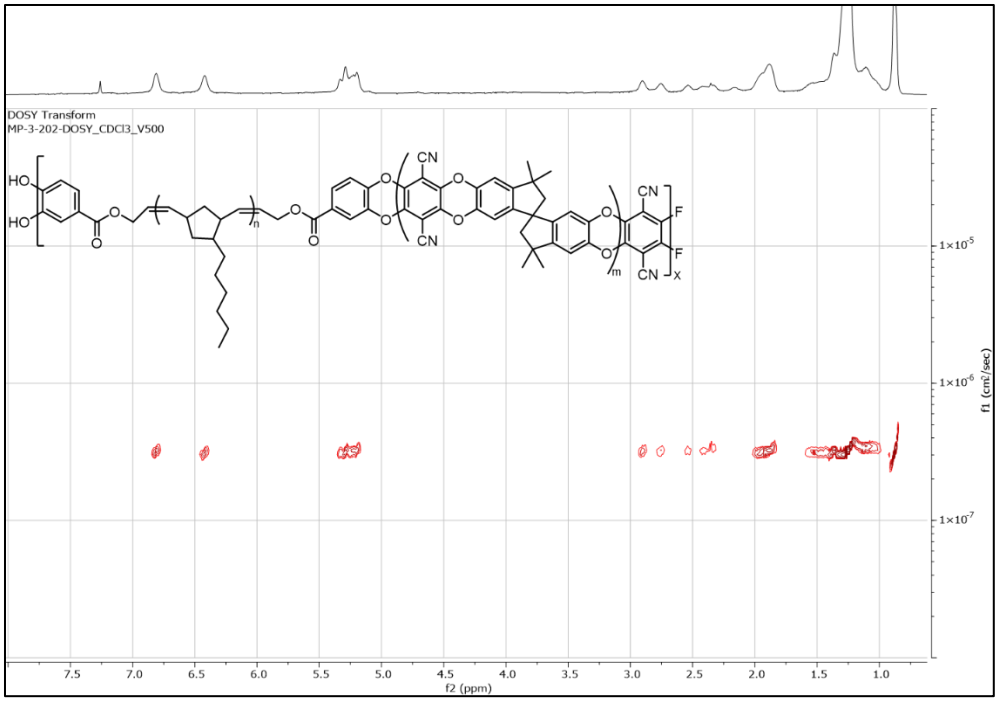

Figure C18. DOSY spectrum of $\mathbf{P^{40:25}}$.

C.2 GPC Traces

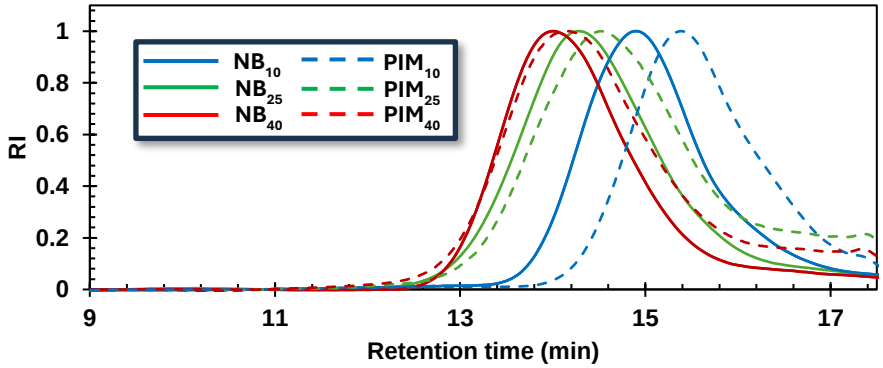

Figure C19. GPC trace of **PIM-1** homopolymers (dashes) and **PNB** homopolymers (solid).

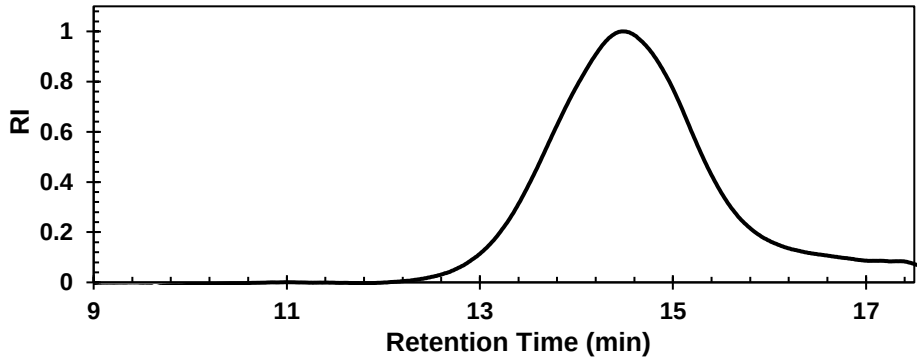

Figure C20. GPC trace of $\mathbf{P^{10:10}}$.

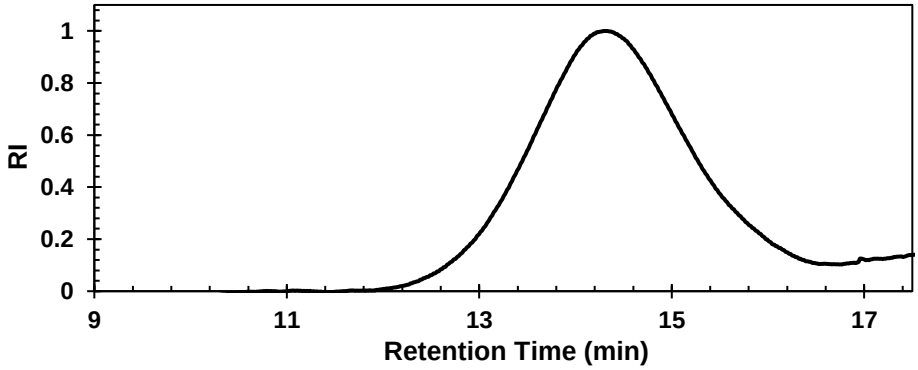

Figure C21. GPC trace of $\mathbf{P^{10:25}}$.

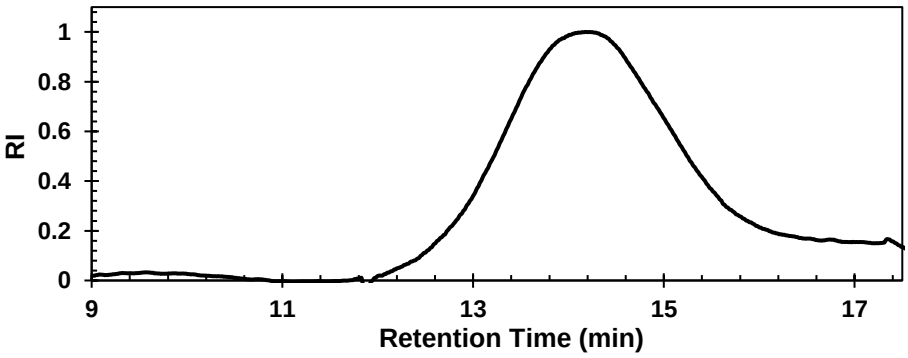

Figure C22. GPC trace of $\mathbf{P^{10:40}}$.

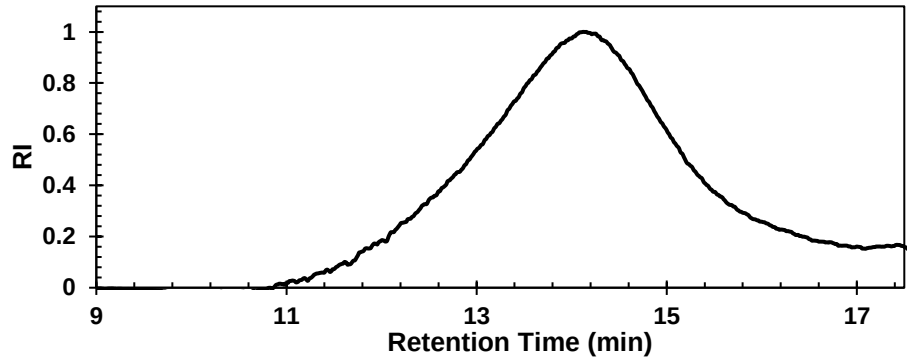

Figure C23. GPC trace of $\mathbf{P^{25:10}}$.

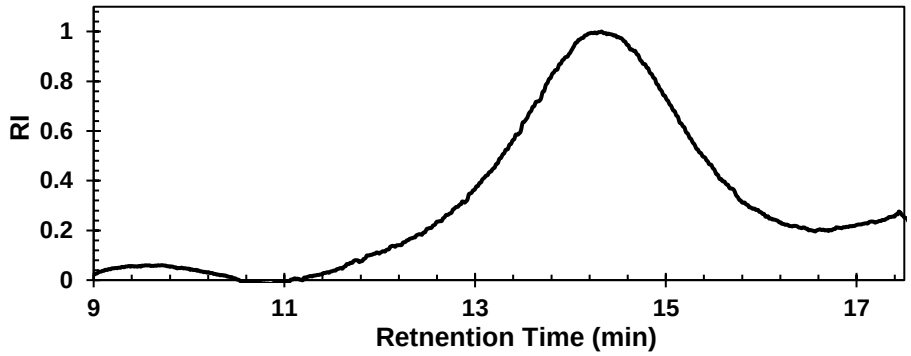

Figure C24. GPC trace of $\mathbf{P^{25:25}}$.

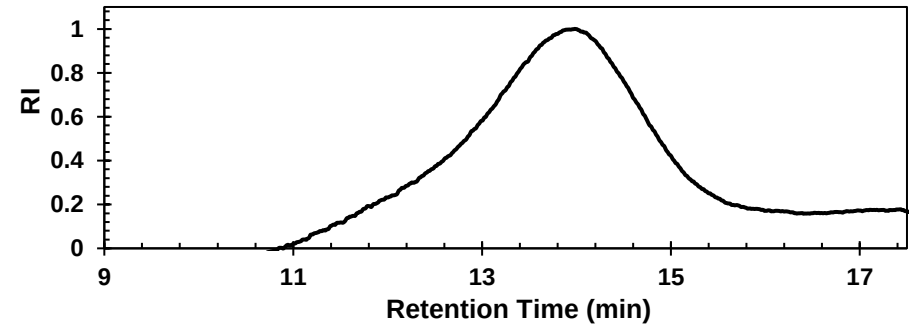

Figure CS25. GPC trace of $\mathbf{P^{25:40}}$.

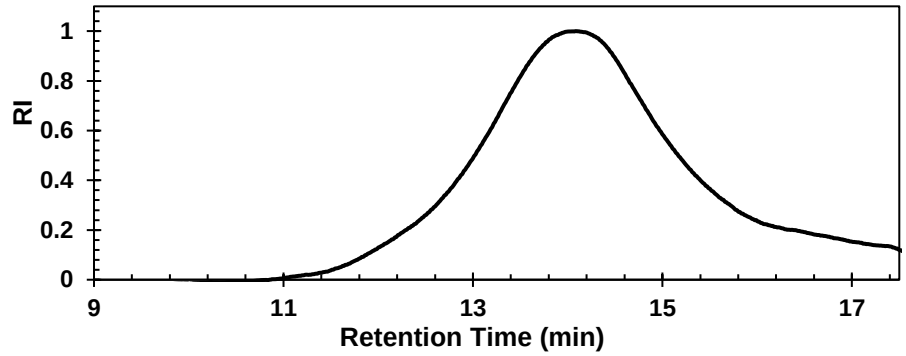

Figure C26. GPC trace of **P$^{40:10}$.**

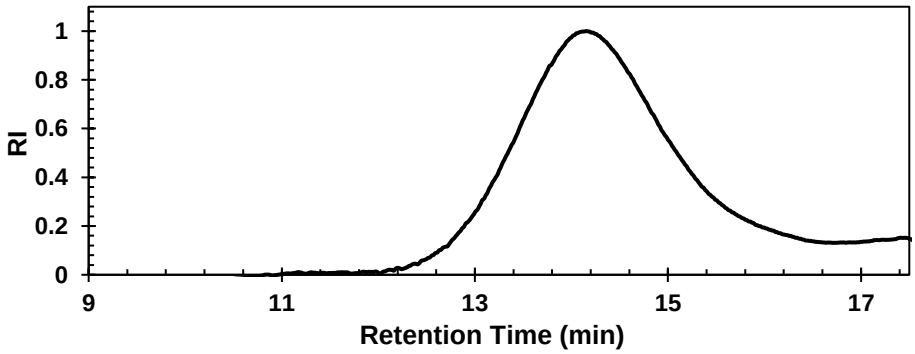

Figure C27. GPC trace of **P$^{40:25}$**.

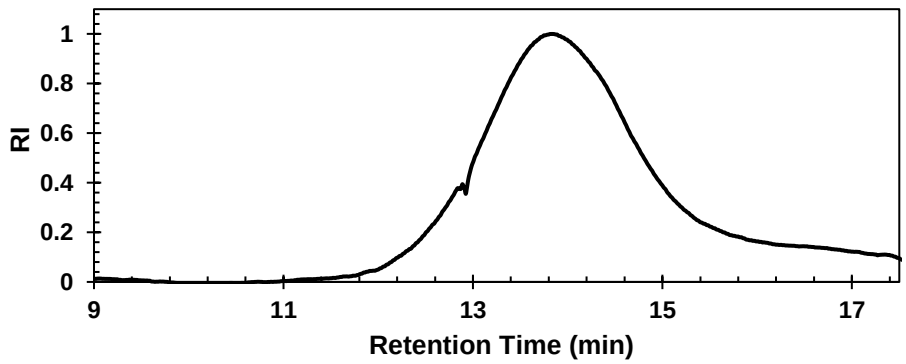

Figure C28. GPC trace of **P$^{40:40}$**.

C.4 Gas Transport Data

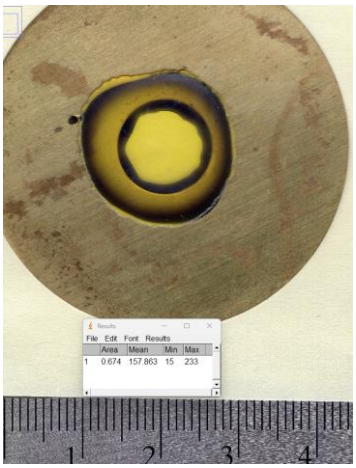

Figure C29. Example surface area measurement of permeation sample using ImageJ.

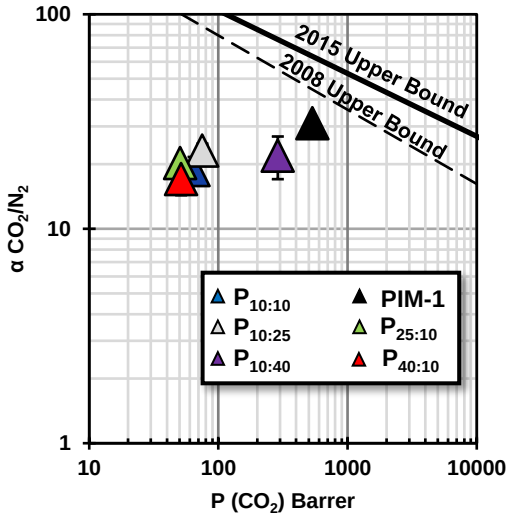

Figure C30. Robeson plot of polymers tested in this study Error bars are included for each data point, but in some cases, the error bars are smaller than the data marker.

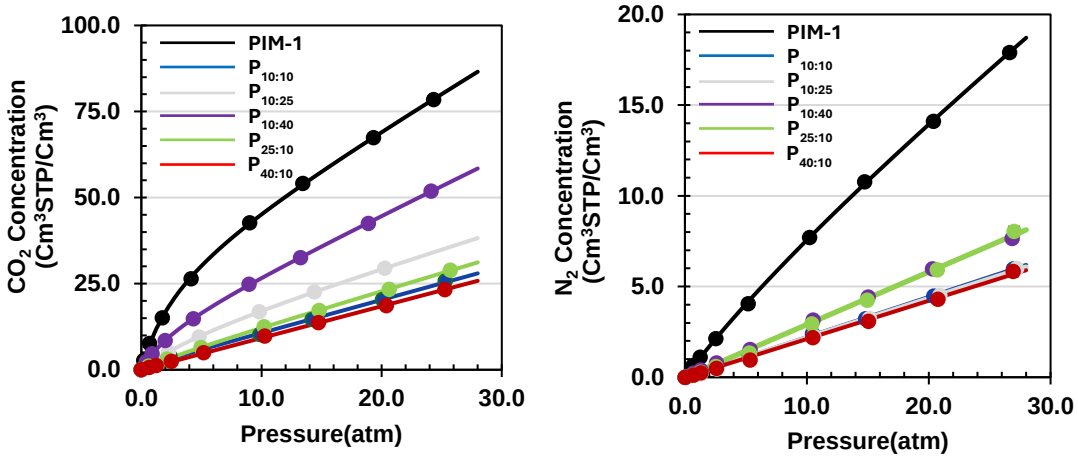

Figure C31. N_2 sorption isotherms (left) and CO_2 sorption isotherms (right) for all polymers.

Table C1. Diffusion and Solubility Coefficients of Copolymer Series, as well as Individual Henry's Law and Langmuir Sorption Parameters.

	D[a] ((cm2·s-1)·10-6)			S[b] (cm3[STP]·/cm3·atm1)			CO_2		N_2	
Polymer	CO_2	N_2	$DCO_2/DN2$	CO_2	N_2	S_{CO2}/S_{N2}	kd	C'_Hb	k_d	C'_Hb
$P^{10:10}$	0.16	0.13	1.24	3.13	0.22	14.13	0.96	2.17	0.22	—c
$P^{10:25}$	0.21	0.11	1.84	2.73	0.22	12.58	1.06	1.67	0.22	—c
$P^{10:40}$	0.36	0.36	1.00	6.09	0.29	20.96	1.68	4.41	0.29	—c
$P^{25:10}$	0.24	0.06	3.66	1.61	0.29	5.55	1.03	0.58	0.29	—c
$P^{40:10}$	0.42	0.11	3.83	0.92	0.21	4.38	0.92	—c	0.21	—c
PIM-1	0.41	0.23	1.80	12.49	0.88	14.10	2.06	10.42	0.54	0.35

[a]Diffusion coefficients (D) were determined algebraically using the D=P/S. [b]Solubility coefficients (S) were measured using the dual-volume pressure decay method and reported as pressure approaches 0. [C]Not applicable as these isotherms were fit linearly.

C.5 Mechanical Analysis

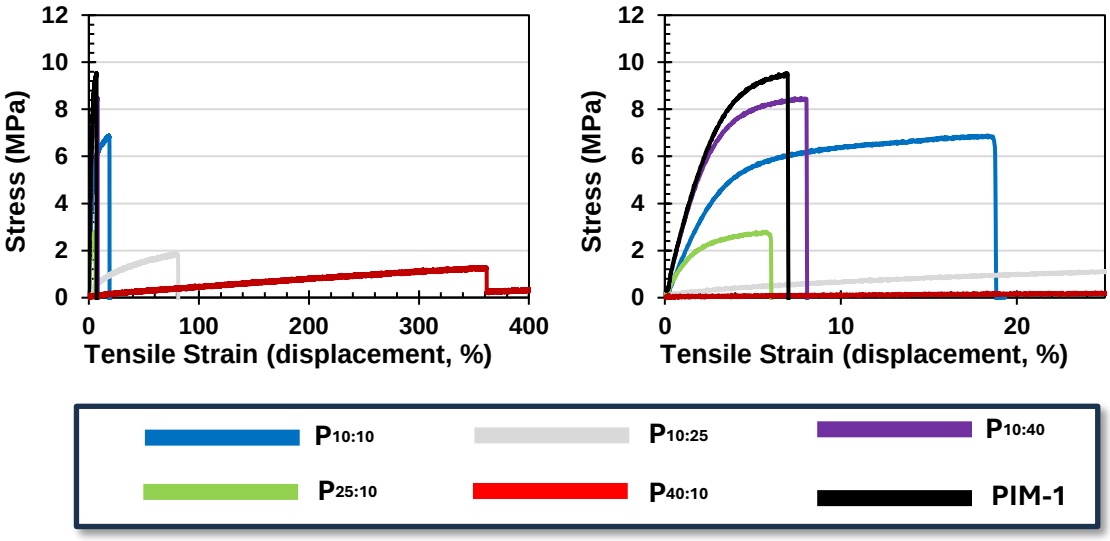

Figure C32. Stress-strain curves of all segmented block copolymers tested in full view (left) and zoomed in (right).

VITA

Elizabeth Margaret Powell (Maggie) was born in Colorado Springs, to Victoria and Russell Powell. She was raised in Mobile, AL where she attended Faith Academy for high school. She then started college at the University of Alabama-Birmingham in 2018 where she received a B.S. in chemistry with a minor in French. Maggie started graduate school at the University of Tennessee-Knoxville in 2020 to pursue a PhD in polymer chemistry. Under the mentorship of Professor Brian Long, Maggie published several peer-reviewed articles and mentored an undergraduate student. Additionally, Maggie served as research open house representative and president of the Association of Chemistry Graduate Students. During these terms, she represented and advocated graduate students within the chemistry department. In her free time, Maggie enjoys reading, cross-stitching, and walking.